ROLE OF PHOSPHORUS DOPING IN

ENHANCING THE ELECTRONIC CONDUCTIVITY OF

BISMUTH VANADATE PHOTOANODES:

A FIRST-PRINCIPLES STUDY

Apinya Ngoipala

A Thesis Submitted in Partial Fulfillment of the Requirements for the

Degree of Master of Science in Physics

Suranaree University of Technology

Academic Year 2019

การศึกษาบทบาทของการเจือฟอสฟอรัสต่อการเพิ่มการนำไฟฟ้า
ในขั้วไฟฟ้าแอโนดบิสมัทวาเนเดตโดยวิธีเฟิร์สทพรินซิเพิล

นางสาวอภิญญา งอยผาลา

วิทยานิพนธ์นี้เป็นส่วนหนึ่งของการศึกษาตามหลักสูตรปริญญาวิทยาศาสตรมหาบัณฑิต
สาขาวิชาฟิสิกส์
มหาวิทยาลัยเทคโนโลยีสุรนารี
ปีการศึกษา 2562

ROLE OF PHOSPHORUS DOPING IN ENHANCING THE ELECTRONIC CONDUCTIVITY OF BISMUTH VANADATE PHOTOANODES: A FIRST-PRINCIPLES STUDY

Suranaree University of Technology has approved this thesis submitted in partial fulfillment of the requirements for a Master's Degree.

Thesis Examining Committee

_____

(Asst. Prof. Dr. Theeranun Siritanon)

Chairperson

_____

(Asst. Prof. Dr. Suwit Suthirakun)

Member (Thesis Advisor)

_____

(Assoc. Prof. Dr. Sirichok Jungthawan)

Member (Thesis Co-Advisor)

_____

(Dr. Ittipon Fongkaew)

Member

_____
(Assoc. Prof. Flt. Lt. Dr. Kontorn Chamniprasart)

Vice Rector for Academic Affairs

and Internationalization

_____
(Assoc. Prof. Dr. Worawat Meevasana)

Dean of Institute of Science

อภิญญา งอยผาลา : การศึกษาบทบาทของการเจือฟอสฟอรัสต่อการเพิ่มการนำไฟฟ้าใน
ขั้วไฟฟ้าแอโนดบิสมัทวาเนเดตโดยวิธีเฟิร์สทพรินซิเพิล (ROLE OF PHOSPHORUS
DOPING IN ENHANCING THE ELECTRONIC CONDUCTIVITY OF BISMUTH
VANADATE PHOTOANODES: A FIRST-PRINCIPLES STUDY) อาจารย์ที่ปรึกษา :
ผู้ช่วยศาสตราจารย์ ดร.สุวิทย์ สุธีรากุล, 143 หน้า.

วิทยานิพนธ์ฉบับนี้ได้ใช้วิธี DFT + U ในการศึกษาบทบาทของการเจือฟอสฟอรัสต่อการ
เปลี่ยนแปลงสมบัติทางโครงสร้างและอิเล็กทรอนิกส์ ความเสถียรของการเกิดช่องว่างของ
ออกซิเจน และการขนส่งประจุในขั้วไฟฟ้าแอโนดบิสมัทวาเนเดต ผลการคำนวณแสดงให้เห็นว่า
การเจือฟอสฟอรัสไม่ส่งผลอย่างมีนัยสำคัญต่อสมบัติทางโครงสร้างและอิเล็กทรอนิกส์ของบิสมัท
วาเนเดต ในทางตรงกันข้าม การเจือฟอสฟอรัสทำให้บิสมัทวาเนเดตถูกรีดิวซ์ได้ดีขึ้นดังสะท้อน
จากการลดลงของพลังงานของการเกิดช่องว่างของออกซิเจน การมีหนึ่งช่องว่างของออกซิเจนจะทำ
ให้เกิดอิเล็กตรอนโพลารอนสองตัวที่ตำแหน่งของวาเนเดียมสองอะตอมที่อยู่ใกล้กัน ซึ่งโพลารอน
หนึ่งตัวจะติดอยู่ที่บริเวณจุดบกพร่อง ในขณะที่โพลารอนอีกหนึ่งตัวจะเคลื่อนที่ได้ ผลของค่า
พลังงานสำหรับการเคลื่อนที่ของโพลารอนจากที่หนึ่งไปยังที่หนึ่งและสภาพคล่องตัวของประจุที่
ได้จากการจำลองแบบไคเนติกมอนติคาร์โลแสดงให้เห็นว่า การเจือฟอสฟอรัสไม่ได้เปลี่ยนแปลง
การขนส่งโพลารอนอย่างมีนัยสำคัญ ดังนั้นจึงสรุปได้ว่า การเจือฟอสฟอรัสทำให้บิสมัทวาเนเดตถูก
รีดิวซ์ได้ดีขึ้น ซึ่งส่งผลให้เกิดการเพิ่มประจุพาหะในบิสมัทวา-เนเดต การเพิ่มขึ้นของความเข้มข้น
พาหะจากการเกิดช่องว่างของออกซิเจนดังที่กล่าวมาข้างต้นจึงส่งผลทำให้เกิดการเพิ่มการนำไฟฟ้า
ในขั้วไฟฟ้าแอโนดบิสมัทวาเนเดต

สาขาวิชาฟิสิกส์   ลายมือชื่อนักศึกษา _อภิญญา   งอยผาลา_
ปีการศึกษา 2562   ลายมือชื่ออาจารย์ที่ปรึกษา_____
                                                 ลายมือชื่ออาจารย์ที่ปรึกษาร่วม_____

APINYA NGOIPALA : ROLE OF PHOSPHORUS DOPING IN
ENHANCING THE ELECTRONIC CONDUCTIVITY OF BISMUTH
VANADATE PHOTOANODES: A FIRST-PRINCIPLES STUDY.
THESIS ADVISOR : ASST. PROF. SUWIT SUTHIRAKUN, Ph.D. 143 PP.

PHOTOANODES/DOPING/OXYGEN VACANCY/CHARGE CARRIERS

In this thesis, DFT+U method was used to study the role of P doping on the change of the geometrical and electronic structures, the stabilities of oxygen vacancies and charge transport properties of $BiVO_4$ photoanodes. Our computations reveal that P impurities does not significantly affect the geometrical and electronic structure of $BiVO_4$. On the other hand, P doping improves the reducibility of $BiVO_4$ as reflect through the lower energies of oxygen vacancy formation. The generated oxygen vacancy yields two electron polarons localized at the two nearest V centers, where one polaron is always trapped at the defect site, while the other polaron is relatively mobile. The calculated polaron hopping barriers and their mobilities obtained from kinetic Monte Carlo simulations indicate that P impurity by itself does not significantly alter the behavior of polaron transport. To conclude, P doping improves reducibility of $BiVO_4$ which in turn increases the number of charge carriers in the material. The increased carrier concentration arising from oxygen vacancy formation could yield the improved electronic conductivity of $BiVO_4$ photoanodes.

School of Physics   Student's Signature _____

Academic Year 2019   Advisor's Signature _____

                                                              Co-Advisor's Signature _____

ACKNOWLEDGEMENTS

CONTENTS

CONTENTS (Continued)

CONTENTS (Continued)

LIST OF TABLES

LIST OF TABLES (Continued)

LIST OF FIGURES

LIST OF FIGURES (Continued)

LIST OF FIGURES (Continued)

LIST OF FIGURES (Continued)

LIST OF FIGURES (Continued)

LIST OF FIGURES (Continued)

LIST OF FIGURES (Continued)

LIST OF ABBREVIATIONS

PEC   = Photoelectrochemical

VBM   = Valence Band Maximum

CBM   = Conduction Band Minimum

TMO   = Transition Metal Oxide

DFT   = Density Functional Theory

GGA   = Generalized Gradient Approximation

FTO   = Fluorine-doped Tin Oxide

PDOS   = Projected Density of States

XPS   = X-ray Photoelectron Spectra

CDD   = Charge Density Difference

LDA   = Local Density Approximation

PAW   = Projector-Augmented Wave

PBE   = Perdew-Burke-Ernzerhof

FLL   = Fully Localized Limit

CI-NEB   = Climbing Image-Nudged Elastic Band

MEP   = Minimum Energy Path

TS   = Transition State

KMC   = Kinetic Monte Carlo

CTL   = Charge Transition Level

CDFT   = Constrained Density Functional Theory

LIST OF ABBREVIATIONS (Continued)

NN   = Nearest Neighbor
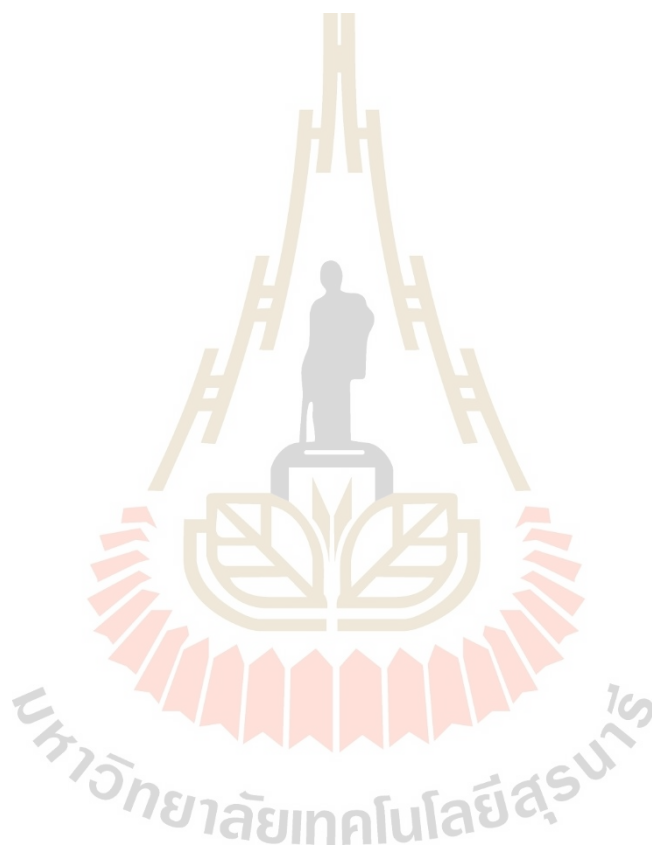
CHAPTER I

INTRODUCTION

1.1   Background and significance

Recently, hydrogen has received great attention as a next-generation energy carrier which is clean, effective, and viable alternative to fossil fuels. Over the past three decades, photocatalytic or photoelectrochemical (PEC) water splitting has received extensive consideration as a potential approach for the clean hydrogen production from a renewable source like solar energy (Tran *et al.*, 2012; Walter *et al.*, 2010). The catalytic splitting of pure water into H_2 and O_2 is a typical uphill reaction with a large positive change in the Gibbs free energy ($\Delta G = 238$ kJ mol^{-1}). Since this reaction is similar to photosynthesis by green plants, it is regarded as a method of artificial photosynthesis. The overall water splitting in an acidic environment can be described as

$$2H_2O \rightarrow 2H_2 + O_2 \qquad E^0_{rxn} = -1.23 \text{ V } vs \text{ NHE} \qquad (1.1)$$

where NHE is abbreviated for normal hydrogen electrode. The half-reactions are described as

$$4H^+ + 4e^- \rightarrow 2H_2 \qquad E^0_{cathode} = 0 \text{ V } vs \text{ NHE} \qquad (1.2)$$

$$2H_2O \rightarrow O_2 + 4H^+ + 4e^- \qquad E^0_{anode} = -1.23 \text{ V } vs \text{ NHE.} \qquad (1.3)$$
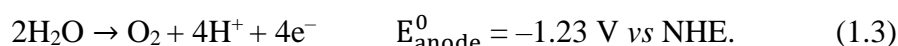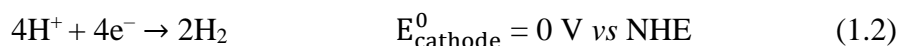
For the overall water splitting on a semiconductor photocatalyst, when the semiconductor absorbs the light with an energy equivalent to or greater than its band

gap, electrons in the valence band (VB) are excited into the conduction band (CB), leaving holes in the VB meanwhile. These photogenerated electron–hole pairs separate and migrate to the surface without recombination. Then, the adsorbed species are reduced and oxidized by the photoexcited electrons and holes to produce H_2 and O_2, respectively. To achieve overall water splitting, the conduction band minimum (CBM) of the material must be more negative than the reduction potential of H^+ to H_2 (0 V *vs* NHE at pH 0), while valence band maximum (VBM) must be more positive than the oxidation potential of H_2O to O_2 (1.23 V *vs* NHE). Thus, the minimum photon energy that thermodynamically required to drive this reaction is 1.23 eV (Maeda, 2011).

Several efforts have been made to research and develop the suitable and efficient semiconductors to use as photocatalysts for water splitting. There are three requirements for efficient photocatalysts including (i) band-edge potentials suitable for overall water splitting (ii) band-gap energy lower than 3 eV to harvest visible light (iii) stability in the photocatalytic reaction (Maeda, 2011). Recently, numerous efforts have been made to design and develop efficient transition metal oxide (TMO) semiconductors as photocatalysts in PEC cells (Jafari *et al.*, 2016; Maeda, 2011). Bismuth vanadate ($BiVO_4$) has been identified as one of the most promising photoanode materials for solar water oxidation to O_2 because it possesses unique physical and electrochemical properties including ability to effectively harvest sunlight at the visible spectrum and high stability under electrochemical conditions (Kudo *et al.*, 1999; Y. Park *et al.*, 2013; Tokunaga *et al.*, 2001; Xi and Ye, 2010; Zhao *et al.*, 2011). In particular, among various crystalline phases of $BiVO_4$, monoclinic scheelite (*ms*-) $BiVO_4$ exhibits the highest photocatalytic activity as the

distortion of VO$_4$ tetrahedra creates local polarization (Tokunaga *et al.*, 2001), which could facilitate the separation of photogenerated electron–hole pairs.

Despite the mentioned advantages, BiVO$_4$ still suffers from major limitations such as extreme recombination of photogenerated electron–hole pairs (Abdi and van de Krol, 2012; Zhong *et al.*, 2011), low electrical conductivity (Abdi *et al.*, 2013; Ziwritsch *et al.*, 2016), and poor water oxidation kinetics (Berglund *et al.*, 2012), resulting in a main bottleneck for practical PEC performance. Such a low intrinsic conductivity and mobility is typically encountered in various TMOs due to the slow thermally activated hopping conduction instead of fast band conduction in Group A semiconductors (Bosman and van Daal, 1970; Lany, 2015). In TMOs such as BiVO$_4$, an extra electron prefers to localize at one transition metal (TM) center due to strong electron–electron repulsion in contracted *d* orbitals and thereby reduce TM^{n+} to TM$^{(n-1)+}$. The trapped electrons are accompanied by local lattice distortion of the surrounding lattice leading to a formation of small polarons. The small polarons can undergo thermally activated hopping from one TM site to the nearby site which is much slower than that of the band conduction (on the order of 0.1 cm^2 V^{-1} s^{-1} electron mobility for BiVO$_4$ compared to 1450 cm^2 V^{-1} s^{-1} for Si) (Canali *et al.*, 1975).

To improve the charge transport kinetics of BiVO$_4$, researchers have focused on developing strategies to overcome these drawbacks, including morphology control (Luo *et al.*, 2010; Pilli *et al.*, 2011), composite structure (heterojunction formation) (Pilli *et al.*, 2013; Selim *et al.*, 2019), oxygen evolution catalyst loading (Berglund *et al.*, 2012; Jeon *et al.*, 2011), defect formation (oxygen vacancy creation) (Kim *et al.*, 2015; Seo *et al.*, 2018; Ullah *et al.*, 2018), and doping. Both experimental and theoretical studies have reported that the substitutional doping at V site with W (H. S.

Park *et al.*, 2011; Yin *et al.*, 2011; Zhang *et al.*, 2016), Mo (B. Liu *et al.*, 2017; H. S. Park *et al.*, 2011; Yin *et al.*, 2011; Zhang *et al.*, 2016), and P (Jo *et al.*, 2012; G. Liu *et al.*, 2014; Regmi *et al.*, 2019; Xia *et al.*, 2018), or at Bi site with Sm (Govindaraju *et al.*, 2018), Yb (Govindaraju *et al.*, 2018), and Ce (Jiang *et al.*, 2016), or at O site with Se (Ullah *et al.*, 2018), and N (Kim *et al.*, 2015; Seo *et al.*, 2018) could enhance electron–hole separation, carrier mobilities, and conductivities of the $BiVO_4$ photoanode. In particular, it has been shown by several studies that addition of small amount of P impurities significantly improves photocurrent density, photocatalytic O_2 evolution rate, carrier concentrations and mobility (Jo *et al.*, 2012; G. Liu *et al.*, 2014; Regmi *et al.*, 2019; Xia *et al.*, 2018). Computations based on density functional theory (DFT) reveal that substitution of P at the V site increases electron density at the surrounding O atoms leading to polarization of P–O bonds which could facilitate charge separation and improve photocatalytic activity (Regmi *et al.*, 2019). Furthermore, the electron density at the top of the VB could increase carrier concentration in the material (Jo *et al.*, 2012; Regmi *et al.*, 2019). Nevertheless, one experimental study based on X-ray photoelectron spectroscopy suggests that P-doped samples contain noticeable amount of oxygen vacancies which could enhance charge transport properties (Xia *et al.*, 2018).

Such ambiguous explanations on the origin of superior electrochemical performance of P-doped $BiVO_4$ have motivated us to further explore the fundamental role of P doping on the formation of oxygen vacancies and corresponding charge transport properties. Note that, the microscopic description of localized charge states depends strongly on the method employed. The conventional DFT with the generalized gradient approximation (GGA) is an unsuccessful approach to predict

charge localization (affect delocalization of charge carriers) due to the self-interaction error inherent in current exchange-correlation functional (Cohen *et al.*, 2008; Mori-Sánchez *et al.*, 2008). To correct the self-interaction error, DFT energy functional including Hubbard-U term have been performed to take into account of strong on-site *d* electron interactions (H. S. Park *et al.*, 2011). Park *et al.* have investigated that the localized charge carriers in bulk $BiVO_4$ can appropriately be described when applying the DFT+U approach with the U value of 2.7 eV for the V $3d$ states. The band gap of $BiVO_4$ is consistent with the obtained value from experiments. The DFT+U calculation has been shown to be a successful method for describing the charge localization and their transport kinetics in $BiVO_4$-based photoanodes (T. Liu *et al.*, 2015; Pasumarthi *et al.*, 2019; Regmi *et al.*, 2019; Seo *et al.*, 2018; Wu and Ping, 2018; Zhang *et al.*, 2016). Therefore, it is the objective of this work to utilize computational tools based on the DFT+U method to study the effect of P substitution on (i) the change of the geometrical and electronic structures (ii) the interplay between formation of oxygen vacancies and charge transport properties of $BiVO_4$-based photoanodes. The obtained fundamental understanding could be used to rationally design doping strategies to obtain high performance photocatalysts. In addition, we briefly review the experimental and theoretical studies of the introduction of P in $BiVO_4$ for the enhanced photocatalytic performance in the following section.

The rest of this thesis is arranged as follows. In Chapter II, we give a brief description of the theoretical and computational approaches employed. In Chapter III, we present geometrical and electronic structures of the doped system and compare them with those of the pristine $BiVO_4$. In Chapter IV, we discuss the role of P doping

on the reducibility of $BiVO_4$, involving the formation of oxygen vacancy and its stability. In Chapter V, we discuss the migration barriers of electrons originated from the formation of oxygen vacancy as well as their mobilities to understand the interaction between the polarons and the defect site. Finally, we summarize the main implications of our results, with a focus on the role of the P substitution in enhancing the electronic conductivity of $BiVO_4$-based photoanodes in Chapter VI.

1.2   Literature review

In recent years, several attempts have been made to develop the effective strategies to improve the photocatalytic activity of $BiVO_4$. Both experimental and theoretical studies have reported that the substitutional doping in $BiVO_4$ with P could enhance photocurrent density, photocatalytic O_2 evolution rate, electron–hole separation, carrier concentrations and mobility, which are responsible for high photocatalytic activities (Jo *et al.*, 2012; G. Liu *et al.*, 2014; Regmi *et al.*, 2019; Xia *et al.*, 2018).

Jo *et al.* studied the enhanced photoelectrochemical properties of P-doped $BiVO_4$. Phosphorus atoms were introduced into the vanadium sites in the host lattice of monoclinic clinobisvanite $BiVO_4$ with different target atom ratios (0.5%, 1%, and 5%). All P-doped $BiVO_4$ samples were synthesized in a powder form by urea-precipitation method and they were loaded onto the fluorine-doped tin oxide (FTO) glass by using electrophoretic deposition technique. The experimental study revealed that $BiVO_4$ doped with 0.5% of P exhibits the best photocurrent density (0.548 $mAcm^{-2}$ at 0.7 V), which is about 30 times higher than of pristine $BiVO_4$ (0.019 $mAcm^{-2}$ at 0.7 V) and it also improves photocatalytic O_2 evolution rates as shown in

Figure 1.1. Moreover, the electrochemical impedance spectroscopy measurements show that P doping remarkably lowers the charge transfer resistance of $BiVO_4$.
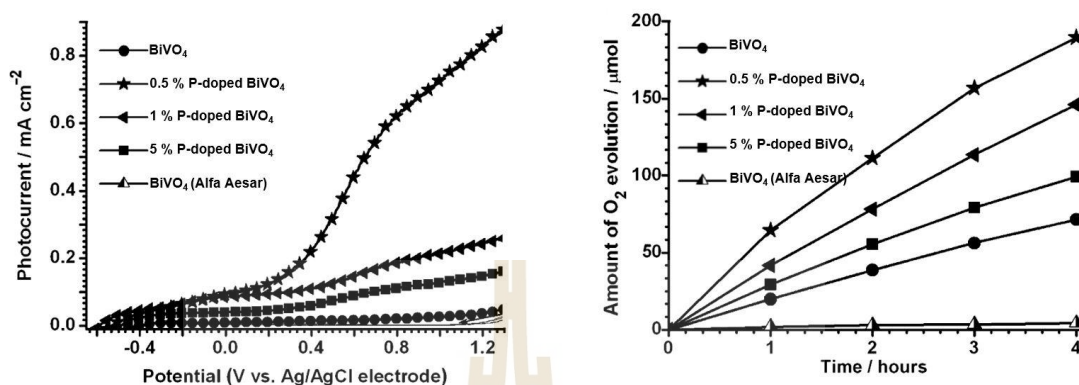
Figure 1.1 Photocurrent-potential curves of pristine $BiVO_4$, and 0.5%, 1%, and 5% PO_4-doped $BiVO_4$ (left). The back side of photo-anodes was illuminated with a xenon arc lamp (300 W) fitted with a UV cut-off filter ($\lambda \geq 420$ nm). Photocatalytic water oxidation with bare and PO_4-doped $BiVO_4$ under the visible light ($\lambda \geq 420$ nm) irradiation (right). The photocatalyst powders (0.1 g) were dispersed in aqueous $AgNO_3$ solution as an electron scavenger (Jo *et al.*, 2012).

To clarify the effect of P doping in $BiVO_4$, they carried out theoretical approach based on DFT calculations to study the electronic properties of P-doped $BiVO_4$. A supercell of $1\times2\times1$ monoclinic clinobisvanite $BiVO_4$ was constructed to be the calculated model. For P-doped $BiVO_4$ system, one of sixteen V atoms is substituted by a P atom (6.25% doping concentration). The findings revealed that the obtained band gap of pristine $BiVO_4$ is 1.94 eV, whereas the slightly larger band gap of 1.95 eV was observed in P-doped system. Upon P doping, the length of P–O bond is 1.563 Å, which is slightly smaller than the V–O bond (1.737 Å). The O $2p$ peak increases at –0.7 eV as evident by projected density of states (PDOS) plots as illustrated in Figure 1.2(a). The ratio of integrated DOS in the energy window of –0.7

eV from VBM to total electrons are 4.0% and 5.9% for pristine and P-doped BiVO₄, respectively, which indicate that the substitution of P could increase charge carriers in BiVO₄, leading to the higher photocatalytic performance. Form Bader charge analysis of P-doped BiVO₄ system, the charge is transferred from P atom to O atoms due to a lower electronegativity of P atom. Therefore, P atom has a much smaller charge (1.357 electrons) than V atom (3.102 electrons) in pristine system. Also, O atoms in PO₄ tetrahedron have a large charge (fluctuate between 7.406 and 7.453 electrons) than O atoms (6.966 electrons) in the pristine BiVO₄. They concluded that the charge redistribution around the dopant may cause the separation of electron–hole pairs as demonstrated in Figure 1.2(b), which could improve the photocatalytic property.
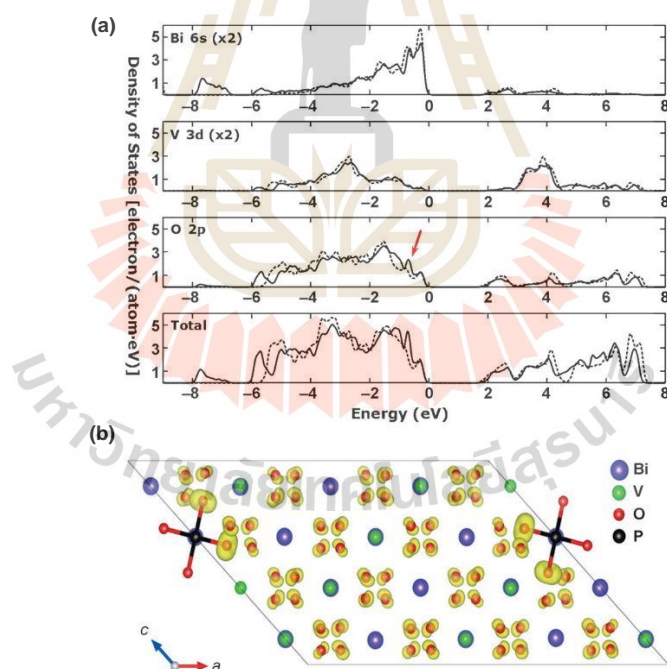
Figure 1.2 (a) Total and projected DOS of monoclinic clinobisvanite BiVO₄ (dotted line) and P-doped BiVO₄ (solid line). (b) Calculated isosurface of integrated charge density in the range from –0.7 eV (red arrow) to Fermi energy for P-doped BiVO₄. Only P–O bonds are shown for clarity (Jo *et al.*, 2012).

The monoclinic $BiVO_4$ doped with different amounts of phosphorus (0.5%, 1%, and 5%) have also been studied by Liu *et al.* They were prepared by an electrospinning method combined with calcination. The experimental results showed that the ultraviolet-visible absorption spectra of the pristine and P-doped $BiVO_4$ are almost the same. $BiVO_4$ is a direct band gap semiconductor with the band gap energy of 2.36 eV whereas the band gap energies of P-doped $BiVO_4$ samples are estimated to be 2.37, 2.49 and 2.50 eV for the doping concentration of 0.5%, 1% and 5%, respectively. Therefore, the band gap increases upon P doping. The 0.5% P-doped $BiVO_4$ exhibits the better photocatalytic activity compared to pristine $BiVO_4$. It is known that the recombination of electron–hole pairs can release energy in the form of fluorescence emission. Thus, a low fluorescence emission intensity implies a lower electron–hole recombination rate. The photoluminescence emission spectra revealed that the emission intensity of pristine $BiVO_4$ is higher than those of the 5%, 1%, 0.5% P-doped samples, and the order is pristine $BiVO_4 > 5\% > 1\% > 0.5\%$ P-doped $BiVO_4$, which suggests that the doped phosphorus reduces the electron–hole pairs recombination rate, leading to high charge density which corresponds to higher photocatalytic activity.

Recently, the 0.6%, 2%, and 4% P-doped $BiVO_4$ have been investigated by Xia *et al.* The P-doped $BiVO_4$ samples were fabricated on FTO substrate by using a simple dip-coating method and subsequent thermal treatment process. Phosphorus element is uniformly dispersed into $BiVO_4$. The X-ray diffraction patterns showed that the increasing amount of P element did not result in any other peaks. This finding can be explained that P doping quantity is too small, resulting that P doping does not change the crystalline structure of $BiVO_4$. However, the incident photon-to-current

efficiency of 2% P-doped $BiVO_4$ is increased to 33%, which is significantly higher than that of pristine $BiVO_4$ as shown in Figure 1.3. Interestingly, the analysis of X-ray photoelectron spectra (XPS) indicates that the 2% P-doped $BiVO_4$ possess more abundant oxygen vacancies (see Figure 1.4). The oxygen vacancy could facilitate the capture of electrons, which is favorable for the separation of electron–hole pairs, accounting for the enhanced photocatalytic performance.
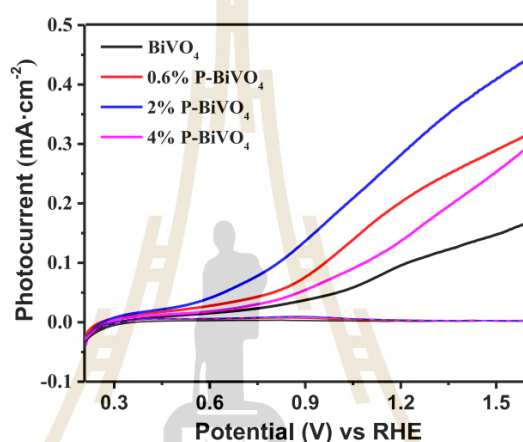
Figure 1.3 Photocurrent-potential curves of pristine $BiVO_4$, 0.6%, 2%, and 4% P-$BiVO_4$ in 0.5 M Na_2SO_4 electrolyte with the AM 1.5 G simulated solar light at 100 mW cm^{-2} (dashed lines represent dark currents) (Xia *et al.*, 2018).
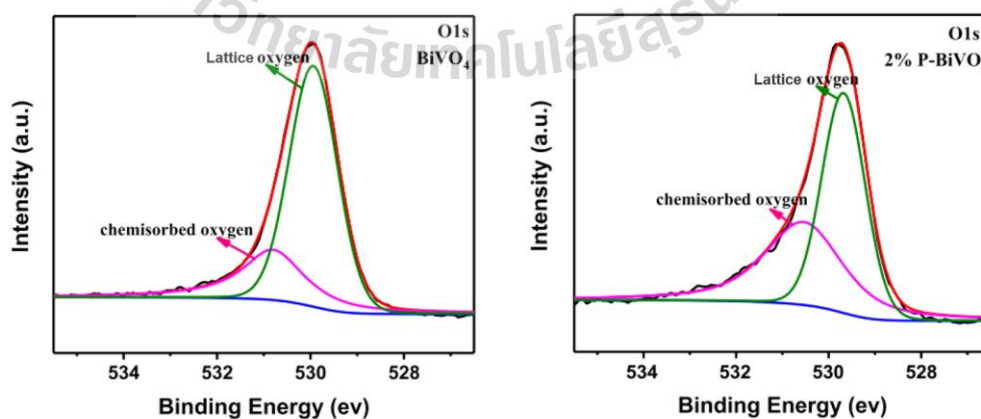
Figure 1.4 XPS spectra of O 1s of $BiVO_4$ (left) and 2% P-doped $BiVO_4$ (right) (Xia *et al.*, 2018).

In addition, Regmi *et al.* reported the synthesis of P-doped BiVO$_4$ with different concentration using a microwave hydrothermal method and investigated its photocatalytic activity. The experimental results showed that the doped samples exhibit higher photocatalytic activity than that of pristine BiVO$_4$, which is consistent with the previous studies (Jo *et al.*, 2012; G. Liu *et al.*, 2014; Xia *et al.*, 2018). Furthermore, they studied the electronic properties of BiVO$_4$ upon P doping in the similar way as a previous study (Jo *et al.*, 2012) by means of DFT+U calculations to understand the improved photocatalytic performance. They applied U of 2.7 eV to account of the strongly localized nature of 3d orbitals in V atom. A 1×2×1 monoclinic BiVO$_4$ was used for calculation. The P-doped BiVO$_4$ was formed by replacing a V atom with a P atom (6.25% doping concentration) as illustrated in Figure 1.5.
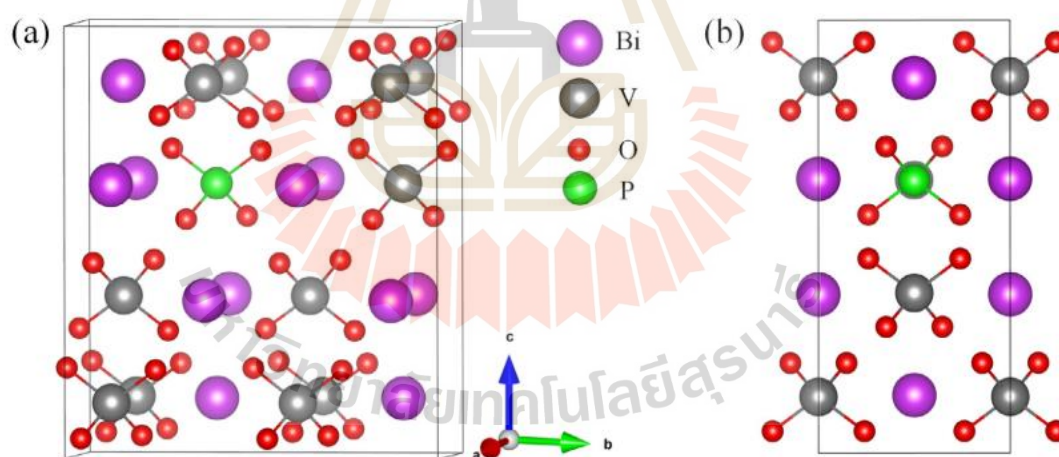
Figure 1.5 (a) Supercell model structure of phosphate doped BiVO$_4$ considered in the calculation (b) Side view of the supercell in (a) (Regmi *et al.*, 2019).

They found that the calculated band gap is 2.11 and 2.13 eV for pristine and P-doped systems, respectively. The larger DOS in the energy range from –0.8 eV to VBM was observed upon P doping (see Figure 1.6), implies an increase of charge

carriers in the material. These results are consistent with a previous study (Jo *et al.*, 2012).
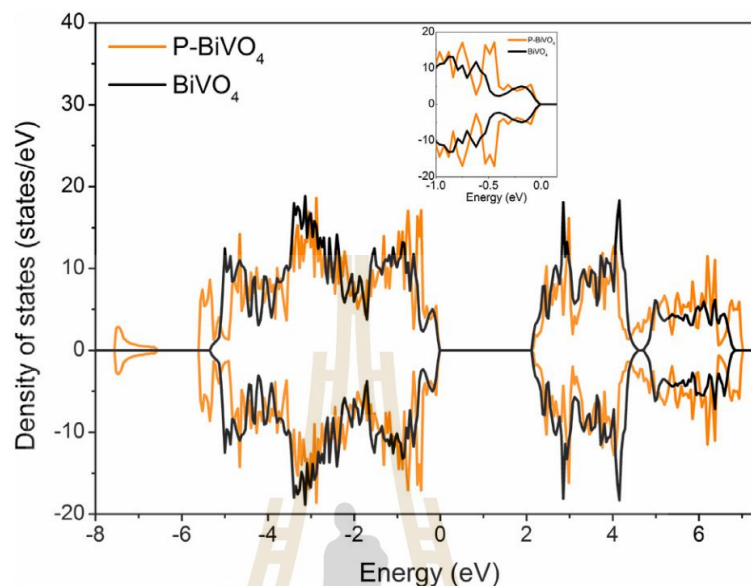
Figure 1.6 Total DOS of pure BiVO$_4$ and phosphate doped BiVO4. The inset shows the magnified view of the DOS in the energy range from −1.0 eV to the top of the VB (Regmi *et al.*, 2019).

In P-doped system, there are two different P–O bond lengths in PO$_4$ unit where the P–O bond length of the upper pair of atoms is slightly longer (1.570 Å) than that of the lower pair (1.566 Å) as shown in Figure 1.7(a). It is indicated that the P–O bond relaxation improves the redox ability and hence the photocatalytic activity. Moreover, they calculated the charge density difference (CDD) of P-doped BiVO$_4$ system as illustrated in Figure 1.7(b) and 1.7(c). The CCD indicated that there is charge accumulation occurring at the vicinity of O atoms in PO$_4$ which verifies the transfer of electrons from P to O atoms. Interestingly, the CDD distributions of the pair of O atoms on the upper and lower half of PO$_4$ are different. More charge is accumulated in the upper pair than that in the lower pair of O atoms, which results in

a dipole moment, thus improving electron–hole separation and benefiting the photocatalytic activity.
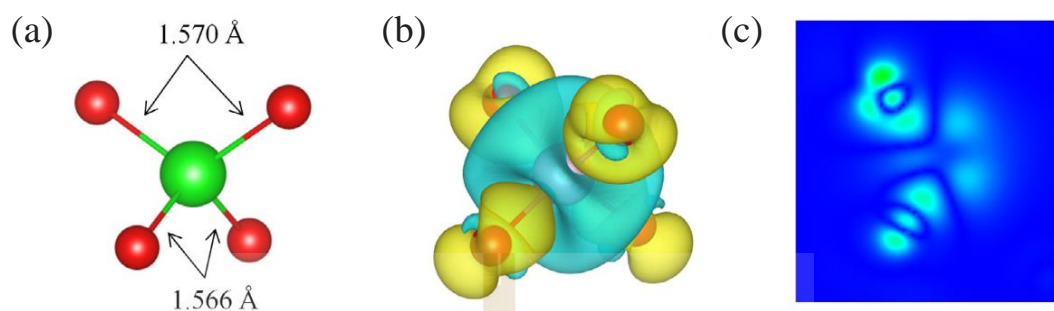
Figure 1.7 (a) PO_4 polyhedron (b) CDD isosurfaces of the PO_4 polyhedron (c) A section of the CDD isosurfaces in (b) showing CDD in the left pair of O atoms in the PO_4 polyhedron (Regmi *et al.*, 2019).

Beside the previous studies mentioned above, other aspects of role of P doping such as charge transport mechanism have not been studied. Additionally, the explanations on the origin of superior photocatalytic performance of P-doped $BiVO_4$ is still unclear. These motivated us to further investigate the role of P doping on the formation of oxygen vacancies and corresponding charge transport properties in $BiVO_4$ photoanodes.

1.3   References

Abdi, F. F., Savenije, T. J., May, M. M., Dam, B. and van de Krol, R. (2013). The Origin of Slow Carrier Transport in $BiVO_4$ Thin Film Photoanodes: A Time-Resolved Microwave Conductivity Study. **J. Phys. Chem. Lett.** 4: 2752.

Abdi, F. F. and van de Krol, R. (2012). Nature and Light Dependence of Bulk Recombination in Co-Pi-Catalyzed BiVO$_4$ Photoanodes. **J. Phys. Chem. C.** 116: 9398.

Berglund, S. P., Rettie, A. J. E., Hoang, S. and Mullins, C. B. (2012). Incorporation of Mo and W into nanostructured BiVO$_4$ films for efficient photoelectrochemical water oxidation. **Phys. Chem. Chem. Phys.** 14: 7065.

Bosman, A. J. and van Daal, H. J. (1970). Small-Polaron versus Band Conduction in Some Transition-Metal Oxides. **Adv. Phys.** 19: 1.

Canali, C., Majni, G., Minder, R. and Ottaviani, G. (1975). Electron and Hole Drift Velocity Measurements in Silicon and Their Empirical Relation to Electric Field and Temperature. **IEEE Trans. Electron Devices.** 22: 1045.

Cohen, A. J., Mori-Sánchez, P. and Yang, W. (2008). Insights into Current Limitations of Density Functional Theory. **Science.** 321: 792.

Govindaraju, G. V., Morbec, J. M., Galli, G. A. and Choi, K.-S. (2018). Experimental and Computational Investigation of Lanthanide Ion Doping on BiVO$_4$ Photoanodes for Solar Water Splitting. **J. Phys. Chem. C.** 122: 19416.

Jafari, T., Moharreri, E., Amin, S. A., Miao, R., Song, W. and Suib, L. S. (2016). Photocatalytic Water Splitting-The Untamed Dream: A Review of Recent Advances. **Molecules.** 21: 900.

Jeon, T. H., Choi, W. and Park, H. (2011). Cobalt–Phosphate Complexes Catalyze the Photoelectrochemical Water Oxidation of BiVO$_4$ Electrodes. **Phys. Chem. Chem. Phys.** 13: 21392.

Jiang, Z., Liu, Y., Jing, T., Huang, B., Zhang, X., Qin, X., Dai, Y. and Whangbo, M.-H. (2016). Enhancing the Photocatalytic Activity of $BiVO_4$ for Oxygen Evolution by Ce Doping: Ce^{3+} Ions as Hole Traps. **J. Phys. Chem. C.** 120: 2058.

Jo, W. J., Jang, J.-W., Kong, K.-j., Kang, H. J., Kim, J. Y., Jun, H., Parmar, K. P. S. and Lee, J. S. (2012). Phosphate Doping into Monoclinic $BiVO_4$ for Enhanced Photoelectrochemical Water Oxidation Activity. **Angew Chem. Int. Ed.** 51: 3147.

Kim, T. W., Ping, Y., Galli, G. A. and Choi, K.-S. (2015). Simultaneous Enhancements in Photon Absorption and Charge Transport of Bismuth Vanadate Photoanodes for Solar Water Splitting. **Nat. Commun.** 6: 8769.

Kudo, A., Omori, K. and Kato, H. (1999). A Novel Aqueous Process for Preparation of Crystal Form-Controlled and Highly Crystalline $BiVO_4$ Powder from Layered Vanadates at Room Temperature and Its Photocatalytic and Photophysical Properties. **J. Am. Chem. Soc.** 121: 11459.

Lany, S. (2015). Semiconducting Transition Metal Oxides. **J. Phys.: Condens. Matter.** 27: 283203.

Liu, B., Yan, X., Yan, H., Yao, Y., Cai, Y., Wei, J., Chen, S., Xu, X. and Li, L. (2017). Preparation and Characterization of Mo Doped in $BiVO_4$ with Enhanced Photocatalytic Properties. **Materials.** 10: 976.

Liu, G., Liu, S., Lu, Q., Sun, H. and Xiu, Z. (2014). Synthesis and characterization of $Bi(VO_4)1-m(PO_4)m$ nanofibers by electrospinning process with enhanced photocatalytic activity under visible light. **RSC Adv.** 4: 33695.

Liu, T., Zhou, X., Dupuis, M. and Li, C. (2015). The nature of photogenerated charge separation among different crystal facets of BiVO4 studied by density functional theory. **Phys. Chem. Chem**. **Phys.** 17: 23503.

Luo, W., Wang, Z., Wan, L., Li, Z., Yu, T. and Zou, Z. (2010). Synthesis, growth mechanism and photoelectrochemical properties of BiVO4microcrystal electrodes. **J. Phys. D: Appl. Phys.** 43: 405402.

Maeda, K. (2011). Photocatalytic Water Splitting Using Semiconductor Particles: History and Recent Developments. **J. Photochem. Photobiol. C.** 12: 237.

Mori-Sánchez, P., Cohen, A. J. and Yang, W. (2008). Localization and Delocalization Errors in Density Functional Theory and Implications for Band-Gap Prediction. **Phys. Rev. Lett.** 100: 146401.

Park, H. S., Kweon, K. E., Ye, H., Paek, E., Hwang, G. S. and Bard, A. J. (2011). Factors in the Metal Doping of BiVO$_4$ for Improved Photoelectrocatalytic Activity as Studied by Scanning Electrochemical Microscopy and First-Principles Density-Functional Calculation. **J. Phys. Chem. C.** 115: 17870.

Park, Y., McDonald, K. J. and Choi, K.-S. (2013). Progress in Bismuth Vanadate Photoanodes for Use in Solar Water Oxidation. **Chem. Soc. Rev.** 42: 2321.

Pasumarthi, V., Liu, T., Dupuis, M. and Li, C. (2019). Charge carrier transport dynamics in W/Mo-doped BiVO4: first principles-based mesoscale characterization. **J. Mater. Chem. A.** 7: 3054.

Pilli, S. K., Deutsch, T. G., Furtak, T. E., Brown, L. D., Turner, J. A. and Herring, A. M. (2013). BiVO$_4$/CuWO$_4$ Heterojunction Photoanodes for Efficient Solar Driven Water Oxidation. **Phys. Chem. Chem. Phys.** 15: 3273.

Pilli, S. K., Furtak, T. E., Brown, L. D., Deutsch, T. G., Turner, J. A. and Herring, A. M. (2011). Cobalt-phosphate (Co-Pi) catalyst modified Mo-doped $BiVO_4$ photoelectrodes for solar water oxidation. **Energ. Environ. Sci.** 4: 5028.

Regmi, C., Kshetri, Y. K., Dhakal, D., Sohng, J. K., Rosei, F. and Lee, S. W. (2019). Insight into Phosphate Doped $BiVO_4$ Heterostructure for Multifunctional Photocatalytic Performances: A Combined Experimental and DFT Study. **Appl. Surf. Sci.** 466: 787.

Selim, S., Francàs, L., García-Tecedor, M., Corby, S., Blackman, C., Gimenez, S., Durrant, J. R. and Kafizas, A. (2019). WO_3/$BiVO_4$: Impact of Charge Separation at the Timescale of Water Oxidation. **Chem. Sci.** 10: 2643.

Seo, H., Ping, Y. and Galli, G. (2018). Role of Point Defects in Enhancing the Conductivity of $BiVO_4$. **Chem. Mater.** 30: 7793.

Tokunaga, S., Kato, H. and Kudo, A. (2001). Selective Preparation of Monoclinic and Tetragonal $BiVO_4$ with Scheelite Structure and Their Photocatalytic Properties. **Chem. Mater.** 13: 4624.

Tran, P. D., Wong, L. H., Barber, J. and Loo, J. S. C. (2012). Recent Advances in Hybrid Photocatalysts for Solar Fuel Production. **Energ. Environ. Sci.** 5: 5902.

Ullah, H., Tahir, A. A. and Mallick, T. K. (2018). Structural and electronic properties of oxygen defective and Se-doped p -type BiVO 4 (001) thin film for the applications of photocatalysis. **Appl. Catal. B Environ.** 224: 895.

Walter, M. G., Warren, E. L., McKone, J. R., Boettcher, S. W., Mi, Q., Santori, E. A. and Lewis, N. S. (2010). Solar Water Splitting Cells. **Chem. Rev.** 110: 6446.

Wu, F. and Ping, Y. (2018). Combining Landau–Zener Theory and Kinetic Monte Carlo Sampling for Small Polaron Mobility of Doped $BiVO_4$ from First-Principles. **J. Mater. Chem. A.** 6: 20025.

Xi, G. and Ye, J. (2010). Synthesis of Bismuth Vanadate Nanoplates with Exposed (001) Facets and Enhanced Visible-Light Photocatalytic Properties. **Chem. Commun.** 46: 1893.

Xia, T., Chen, M., Xiao, L., Fan, W., Mao, B., Xu, D., Guan, P., Zhu, J. and Shi, W. (2018). Dip-Coating Synthesis of P-doped $BiVO_4$ Photoanodes with Enhanced Photoelectrochemical Performance. **J. Taiwan Inst. Chem. E.** 93: 582.

Yin, W.-J., Wei, S.-H., Al-Jassim, M. M., Turner, J. and Yan, Y. (2011). Doping Properties of Monoclinic $BiVO_4$ Studied by First-Principles Density-Functional Theory. **Phys. Rev. B.** 83: 155102.

Zhang, J., Deng, M., Ren, F., Wu, Y. and Wang, Y. (2016). Effects of Mo/W Codoping on the Visible-Light Photocatalytic Activity of Monoclinic $BiVO_4$ within the GGA + U Framework. **RSC Adv.** 6: 12290.

Zhao, Z., Li, Z. and Zou, Z. (2011). Electronic Structure and Optical Properties of Monoclinic Clinobisvanite $BiVO_4$. **Phys. Chem. Chem. Phys.** 13: 4746.

Zhong, D. K., Choi, S. and Gamelin, D. R. (2011). Near-Complete Suppression of Surface Recombination in Solar Photoelectrolysis by "Co-Pi" Catalyst-Modified W:$BiVO_4$. **J. Am. Chem. Soc.** 133: 18370.

Ziwritsch, M., Müller, S., Hempel, H., Unold, T., Abdi, F. F., van de Krol, R.,
Friedrich, D. and Eichberger, R. (2016). Direct Time-Resolved Observation of
Carrier Trapping and Polaron Conductivity in $BiVO_4$. **ACS Energy Lett.** 1:
888.
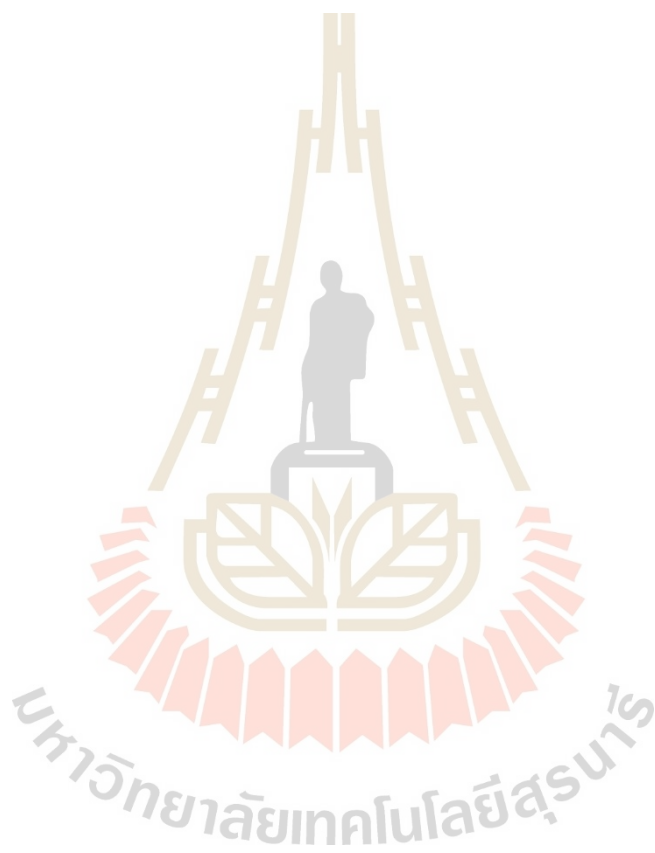
CHAPTER II

THEORETICAL AND COMPUTATIONAL

APPROACHES

2.1 Density functional theory (DFT)

In condensed-matter physics and quantum chemistry, the characteristics of materials such as electronic, optical, and magnetic properties arise from the behavior of atoms and their crystal structures. Since the electrons are dominated by the laws of quantum mechanics, the Schrödinger equation are employed to describe all systems ranging from atoms and molecules to complex materials. The Schrödinger equation are attainable for only very simple systems, but for systems with large number of atoms, the electrostatic repulsion between the electrons makes the problems very difficult to solve. Therefore, the quantum mechanics with the appropriate approximations are used to solve the problems by reducing complexity of the systems while providing the accurate solutions.

The earliest and extensively used approximation was that of Hartree theory (Hartree, 1928). This theory is expressed the wave function of system as a product of one-electron wave functions, so that the problem reduces to a one-electron Schrodinger equation. However, such functions do not possess antisymmetric property which are not correct for many-body systems. To this end, the so-called Hartree-Fock theory (Fock, 1930) was proposed which compose wave function of system in the form of

slater determinant. As a result of replacing the product of one-electron wave functions by a linear combination of orbitals (Slater, 1930), the total energy of system incorporates the exchange effects. However, this theory neglects the correlation effect which makes the obtained solution inaccurate. Also, this theory is not suitable for practical use because it requires high computational resources for systems with large number of electrons. To overcome these drawbacks, DFT, one of the most widely used methods for ab initio calculations of the structure of materials, is applied, where crucial developments in exchange-correlation energy has been taken into account. This approach is expressed in terms of the electron density in the Hohenberg-Kohn theorems (Hohenberg and Kohn, 1964) and in terms of electron density and the single-particle wave functions in the Kohn-Sham equation (Kohn and Sham, 1965). The description in detail of DFT are described in the following sections.

2.1.1 The Hohenberg-Kohn theorems

The Hohenberg-Kohn Theorems are the fundamental theorems for DFT. This theorem was proposed in 1964 by P. Hohenberg and W. Kohn (Hohenberg and Kohn, 1964). Instead of calculating all electrons interacting with each other, they proposed the two concepts of electron density within the framework of DFT which are as follows:

1. The ground-state energy and all behaviors of electron wavefunction in the external potential can be determined from the electron density.

2. For every external potential, there exists a universal energy functional. Its global minimum corresponds to the ground state of the system and the ground-state electron density.

2.1.2 The Kohn-Sham equation

In 1965, Kohn and Sham (Kohn and Sham, 1965) proposed the method to solve the Schrödinger equation for many-body systems based on the Hohenberg-Kohn theorems and Born-Oppenheimer approximation. They divided the term of total energy into two parts including the known and unknown energy functionals, where considering the energy that corresponds to electrons only. The kinetic energy of electrons in many-body systems can be separated into two terms, namely the known kinetic energy which is the kinetic energy of non-interacting electrons, $T_{\text{non}}[n(r)]$ and the unknown term which is the kinetic energy of electron-electron correlation, $T_{\text{corr}}[n(r)]$. For the potential energy of electrons in many-body systems, it consists of two parts which are the potential energy of interaction between electron and electron, E_{ee} and the potential energy of interaction between nucleus and electron, E_{Ne}.

Based on the Hartree-Fock theory, it treats exchange energy, E_{x} exactly but completely neglects correlation energy, E_{corr}. From this drawback, DFT incorporates all terms of the unknown exchange and correlation energy including $T_{\text{corr}}[n(r)]$ and E_{corr} to be one term which is called exchange-correlation energy, $E_{\text{xc}}[n(r)]$. Therefore, the total energy of many-body systems can be expressed as

$$E[n(r)] = T_{\text{non}}[n(r)] + \frac{1}{2} \iint \frac{n(r)n(r')}{|r-r'|} dr dr'$$

$$- \sum_{I=1}^{N} \int \frac{Z_I n(r)}{|R_I - r|} dr + E_{\text{xc}}[n(r)]. \tag{2.1}$$

From Equation 2.1, the first term is the kinetic energy of non-interacting electrons, the second term is the potential energy of interaction between electron and electron, the third term is the potential energy of interaction between nucleus and electron, and the last term is the exchange-correlation energy.

Based on the second Hohenberg-Kohn theorem, the ground-state energy of the system can be calculated by minimizing the term of total energy (Equation 2.1) with the ground-state electron density. The condition for obtaining the lowest total energy can be defined as

$$\left[-\frac{\nabla_i^2}{2} + V_{\text{eff}}[n(r)]\right]\Psi_i^{\text{KS}}(r) = E_i\Psi_i^{\text{KS}}(r). \tag{2.2}$$

The Equation 2.2 is called the Kohn-Sham equation where $-\frac{\nabla_i^2}{2}$ is the kinetic energy operator of electrons in atomic units, $V_{\text{eff}}[n(r)]$ is the effective potential, $\Psi_i^{\text{KS}}(r)$ is the Kohn-Sham orbital (the electron density that obtained by the Kohn-Sham orbital is the corrected density for many-body systems), i is band index (in general, the value of i is ranged from one to the number of occupied electron bands which is equal to a half of the total number of electrons), and E_i is the energy that corresponds to band index.

The effective potential can be written as

$$V_{\text{eff}}[n(r)] = V_{\text{H}}[n(r)] + V_{\text{ext}}[n(r)] + V_{\text{xc}}[n(r)]$$

$$= \frac{1}{2}\int\frac{n(r')}{|r-r'|}dr' - \sum_{I=1}^{N}\int\frac{Z_I}{|R_I-r|}dr + V_{\text{xc}}[n(r)], \tag{2.3}$$

where $V_{\text{H}}[n(r)]$ is the Hartree potential (potential of interaction between electron and electron), $V_{\text{ext}}[n(r)]$ is the external potential (potential of interaction between nucleus and electron), and $V_{\text{xc}}[n(r)]$ is the exchange-correlation potential which can be expressed as

$$V_{\text{xc}}[n(r)] = \frac{\delta E_{\text{xc}}[n(r)]}{\delta n}. \tag{2.4}$$

To solve the Kohn-Sham equation, we have to know the effective potential first. However, there exist the unknown exchange-correlation term in the

effective potential. Hence, it is essential to know the exact form of exchange-correlation energy which are mentioned in the section below.

2.1.3 Exchange-correlation energy

DFT is the effective method that provides us the accurate results if we know the correct form of exchange-correlation energy. However, the main problem of this theory is that the exchange-correlation energy is not known exactly. Therefore, many researchers have proposed several forms of this energy that give the results of calculations matching with the experimental results. The common form of exact exchange-correlation energy can be defined as

$$E_{xc}[n(r) = \int \varepsilon_{xc} n(r) dr = \int (\varepsilon_x + \varepsilon_c) n(r) dr, \qquad (2.5)$$

where ε_{xc} is the exchange-correlation energy density, ε_x is the exchange energy density, and ε_c is the correlation energy density.

There are two most widely used exchange-correlation energy, namely the local density approximation and the generalized gradient approximation.

(1) Local density approximation (LDA)

This approximation is based on the homogeneous electron gas where exchange energy density of LDA can be expressed as

$$\varepsilon_x^{LDA}[n(r)] = -\frac{3}{4}\left(\frac{3}{\pi}\right)^{\frac{1}{3}} n^{\frac{1}{3}}(r). \qquad (2.6)$$

For the correlation energy density, it is not known exactly now. In practical, the correlation energy density are parametrizations of highly precise Quantum Monte Carlo simulations (Ceperley and Alder, 1980). Since the atomic and molecular systems spatially inhomogeneous which differ from the uniform electron gas, this approach is not quite correct. However, it still works fine for the case of homogeneous system.

(2) Generalized gradient approximation (GGA)

In fact, the electron density in the vicinity of nucleus is high while the electron density that far away from nucleus is low. Thus, the electron density is not uniform at any position that means there exist the gradient of the electron density, $\nabla n(r)$. The exchange-correlation energy of GGA consists of the terms that depend on the electron density and the gradient of the electron density. There are various commonly used forms of GGA. The most popular GGAs are BLYP which was denoted the combination of the exchange functional by Becke and the correlation functional of Lee, Yang and Parr, both in 1988 (Becke, 1988) and PBE where this functional was proposed in 1996 by Perdew, Burke and Ernzerhof (John P Perdew *et al.*, 1996). In this thesis, the exchange-correlation energy was approximated using the PBE form. The exchange energy density of PBE can be written as

$$\varepsilon_{\mathrm{x}}^{\mathrm{PBE}}[n(r), \nabla n(r)] = -\frac{3}{4}\left(\frac{3}{\pi}\right)^{\frac{1}{3}} n^{\frac{1}{3}}(r) F(x), \tag{2.7}$$

where

$$F(x) = 1 + a - \frac{a}{1+bx^2}, \tag{2.8}$$

$$x = \frac{|\nabla n(r)|}{n^{\frac{4}{3}}(r)} \tag{2.9}$$

when a and b are constant.

The correlation energy density of PBE is based on the correlation energy density of LDA where the effect of the gradient of the electron density is applied ($H[n(r), \nabla n(r)]$). For the non-magnetic systems, the correlation energy density can be written as

$$\varepsilon_{\mathrm{c}}^{\mathrm{PBE}}[n(r), \nabla n(r)] = \varepsilon_{\mathrm{c}}^{\mathrm{LDA}}[n(r)] + H[n(r), \nabla n(r)], \tag{2.10}$$

where

$$H[n(r), \nabla n(r)] = c \ln \left[1 + dt^2 \left(\frac{1+At^2}{1+At^2+A^2t^4} \right) \right], \tag{2.11}$$

$$A = d \left[\exp \left(\frac{\varepsilon_c^{\text{LDA}}[n(r)]}{c} \right) - 1 \right]^{-1}, \tag{2.12}$$

$$t = \frac{x}{2(3\pi^2)^{\frac{1}{3}}} = \frac{\nabla n(r)}{2(3\pi^2)^{\frac{1}{3}} n^{\frac{4}{3}}(r)}, \tag{2.13}$$

when c and d are constant.

2.1.4 Pseudopotential

One of the important quantities in the Kohn-Sham equation is the effective potential which consists of the Hartree, external, and exchange-correlation potentials. The Hartree and external potentials are inversely proportional to the distance between the particles, r. The problem of these two potentials is that when the distance between the particles is small, the wavefunction in this area exhibits the strong oscillation. This requires large number of basis functions to perform the wavefunction in this region, leading to the use of high computational resources and excessive computational times. To overcome this problem, the pseudopotential was proposed. The relation between real potential, V and pseudopotential, V_{pseudo} and the relation between real wavefunction, Ψ and pseudo wavefunction, Ψ_{pseudo} as a function of the distance between the particles are shown in Figure 2.1. It can be seen that $V = V_{\text{pseudo}}$ and $\Psi = \Psi_{\text{pseudo}}$ when $r > r_c$, where r_c is cut-off radius while $V \neq V_{\text{pseudo}}$ and $\Psi \neq \Psi_{\text{pseudo}}$ when $r \leq r_c$. In addition, it can be obviously found that Ψ displays the strong oscillation when $r \leq r_c$. Therefore, it is difficult to solve the Schrödinger equation in this region. To solve such problem, it is essential to make wavefunction in this area smooth which are regarded as Ψ_{pseudo} (red line in Figure 2.1), where the suitable Ψ_{pseudo} has to meet the definitions as follows.

1. When $r \geq r_c$, the pseudo wavefunction and real wavefunction must be the same and the total energy of pseudopotential must be equal to the corrected total energy or total energy of all electrons.

2. The pseudo wavefunction and real wavefunction must be continuous at $r = r_c$.

3. The generated pseudo wavefunction must have the spherical charge of r_c which is equal to that of real wavefunction.

4. The generated pseudopotential is needed to apply to the comparable problems.

5. For the element that exists a large number of electrons, it is required to incorporate the relativistic property into the generated pseudopotential.
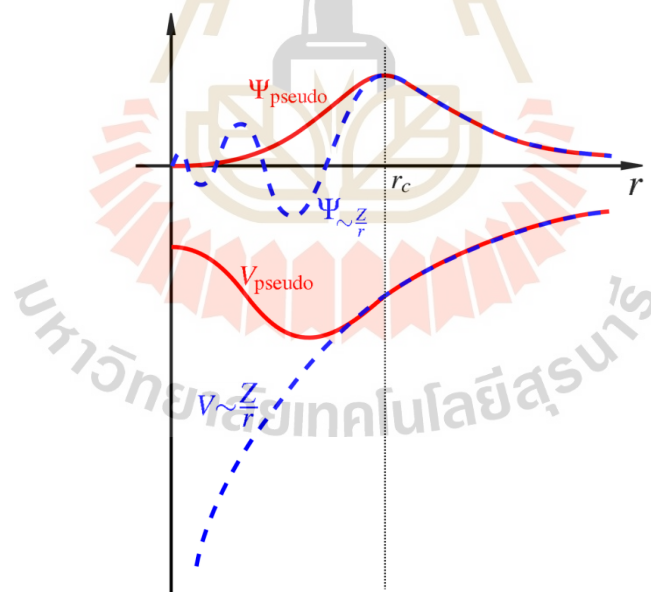
Figure 2.1 Relation between real potential, V and pseudopotential, V_{pseudo}; between real wavefunction, Ψ and pseudo wavefunction, Ψ_{pseudo} as a function of the distance between the particles (Payne *et al.*, 1992).

There are three commonly used types of pseudopotential: norm-conserving (Hamann *et al.*, 1979); ultrasoft (Vanderbilt, 1990); and projector-augmented wave (PAW) (Blöchl, 1994; Kresse and Joubert, 1999). In this thesis, we used PAW pseudopotential to describe electron-ion interactions. This method uses a smooth wavefunction to describe the electrons near the nucleus or the core region, C, which is a good approximation since only the valence electrons are responsible for the interatomic interactions. In this method, the pseudo wavefunctions are transformed by an operator $\hat{T}$ into the real Kohn-Sham single particle wave functions (Blöchl, 1994; Kresse and Joubert, 1999)

$$|\Psi\rangle = \hat{T}|\Psi'\rangle, \qquad (2.14)$$

where $|\Psi\rangle$ is the real single particle wavefunction and $|\Psi'\rangle$ is the pseudo wavefunction. The operator $\hat{T}$ can be constructed by considering that the wavefunctions have to be the same outside the core region. For inside the core region, it can be created with the smoother partial waves

$$|\Psi'\rangle = \sum_i |\phi_i'\rangle c_i. \qquad (2.15)$$

The total single particle wavefunction outside and inside the core region can be written as the following equation

$$|\Psi\rangle = \sum_i |\phi_i\rangle c_i = \hat{T}|\Psi'\rangle, \qquad (2.16)$$

where

$$\hat{T} = 1 + \sum_C T_C \quad (T_C \text{ only acts inside C}), \qquad (2.17)$$

$$c_i = \langle \hat{p}_i | \Psi' \rangle, \qquad (2.18)$$

$$\langle \hat{p}_i | \phi_j' \rangle = \delta_{ij}, \qquad (2.19)$$

$$\sum_i |\phi_i'\rangle \langle \hat{p}_i| = 1, \qquad (2.20)$$

$$T_C |\Psi'\rangle = \sum_i T_C |\phi_i'\rangle c_i = \sum_i (|\phi_i\rangle - |\phi_i'\rangle) \langle \hat{p}_i | \Psi' \rangle, \qquad (2.21)$$

$$\hat{T} = 1 + \sum_i (|\phi_i\rangle - |\phi_i'\rangle)\langle\hat{p}_i|. \tag{2.22}$$

The transformation of the pseudo wavefunctions into real functions has to be linear. This means that it is possible to project the coefficients from the operator $\hat{p}_i$ according to Equation 2.18. If we consider that Equation 2.19 and 2.20 define the operator $\hat{p}_i$, while using Equation 2.15 and 2.18, we finally end up with Equation 2.21 within the core region with Equation 2.22 that originates from Equation 2.16 (Wärnå, 2019).

2.1.5 Bloch's Theorem

A crystal is a form of solid where the atoms are arranged in a regular repeating pattern called a crystal lattice. This makes the potential energy of the crystalline solid possess the periodic character. Nevertheless, the complexity of this problem can be reduced by using Bloch's Theorem (Kittel *et al.*, 1996). This theorem establishes that the wavefunction of a crystal can be expressed as the product of a plane wave and a function that has the same periodicity as the lattice, $u_k(r)$, i.e.,

$$\Psi_k(r) = u_k(r)e^{ik\cdot r}, \tag{2.23}$$

where k is the wave vector in the reciprocal lattice or Brillouin zone of the crystal and r is the position of atom in the unit cell of the crystal. The wavefunction of the crystal that has the periodicity can be written as

$$u_k(r) = \sum_G c_{k+G}e^{iG\cdot r}, \tag{2.24}$$

where c_{k+G} is constant and G is any vector that distributes in the reciprocal lattice, $G = m_1 a' + m_2 b' + m_3 c'$ where m_1, m_2, and m_3 are the positive integers; a', b', and c' are reciprocal lattice vectors. When we substitute the periodic wavefunction into Bloch's Theorem, the wavefunction of the crystal can be written as

$$\Psi_k(r) = \sum_G c_{k+G}e^{i(k+G)\cdot r}. \tag{2.25}$$

Therefore, the Kohn-Sham orbital of the crystal in DFT can be expressed as

$$\Psi_k^{KS}(r) = \sum_G c_{k+G} e^{i(k+G)\cdot r}. \tag{2.26}$$

From Equation 2.26, the value of G should be defined to distribute over the reciprocal lattice; in other words, the value of G should be infinity. However, we cannot do that in a practical manner. Thus, the value of G can be cut out at the high energy. This can be done because the properties of the materials correspond to the low-energy range (energy near Fermi energy), while the high-energy range does not affect the properties of the materials. Here, the highest value of G can be defined as G_{cut} and G_{cut} relates to the cutoff energy in the atomic unit as follows

$$E_{\text{cut}} = \frac{|k+G_{\text{cut}}|^2}{2}. \tag{2.27}$$

Therefore, the Kohn-Sham orbital of the crystal can be rewritten as

$$\Psi_k^{KS}(r) = \sum_{G_i < |G_{cut}|} c_{k+G_i} e^{i(k+G_i)\cdot r}. \tag{2.28}$$

Assuming that $|G_{cut}|$ relates to the number of plane wave, N_G, Equation 2.28 can be rewritten as

$$\Psi_k^{KS}(r) = \sum_{G_i=1}^{N_G} c_{k+G_i} e^{i(k+G_i)\cdot r}. \tag{2.29}$$

In order to calculate the energy at each k and the set of coefficient c_{k+G_i}, the secular equation for the crystal have to be constructed as

$$\sum_{G_i=1}^{N_G} \mathcal{H}_{G_j,G_i} c_{k+G_i} = \sum_{G_i=1}^{N_G} \epsilon(k) S_{G_j,G_i} c_{k+G_i}. \tag{2.30}$$

When we solve this secular equation (Equation 2.30), we obtain the eigen value and the Kohn-Sham orbital for each N_G at k. The relation between the eigen value and wave vector, $k = k_1$ are shown in Figure 2.2(a). When we change the value of k such as $k = k_1$, k_2, k_3, k_4, and k_5, the relation between the eigen values and wave vectors are illustrated as Figure 2.2(b), which is known as the band structure. Besides the band structure obtained by solving the secular equation, there is one quantity that can be

achieved automatically when we know the band structure, namely the density of states

of electrons, $n(\epsilon)$. This quantity can be calculated from the band structure as

$$n(\epsilon) = \sum_k \delta(\epsilon - \epsilon(k)), \tag{2.31}$$

where $\delta(\epsilon - \epsilon(k))$ is the Dirac delta function which is equal to zero for every ϵ, except

$\epsilon = \epsilon(k)$.
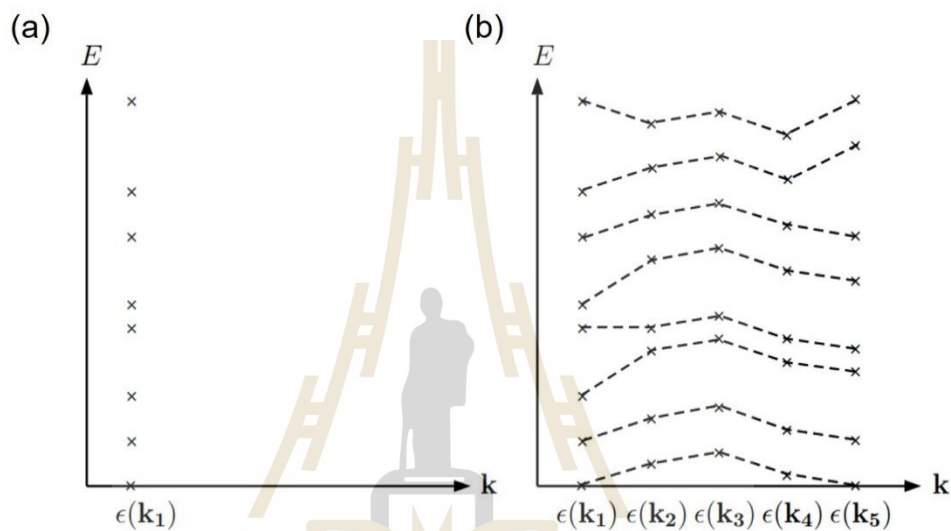
Figure 2.2 Relation between the eigen value and wave vector, k (a) one point (b) five

points, where $N_G = 8$ and the dashed line is the line which links between the points

that have the same value of N_G (Srepusharawoot, 2016).

The accuracy of the results from calculations depends on the number of

basis functions that perform the Kohn-Sham orbital. From Equation 2.29, the quantities

that relate to the number of these basis functions are N_G and k. This means that if these

two variables have large values, the obtained computational results are highly accurate

but it requires the extensive computational times. On the other hand, when the value of

the two variables is small, the obtained results are less accurate but it use low

computational times. In order to get the accurate results with low computational times,

we have to find the appropriate value of N_G and k. It is well known that the value of N_G corresponds to the cut-off energy. Therefore, the suitable value of N_G relates to the reasonable value of the cut-off energy. The way to find the appropriate value of the cut-off energy can be accomplished as follows.

1. Calculating the total energy of considered system at various cut-off energies.

2. Plotting graph of the relation between the total energy and cut-off energy where the reasonable value of the cut-off energy is the lowest cut-off energy that makes the total energy consistent.

From Equation 2.29, another variable needed to consider for finding the suitable value is k. Here, we can use the number of points in Brillouin zone (k-points), n_k to represent variable k. The means to find the reasonable value of n_k can be achieved as follows.

1. Determining the appropriate cut-off energy for the calculations.

2. Calculating the total energy which corresponds to various n_k.

3. Plotting graph of the relation between the total energy and n_k where the acceptable value of n_k is the lowest number of k-points in Brillouin zone that makes the total energy consistent.

2.1.6 Self-Consistent Field calculation

In practice, the ground-state energy in DFT can be obtained by Self-Consistent Field calculation. This calculation is the method to find the ground-state density which is the fundamental quantity for calculating the physical quantities such as energy, force, and stress. The step of Self-Consistent Field calculation are demonstrated in Figure 2.3 and the details are as follows.
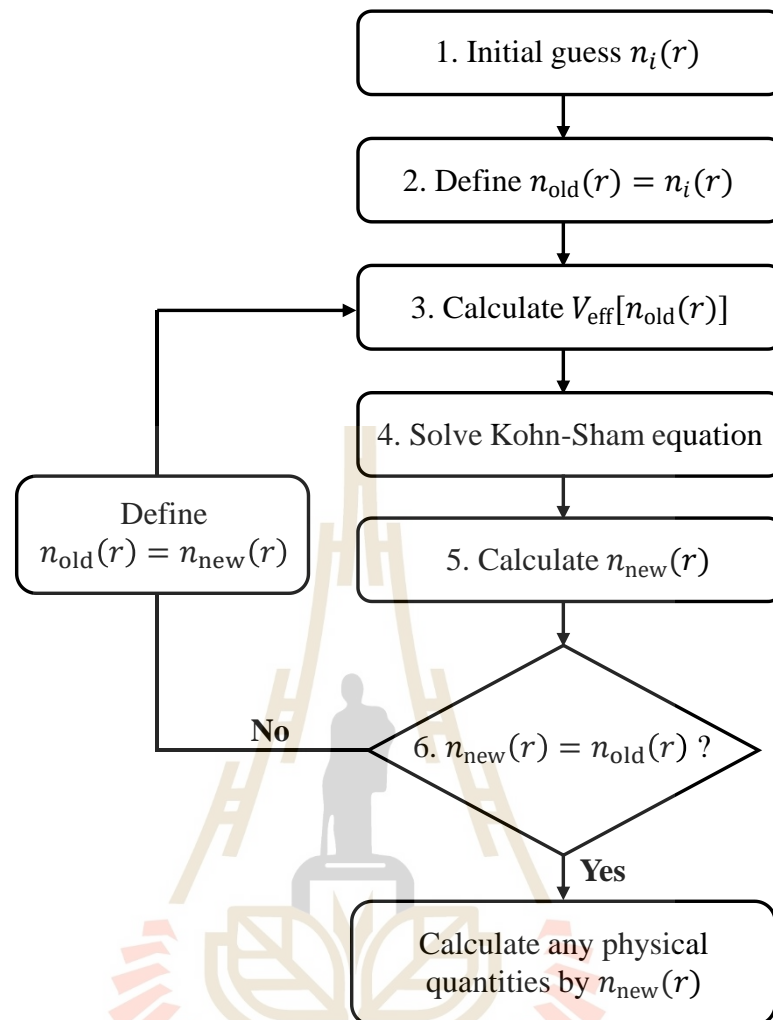
Figure 2.3 Self-Consistent Field calculation in DFT.

Modified from Ref. (Srepusharawoot, 2016).

1. Guessing the initial electron density, $n_i(r)$.

2. Determining the old electron density, $n_{\text{old}}(r) = n_i(r)$.

3. Taking $n_{\text{old}}(r)$ to calculate the effective potential, $V_{\text{eff}}[n_{\text{old}}(r)]$.

4. Substituting the obtained effective potential into the Kohn-Sham equation and solving such equation to get the Kohn-Sham orbital and eigenvalues.

5. Taking the obtained Kohn-Sham orbital to calculate the new electron density, $n_{\text{new}}(r)$.

6. Comparing between $n_{\text{old}}(r) = n_{\text{new}}(r)$:

- If $n_{\text{old}}(r) = n_{\text{new}}(r)$, the ground-state electron density is $n_{\text{new}}(r)$ where it is used to calculate any physical quantities.

- If $n_{\text{old}}(r) \neq n_{\text{new}}(r)$, $n_{\text{old}}(r) = n_{\text{new}}(r)$ is defined and the step 3 to 6 are repeated until $n_{\text{old}}(r) = n_{\text{new}}(r)$.

2.1.7 Hellmann-Feynman Theorem

Force theorem is the theorem for calculating the force between ions in quantum mechanics. The force acting on ions, I can be calculated as

$$F_I = -\nabla_I E_{\text{tot}} = -\frac{dE_{\text{tot}}}{dR_I}, \tag{2.32}$$

where E_{tot} is the total energy of electron and nucleus in many-body system and R_I is the position of ion I. In DFT, the total energy of many-body system based on Born-Oppenheimer approximation can be written as

$$E_{\text{tot}} = T + E_{\text{ee}} + E_{\text{Ne}} + E_{\text{NN}}$$
$$= E + E_{\text{NN}}, \tag{2.33}$$

where T, E_{ee}, E_{Ne}, and E_{NN} is the kinetic energy of electron, the potential energy of electron-electron interaction, nucleus-electron interaction, and nucleus-nucleus interaction, respectively and E is the total energy that corresponds to electron only. Therefore, the force between ions can be written in terms of such energies as

$$F_I = -\frac{d(E+E_{\text{NN}})}{dR_I}$$
$$= -\frac{dE}{dR_I} - \frac{dE_{\text{NN}}}{dR_I}. \tag{2.34}$$

If Ψ is wavefunction (Kohn-Sham orbital) of electron, the total energy of electron can be expressed as

$$E = \langle \Psi | \hat{H} | \Psi \rangle = \int \Psi^* \hat{H} \Psi dr. \tag{2.35}$$

Substituting Equation 2.35 into Equation 2.34, we get

$$F_I = -\frac{d}{dR_I} \int \Psi^* \widehat{H} \Psi dr - \frac{dE_{\text{NN}}}{dR_I}. \qquad (2.36)$$

Considering the first term in Equation 2.36, we get

$$-\frac{d}{dR_I} \int \Psi^* \widehat{H} \Psi dr = -\int \frac{d\Psi^*}{dR_I} \widehat{H} \Psi dr - \int \Psi^* \frac{d\widehat{H}}{dR_I} \Psi dr - \int \Psi^* \widehat{H} \frac{d\Psi}{dR_I} dr, \quad (2.37)$$

$$-\frac{d}{dR_I} \int \Psi^* \widehat{H} \Psi dr = -\left\langle \frac{d\Psi}{dR_I} \middle| \widehat{H} \middle| \Psi \right\rangle - \left\langle \Psi \middle| \frac{d\widehat{H}}{dR_I} \middle| \Psi \right\rangle - \left\langle \Psi \middle| \widehat{H} \middle| \frac{d\Psi}{dR_I} \right\rangle. \qquad (2.38)$$

From the property of Hermitian Hamiltonian as

$$\left\langle \Psi_1 \middle| \widehat{H} \middle| \Psi_1 \right\rangle = \left\langle \Psi_1 \middle| (\widehat{H}\Psi_1) \right\rangle = \left\langle (\widehat{H}\Psi_1) \middle| \Psi_1 \right\rangle = E\left\langle \Psi_1 \middle| \Psi_1 \right\rangle, \qquad (2.39)$$

Equation 2.38 can be written as

$$-\frac{d}{dR_I} \int \Psi^* \widehat{H} \Psi dr = -\left[E \frac{d}{dR_I} \langle \Psi | \Psi \rangle + \left\langle \Psi \middle| \frac{d\widehat{H}}{dR_I} \middle| \Psi \right\rangle \right]. \qquad (2.40)$$

From the property of orthonormal wavefunction as $\langle \Psi | \Psi \rangle = 1$, $\frac{d}{dR_I} \langle \Psi | \Psi \rangle = 0$,

Equation 2.40 can be rewritten as

$$-\frac{d}{dR_I} \int \Psi^* \widehat{H} \Psi dr = -\left\langle \Psi \middle| \frac{d\widehat{H}}{dR_I} \middle| \Psi \right\rangle = -\int \Psi^* \frac{d\widehat{H}}{dR_I} \Psi dr. \qquad (2.41)$$

It is well known that the kinetic energy of electron and potential energy of electron-electron interaction depend on the position of electron only. Therefore, the derivative of these energies with respect to the position of nucleus is zero. Then, we get

$$-\frac{d}{dR_I} \int \Psi^* \widehat{H} \Psi dr = -\int \Psi^* \frac{dE_{\text{Ne}}}{dR_I} \Psi dr. \qquad (2.42)$$

Thus, the force acting on ions can be written as

$$F_I = -\int \Psi^* \frac{dE_{\text{Ne}}}{dR_I} \Psi dr - \frac{dE_{\text{NN}}}{dR_I}. \qquad (2.43)$$

Equation 2.43 is the well-known Hellmann-Feynman Theorem (Hellmann, 1937).

2.1.8 Optimization

Optimization is the method to move the atoms or ions to the positions that possess the lowest total energy of the positions that make the net force zero. The process of optimization in DFT is the combination of the process of ion position change and Self-Consistent Field calculation. The step of optimization are displayed in Figure 2.4 and the details are as follows.
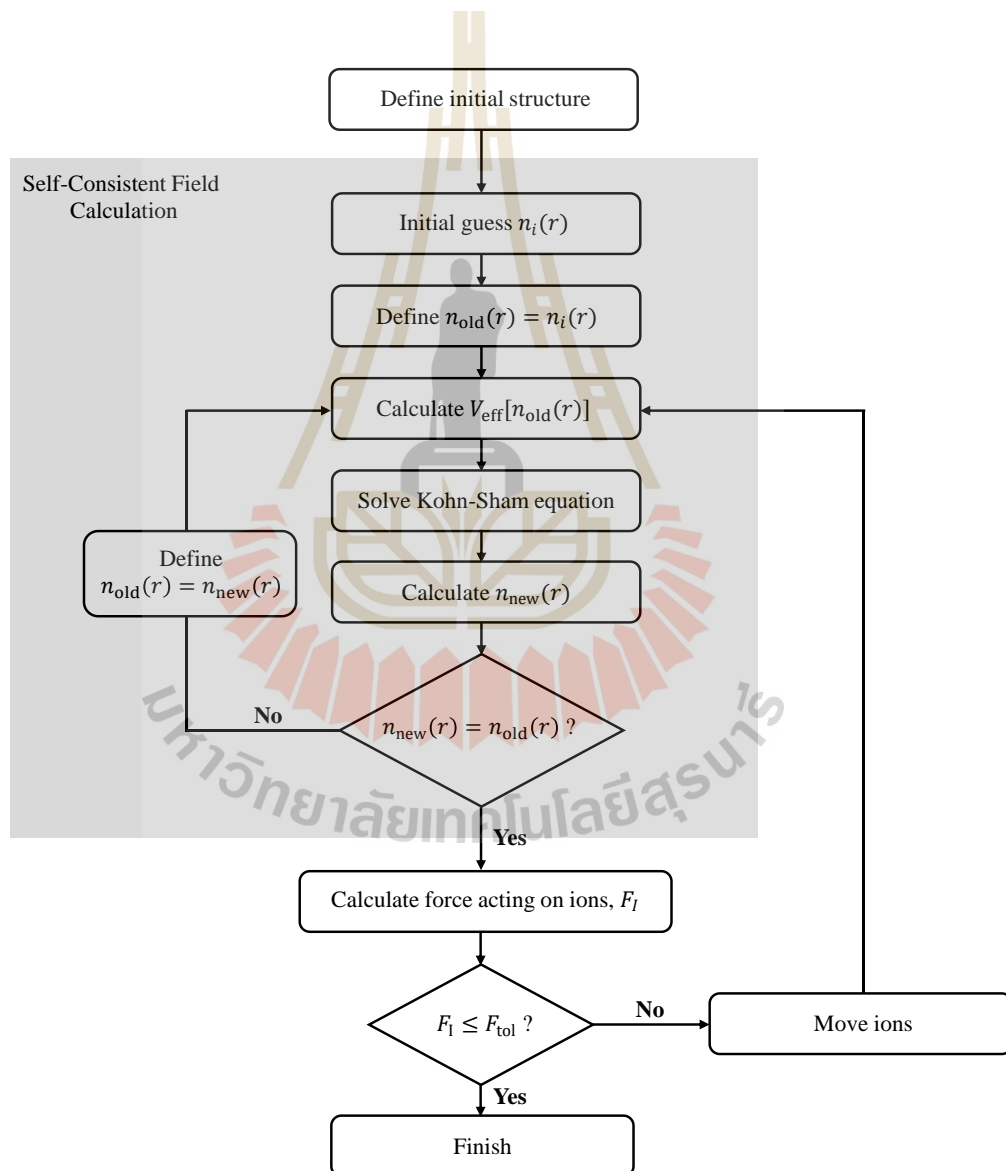
Figure 2.4 Optimization process in DFT.

Modified from Ref. (Srepusharawoot, 2016).

1. Defining the initial structure for optimization.

2. Self-Consistent Field calculation for getting the eigenvalues and the Kohn-Sham orbital that correspond to such structure.

3. Taking the obtained Kohn-Sham orbital to calculate the force between ions, F_I.

4. Comparing between F_I obtained from step 4 and F_{tol} (in this thesis, F_{tol} was set to be 0.02 eV/Å):

- If $F_I \leq F_{tol}$, the process of optimization is finished where the last position of atoms is the position of atoms for optimized structure.

- If $F_I > F_{tol}$, the atoms are moved to the direction that dominates the lowest total energy. Then, the processes go through the Self-Consistent Field calculation again and are repeated until $F_I \leq F_{tol}$.

2.1.9 Pros and cons of DFT

Currently, DFT is a very powerful method for understanding and predicting material properties starting from the first-principles of quantum mechanics. Despite the success and widespread use of DFT, it only addresses the electronic ground state of materials where it is not designed to describe electronic excitations and non-equilibrium phenomena (Giustino, 2014).

The material properties which can be calculated with good accuracy using DFT are as follows:

- equilibrium structures

- vibrational properties and vibrational spectra

- binding energies of molecules and cohesive energies of solids

- ionization potential and electron affinity of molecules

- band structures of metals and semiconductors.

The material properties that cannot be calculated reliably using DFT are as follows:

- electronic band gaps of semiconductors and insulators

- magnetic properties of Mott-Hubbard insulators (mostly systems with atomic-like localized d or f electronic states)

- bonding and structure in sparse matter, e.g. proteins, where van der Waals forces are important.

2.2   DFT+U method

As described in the previous section, DFT is the computational tools for predicting the properties of different classes of materials in a good accuracy. Although its accuracy is acceptable for the structural and cohesive properties, it significantly fails in the prediction of the properties of strongly-correlated systems. Also, it is unsuccessful for calculating the polaron properties, as well. The problem of DFT to describe correlated systems can be ascribed to the tendency of exchange-correlation functionals to over-delocalize valence electrons and to over-stabilize metallic ground states (Cococcioni, 2012; Tolba *et al.*, 2018). That is why DFT fails dramatically in predicting the properties of systems whose ground state is characterized by a more pronounced localization of electrons. The reason behind this delocalization stems from the inability of the approximated exchange-correlation functionals to completely cancel out the electronic self-interaction contained in the Hartree term. Therefore, a remaining fragment of the same electron is still there which can induce added self-interaction, resulting in the excessive delocalization of the wavefunctions (Cococcioni, 2012;

Himmetoglu *et al.*, 2014; Tolba *et al.*, 2018). From this drawback, DFT+U method is formulated to improve the description of the ground state of correlated systems.

DFT+U method is inspired by the Hubbard model. This U correction treats the strong on-site Coulomb interaction of localized electrons with an additional Hubbard-like term. The Hubbard Hamiltonian describes the strongly correlated d and f electronic states while treating the rest of the valence electrons by the usual approximations of DFT. In practice, the on-site interaction strength is described by two parameters including the on-site Coulomb term U and the site exchange term J, which are empirically adjusted to match the experimental band gap (Deskins and Dupuis, 2007). The DFT+U performs in the same way as the conventional DFT method to describe the valence electrons, and only for the d and f orbitals. Therefore, within DFT+U the total energy of the system, $E_{\text{DFT+U}}$ can be written as (Himmetoglu *et al.*, 2014)

$$E_{\text{DFT+U}}[\rho(r)] = E_{\text{DFT}}[\rho(r)] + E_{\text{Hub}}[\{n_{mm'}^{I\sigma}\}] - E_{\text{dc}}[n^{I\sigma}], \qquad (2.44)$$

where E_{DFT} is the standard DFT energy functional for all the states and E_{Hub} is the energy of the Hubbard functional that describes the correlated states. Due to the additive Hubbard term, there is a double counting error for the correlated states; thus, a double-counting term, E_{dc} must be subtracted from the DFT energy that models the contribution of correlated electrons to the E_{DFT} as a mean-field approximation of E_{Hub} (Himmetoglu *et al.*, 2014). The E_{dc} term is not uniquely defined for each system and different formulations can be used in various systems. One of the most popular formulations is the FLL formulation (Vladimir I Anisimov *et al.*, 1997; Vlasdimir I Anisimov *et al.*, 1993; Liechtenstein *et al.*, 1995), which is based on the implementation of fully localized limit (FLL) on systems with more localized electrons on atomic orbitals. Based on the FLL formulation, the DFT+U can be written as

$$E_{\text{DFT}+\text{U}}[\rho(r)] = E_{\text{DFT}}[\rho(r)] + \sum_I \left[\frac{U^I}{2} \sum_{m,\sigma \neq m',\sigma'} n_m^{I\sigma} n_{m'}^{I\sigma'} - \frac{U^I}{2} n^I(n^I - 1) \right], \quad (2.45)$$

where $n_m^{I\sigma}$ are the occupation numbers of localized orbitals identified by the atomic site index I, state index m, and by the spin σ. The occupation number can be calculated from the projection of Kohn-Sham orbitals on the states of a localized basis set as (Himmetoglu *et al.*, 2014)

$$n_{m,m'}^{I\sigma} = \sum_{k,v} f_{kv}^{\sigma} \langle \Psi_{kv}^{\sigma} | \phi_{m'}^{I} \rangle \langle \phi_m^{I} | \Psi_{kv}^{\sigma} \rangle, \quad (2.46)$$

where the coefficients f_{kv}^{σ} is the occupations of Kohn-Sham states (labeled by k-point, band, and spin indices), determined by the Fermi-Dirac distribution of the corresponding single-particle energy eigen values.

In this thesis, we employed the Dudarev's approach (Dudarev *et al.*, 1998) for DFT+U calculations because we studied the $BiVO_4$ system, involving the transition metals with tightly bound d electrons, such as V atom. Nevertheless, there is no universal U value for holding every properties of every materials of interest. Therefore, we have to determine an appropriate U value to describe the properties of $BiVO_4$, including the electronic and polaron properties. The U value of 2.7 eV has been used to properly describe the behavior of polaron formation in the Mo/W-doped $BiVO_4$ (Park *et al.*, 2011). The calculated hopping barrier of 0.3 eV is consistent with the experimental determined value (0.29 eV) in W-doped $BiVO_4$ (Rettie *et al.*, 2013). To further ensure this U value that it is suitable for our system, we explored the band gap of $BiVO_4$; the polaron state in the band gap and the polaron hopping barrier for electron-doped $BiVO_4$ system by applying the values of U in the range between 1.7 and 10 eV. The results are summarized in Table 2.1 and demonstrated in Figure 2.5. Here, only one polaron hopping path was considered because the hopping barriers along various possible paths are equivalent. The energy barriers were obtained by the linear

interpolation method for saving computational costs, where this method performs a single-point energy calculations of each configuration along the migration path. This method is acceptable for this case because we first calculated the hopping barrier with U of 2.7 eV by linear interpolation method and Climbing image nudged elastic band (CI-NEB) method; then, we found that the barriers obtained from both methods are very comparable. However, we used a more acceptable method like CI-NEB to find the polaron hopping barrier in the main results. The details of CI-NEB method and polaron hopping model are described in the next section and in Chapter V, respectively.

Table 2.1 Calculated band gap of $BiVO_4$; the polaron state in the band gap and the polaron hopping barrier of electron-doped $BiVO_4$ for different U values.

U (eV)	Band gap (eV)	Polaron state (eV below CBM)	Energy barrier (eV)
1.7	2.12	0.52	0.17
2.7	2.17	1.03	0.30
3.7	2.22	1.44	0.34
4.7	2.28	1.82	0.36
6	2.38	2.21	0.38
8	2.55	no gap state	0.44
10	2.55	no gap state	0.47
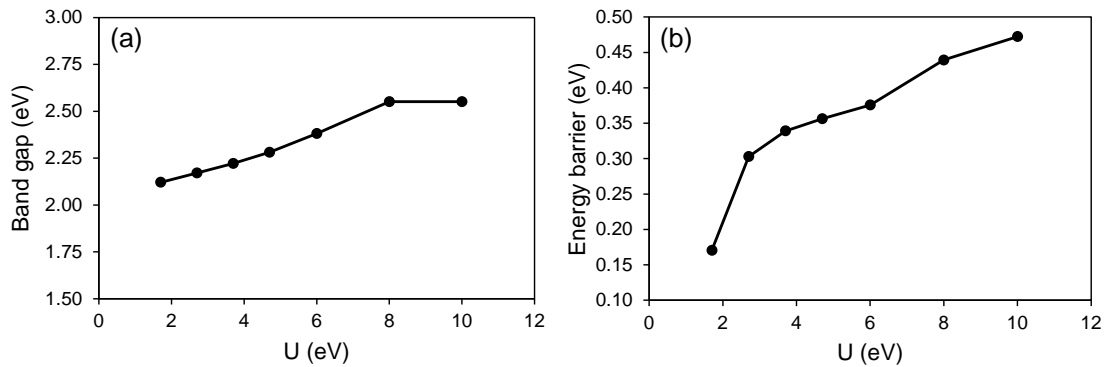
Figure 2.5 (a) Band gap of $BiVO_4$ (b) Polaron hopping barrier of electron-doped $BiVO_4$ at different U values.

From Table 2.1 and Figure 2.5, the band gap, polaron state, and energy barrier increase with increasing U value. In case of band gap, U = 6 eV gives the band gap of 2.38 eV which is in good agreement with experimental value of 2.4 eV (Kudo *et al.*, 1999; Tokunaga *et al.*, 2001). Above U values of 8 eV, the band gap tends to converge to 2.55 eV. For the polaron state, low U values give gap state near CBM while large U values give gap state near VBM. However, above U values of 8 eV, the polaron state is located in the VB which proves impossible. In case of polaron hopping barrier, U = 2.7 eV gives the energy barrier of 0.30 eV which is consistent with the result (0.3 eV) in the Mo/W-doped $BiVO_4$ from previous computational work (Park *et al.*, 2011) and the experimental value (0.29 eV) in W-doped $BiVO_4$ (Rettie *et al.*, 2013). Therefore, we chose U value of 2.7 eV for our study because it gives the accurate energy barrier and reasonable band gap (2.17 eV) and gap state. Moreover, we have confidence in this U value because our results show good agreement with the previous study (Park *et al.*, 2011).

2.3 Climbing image nudged elastic band (CI-NEB) method

The nudged elastic band (NEB) is a method for finding the saddle points and minimum energy paths (MEP) between a given initial and final states of a transition. The NEB has been used in conjunction with electronic structure calculations, in particular plane wave-based DFT. In this method, the MEP is found by constructing the images between the initial and final states. A spring interaction between adjacent images is added to ensure continuity of the path, thus mimicking an elastic band. An optimization of the band with the minimization of the force acting on the images brings the band to the MEP. Recently, CI-NEB method, a modification of the NEB method which gives a precise estimate of the saddle point, has been widely used. Also, in this thesis, we used CI-NEB method to determine the saddle point of polaron transfer. The brief details of regular NEB and CI-NEB method are given below.

2.3.1 Regular NEB method

An elastic band with N+1 images can be denoted as $[R_0, R_1, R_2, \ldots, R_N]$, where R_0 and R_N are fixed and given by the energy minima for the initial and final states, respectively, while the intermediate images are adjusted by optimization. The total force acting on the images can be expressed as (Henkelman *et al.*, 2000)

$$F_i = F_i^s|_\parallel - \nabla E(R_i)|_\perp, \tag{2.47}$$

where $F_i^s|_\parallel$ and $\nabla E(R_i)|_\perp$ are the spring force along the local tangent and the true force perpendicular to the local tangent, respectively. The true force is given by

$$\nabla E(R_i)|_\perp = \nabla E(R_i) - \nabla E(R_i) \cdot \hat{\tau}_i, \tag{2.48}$$

where E is the energy of the system and $\hat{\tau}_i$ is the normalized tangent at image i.
The spring force is given by

$$F_i^s|_\parallel = k(|R_{i+1} - R_i| - |R_i - R_{i-1}|)\hat{\tau}_i, \tag{2.49}$$

where k is the spring constant. The images are optimized according to the force in Equation 2.47. The images converge on the MEP with equal spacing if the spring constant is the same for all the springs. As the images do not land at or even near the saddle point typically, the activation energy needs to be estimated by interpolation.

2.3.2 CI-NEB method

In this approach, the information about the shape of the MEP is maintained whereas a precise convergence to a saddle point is obtained. After a few iterations with the regular NEB, the highest energy image, $i_{\max}$ is identified. The force on this image is given by (Henkelman *et al.*, 2000)

$$
\begin{aligned}
F_{i_{\max}} &= -\nabla E(R_{i_{\max}}) + 2\nabla E(R_{i_{\max}})|_{\parallel} \\
&= -\nabla E(R_{i_{\max}}) + 2\nabla E(R_{i_{\max}}) \cdot \hat{\tau}_{i_{\max}} \hat{\tau}_{i_{\max}}.
\end{aligned} \tag{2.50}
$$

This image does not feel the spring forces at all, the true force at this image along the tangent is inverted instead. The image tries to maximize its energy along the band and minimize in all other directions. When this image converges, it is at the exact saddle point.

An example of NEB and CI-NEB calculations is shown in Figure 2.6. In can be seen that the regular NEB results in a low resolution of the barrier, and the interpolation gives an underestimate of the activation energy. The CI-NEB brings one of the images right to the saddle point and gives the accurate activation energy.
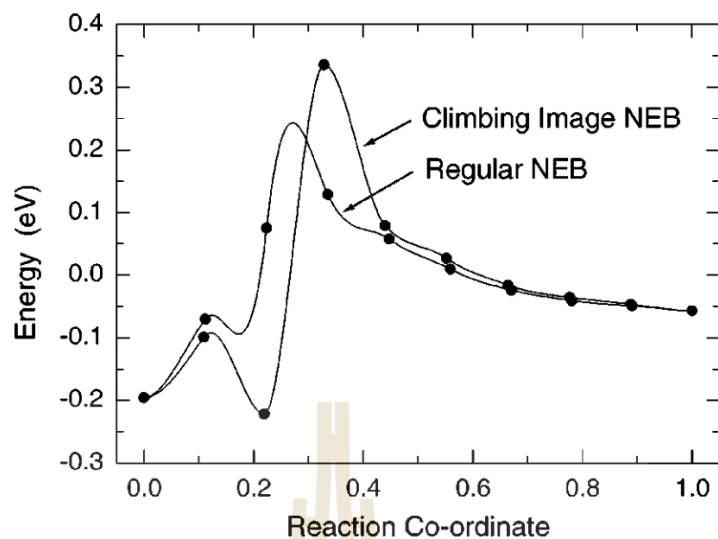
Figure 2.6 DFT calculations of the minimum energy path for CH$_4$ dissociative
adsorption on Ir(111) surface. The dissociated H and CH$_3$ fragments sitting on adjacent
on-top sites correspond to reaction coordinate of 0.0. The CH$_4$ molecule 4 Å away from
the surface corresponds to 1.0. Both NEB and CI-NEB calculations involve 8 movable
images (Henkelman *et al.*, 2000).

2.4   A Summary of computational details

We carried out first-principles calculations using the spin-polarized DFT+U
approach with periodic supercell model as implemented in the Vienna Ab Initio
Simulation Package (VASP 5.3) (Kresse and Furthmüller, 1996a, 1996b; Kresse and
Hafner, 1993). The PAW method (Blöchl, 1994; Kresse and Joubert, 1999) was used to
describe electron-ion interactions where Bi $5d^{10}6s^26p^3$, V $3p^63d^34s^2$, O $2s^22p^4$, and
P $3s^23p^3$ were treated as valence electrons. Their wavefunctions were expanded in the
plane-wave basis with a cutoff energy of 450 eV. The exchange-correlation functional
was approximated using the GGA in the form of PBE version (John P. Perdew *et al.*,
1996). We employed the Dudarev's approach (Dudarev *et al.*, 1998) for DFT+U

calculations with $U_{3d}(V) = 2.7$ eV (Park *et al.*, 2011) to correct for the self-interaction error inherent in the current exchange-correlation functional. A Gaussian smearing technique ($\sigma = 0.05$ eV) was used during structural relaxations where the calculated energies were extrapolated to zero smearing width.

To study the role of P doping on the reducibility and transport properties of charge carriers in the BiVO$_4$ lattice, we constructed a $3\times3\times1$ supercell of Bi$_{36}$V$_{36}$O$_{144}$ using the experimental lattice parameters of *ms*-BiVO$_4$ unit cell (Sleight *et al.*, 1979). The supercell model contains 216 atoms which corresponds to 36 BiVO$_4$ formula units. The P-doped BiVO$_4$ system was created by replacing a V atom with a P atom to yield a 2.8% doping concentration which is in the range of experimental values (Jo *et al.*, 2012; Liu *et al.*, 2014; Xia *et al.*, 2018). Most stable oxygen vacancy structures for pristine and doped systems were achieved by removing an O atom at various possible positions where the lowest energy structures were identified. For structural optimization, we sampled the Brillouin zone with a single k-point at Gamma position. Internal coordinates were relaxed until the forces were smaller than 0.02 eV/Å. We used the tetrahedron smearing method with Bloch corrections with a denser k-point grid of $2\times2\times2$ Gamma-centered to accurately calculate PDOS. Furthermore, the high frequency and static dielectric constants were computed using the $2\times2\times1$ supercell with the density functional perturbation theory (Baroni *et al.*, 2001).

In this thesis, polaron migration was described by the transfer of electron accompanied by the lattice distortion along a one-dimensional trajectory on the Born-Oppenheimer surface (Maxisch *et al.*, 2006). We adopted the CI-NEB method (Henkelman *et al.*, 2000) to determine the minimum energy path of polaron transfer. The CI-NEB approach allows for ionic relaxation of each configuration along the

migration path. The transition state (TS) is located at the saddle point of the reaction coordinate where the energy difference between TS and the initial state yields the migration barrier. The calculated barriers are considered adiabatic because this method implies the validity of Born-Oppenheimer approximation. Various possible migration paths were examined to understand behavior of electron polarons in the pristine and doped systems, in the presence and absence of an oxygen vacancy. In addition, the kinetic Monte Carlo (kMC) simulations were carried out to take into account the anisotropic hopping in pristine and doped systems. We used the kMC algorithm (see detail in APPENDIX A) reported by Wu and Ping (Wu and Ping, 2018) to estimate the polaron mobilities. The hopping rate and the distance between two nearest neighbor lattice sites throughout the lattice were included in the simulation.

2.5   References

Anisimov, V. I., Aryasetiawan, F. and Lichtenstein, A. (1997). First-principles calculations of the electronic structure and spectra of strongly correlated systems: the LDA+ U method. **J. Phys.: Condens. Matter.** 9: 767.

Anisimov, V. I., Solovyev, I., Korotin, M., Czyżyk, M. and Sawatzky, G. (1993). Density-functional theory and NiO photoemission spectra. **Phys. Rev. B.** 48: 16929.

Baroni, S., de Gironcoli, S., Dal Corso, A. and Giannozzi, P. (2001). Phonons and Related Crystal Properties from Density-Functional Perturbation Theory. **Rev. Mod. Phys.** 73: 515.

Becke, A. D. (1988). Correlation energy of an inhomogeneous electron gas: a coordinate-space model. **J. Chem. Phys.** 88: 1053.

Blöchl, P. E. (1994). Projector Augmented-Wave Method. **Phys. Rev. B.** 50: 17953.

Ceperley, D. M. and Alder, B. J. (1980). Ground state of the electron gas by a stochastic method. **Phys. Rev. Lett.** 45: 566.

Cococcioni, M. (2012). **In Correlated Electrons: From Models to Materials**. Pavarini, E., Koch, E., Anders, F., Jarrell, M., Eds.

Deskins, N. A. and Dupuis, M. (2007). Electron transport via polaron hopping in bulk TiO_2: A density functional theory characterization. **Phys. Rev. B.** 75: 195212.

Dudarev, S. L., Botton, G. A., Savrasov, S. Y., Humphreys, C. J. and Sutton, A. P. (1998). Electron-Energy-Loss Spectra and the Structural Stability of Nickel Oxide: An LSDA+U Study. **Phys. Rev. B.** 57: 1505.

Fock, V. (1930). Näherungsmethode zur Lösung des quantenmechanischen Mehrkörperproblems. **Z. Phys.** 61: 126.

Giustino, F. (2014). **Materials modelling using density functional theory: properties and predictions**: Oxford University Press.

Hamann, D., Schlüter, M. and Chiang, C. (1979). Norm-conserving pseudopotentials. **Phys. Rev. Lett.** 43: 1494.

Hartree, D. R. (1928). The Wave Mechanics of an Atom with a Non-Coulomb Central Field. Part I. Theory and Methods. **Math. Proc. Camb. Philos. Soc.** 24: 89.

Hellmann, H. (1937). **Einführung in die Quantenchemie**. Leipzig: Denticke.

Henkelman, G., Uberuaga, B. P. and Jónsson, H. (2000). A climbing image nudged elastic band method for finding saddle points and minimum energy paths. **J. Chem. Phys.** 113: 9901.

Himmetoglu, B., Floris, A., De Gironcoli, S. and Cococcioni, M. (2014). Hubbard-corrected DFT energy functionals: The LDA+ U description of correlated systems. **Int. J. Quantum Chem.** 114: 14.

Hohenberg, P. and Kohn, W. (1964). Inhomogeneous electron gas. **Phys. Rev.** 136: B864.

Jo, W. J., Jang, J.-W., Kong, K.-j., Kang, H. J., Kim, J. Y., Jun, H., Parmar, K. P. S. and Lee, J. S. (2012). Phosphate Doping into Monoclinic $BiVO_4$ for Enhanced Photoelectrochemical Water Oxidation Activity. **Angew Chem. Int. Ed.** 51: 3147.

Kittel, C., McEuen, P. and McEuen, P. (1996). **Introduction to solid state physics (Vol. 8)**: Wiley New York.

Kohn, W. and Sham, L. J. (1965). Self-consistent equations including exchange and correlation effects. **Phys. Rev.** 140: A1133.

Kresse, G. and Furthmüller, J. (1996a). Efficiency of Ab-Initio Total Energy Calculations for Metals and Semiconductors using a Plane-Wave Basis Set. **Comput. Mater. Sci.** 6: 15.

Kresse, G. and Furthmüller, J. (1996b). Efficient Iterative Schemes for Ab Initio Total-Energy Calculations using a Plane-Wave Basis Set. **Phys. Rev. B.** 54: 11169.

Kresse, G. and Hafner, J. (1993). Ab Initio Molecular Dynamics for Liquid Metals. **Phys. Rev. B.** 47: 558.

Kresse, G. and Joubert, D. (1999). From Ultrasoft Pseudopotentials to the Projector Augmented-Wave Method. **Phys. Rev. B.** 59: 1758.

Kudo, A., Omori, K. and Kato, H. (1999). A Novel Aqueous Process for Preparation of Crystal Form-Controlled and Highly Crystalline $BiVO_4$ Powder from Layered Vanadates at Room Temperature and Its Photocatalytic and Photophysical Properties. **J. Am. Chem. Soc.** 121: 11459.

Liechtenstein, A., Anisimov, V. and Zaanen, J. (1995). Density-functional theory and strong interactions: Orbital ordering in Mott-Hubbard insulators. **Phys. Rev. B.** 52: R5467.

Liu, G., Liu, S., Lu, Q., Sun, H. and Xiu, Z. (2014). Synthesis and Characterization of $BiVO_4-PO_4$ Nanofibers by Electrospinning Process with Enhanced Photocatalytic Activity under Visible Light. **RSC Adv.** 4: 33695.

Maxisch, T., Zhou, F. and Ceder, G. (2006). Ab Initio Study of the Migration of Small Polarons in Olivine Li_xFePO_4 and Their Association with Lithium Ions and Vacancies. **Phys. Rev. B.** 73: 104301.

Park, H. S., Kweon, K. E., Ye, H., Paek, E., Hwang, G. S. and Bard, A. J. (2011). Factors in the Metal Doping of $BiVO_4$ for Improved Photoelectrocatalytic Activity as Studied by Scanning Electrochemical Microscopy and First-Principles Density-Functional Calculation. **J. Phys. Chem. C.** 115: 17870.

Payne, M. C., Teter, M. P., Allan, D. C., Arias, T. and Joannopoulos, a. J. (1992). Iterative minimization techniques for ab initio total-energy calculations: molecular dynamics and conjugate gradients. **Rev. Mod. Phys.** 64: 1045.

Perdew, J. P., Burke, K. and Ernzerhof, M. (1996). Generalized gradient approximation made simple. **Phys. Rev. Lett.** 77: 3865.

Perdew, J. P., Burke, K. and Ernzerhof, M. (1996). Generalized Gradient Approximation Made Simple. **Phys. Rev. Lett.** 77: 3865.

Rettie, A. J. E., Lee, H. C., Marshall, L. G., Lin, J.-F., Capan, C., Lindemuth, J., McCloy, J. S., Zhou, J., Bard, A. J. and Mullins, C. B. (2013). Combined Charge Carrier Transport and Photoelectrochemical Characterization of $BiVO_4$ Single Crystals: Intrinsic Behavior of a Complex Metal Oxide. **J. Am. Chem. Soc.** 135: 11389.

Slater, J. C. (1930). Note on Hartree's method. **Phys. Rev.** 35: 210.

Sleight, A. W., Chen, H. y., Ferretti, A. and Cox, D. E. (1979). Crystal Growth and Structure of $BiVO_4$. **Mater. Res. Bull.** 14: 1571.

Srepusharawoot, P. (2016). **Computational Materials Science: Basic Theory and Practical Method**.

Tokunaga, S., Kato, H. and Kudo, A. (2001). Selective Preparation of Monoclinic and Tetragonal $BiVO_4$ with Scheelite Structure and Their Photocatalytic Properties. **Chem. Mater.** 13: 4624.

Tolba, S. A., Gameel, K. M., Ali, B. A., Almossalami, H. A. and Allam, N. K. (2018). The DFT+ U: Approaches, Accuracy, and Applications. **Density Functional Calculations: Recent Progresses of Theory and Application.** 16: 1.

Vanderbilt, D. (1990). Soft self-consistent pseudopotentials in a generalized eigenvalue formalism. **Phys. Rev. B.** 41: 7892.

Wärnå, J. (2019). **Water Splitting Mechanism on 2D Catalytic Materials: DFT based Theoretical Investigations**. Acta Universitatis Upsaliensis.

Wu, F. and Ping, Y. (2018). Combining Landau–Zener Theory and Kinetic Monte Carlo Sampling for Small Polaron Mobility of Doped $BiVO_4$ from First-Principles. **J. Mater. Chem. A.** 6: 20025.

Xia, T., Chen, M., Xiao, L., Fan, W., Mao, B., Xu, D., Guan, P., Zhu, J. and Shi, W. (2018). Dip-Coating Synthesis of P-doped $BiVO_4$ Photoanodes with Enhanced Photoelectrochemical Performance. **J. Taiwan Inst. Chem. E.** 93: 582.

CHAPTER III

GEOMETRICAL AND ELECTRONIC STRUCTURES

3.1   Geometrical structure

The *ms*-BiVO$_4$ belongs to the space group *I2/b* with lattice parameters a = 5.1935 Å, b = 5.0898 Å, c = 11.6972 Å, and γ = 90.387° (Sleight *et al.*, 1979). As illustrated in Figure 3.1(a), its unit cell contains four Bi atoms, four V atoms, and sixteen O atoms. Each V atom is coordinated by four O atoms forming a distorted VO$_4$ tetrahedron, each Bi atom is coordinated by eight O atoms forming a distorted BiO$_8$ dodecahedron, and each O atom connects to one V atom and two Bi atoms. The significant distortion in *ms*-BiVO$_4$ caused by Bi 6*s* lone-paired electrons (Payne *et al.*, 2011). The optimized pristine structure exhibits two sets of the average V–O bond distances (1.750, 1.753 Å) and four sets of the average Bi–O bond distances (2.419, 2.431, 2.462, 2.503 Å). These values are consistent with the experimental results (V–O bond distances are 1.69, 1.77 Å and Bi–O bond distances are 2.354, 2.372, 2.516, 2.628 Å) (Sleight *et al.*, 1979), which validates the methodology used in this study.
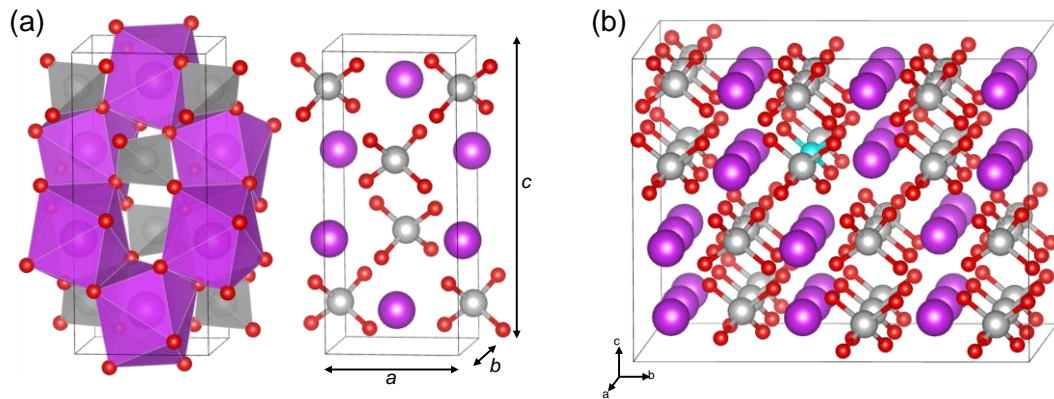
Figure 3.1 (a) Unit cell of *ms*-BiVO$_4$; polyhedron model (left panel) and ball and stick model (right panel) (b) Optimized structure of 3×3×1 P-doped BiVO$_4$ supercell, where purple, gray, red, and blue balls represent Bi, V, O, and P atoms, respectively.

To explore the impact of P-doping toward the local structure of BiVO$_4$, we replaced a V atom with a P atom in the 3×3×1 BiVO$_4$ supercell, as shown in Figure 3.1(b). The substitution of P creates a local structure reorganization at the PO$_4$ unit. As depicted in Figure 3.2 and summarized in Table 3.1, the average P–O bond distance is about 11% shorter than that of the VO$_4$, suggesting a relatively strong interaction between P and the surrounding O atoms in the lattice. There are two sets of P−O bond distances in PO$_4$ tetrahedron which are 1.564 and 1.569 Å. These results are consistent with the previous studies (Jo *et al.*, 2012; Regmi *et al.*, 2019). The relaxation of PO$_4$ tetrahedron in turn leads to the elongation of Bi−O bonds of the nearest BiO$_8$ units. The average distance of these Bi–O bonds in the P–doped system is slightly longer than that of the pristine system by about 4%.
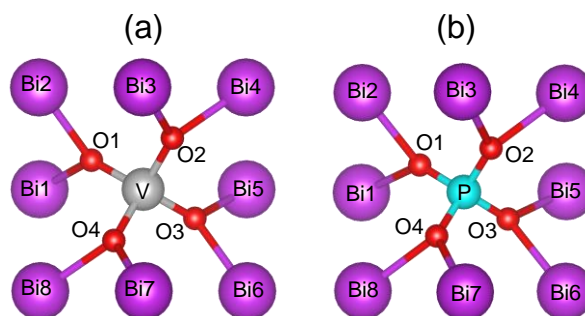
Figure 3.2 Local structures of (a) pristine and (b) P-doped BiVO$_4$.

Table 3.1 Calculated bond distances (Å) of pristine and P-doped BiVO$_4$. Their geometrical structures are shown in Figure 3.2.

Bond distance	Pristine BiVO$_4$	P-doped BiVO$_4$	Variation (%)
V(P)–O1	1.749	1.564	−10.58
V(P)–O2	1.752	1.569	−10.45
V(P)–O3	1.750	1.564	−10.63
V(P)–O4	1.754	1.569	−10.55
			−10.55 ave.
Bi1–O1	2.503	2.655	+6.07
Bi2–O1	2.429	2.489	+2.47
Bi3–O2	2.469	2.592	+4.98
Bi4–O2	2.420	2.480	+2.48
Bi5–O3	2.502	2.655	+6.12
Bi6–O3	2.428	2.494	+2.72
Bi7–O4	2.461	2.589	+5.20
Bi8–O4	2.417	2.483	+2.73
			+4.10 ave.

3.2   Electronic structure

To obtain insight into the electronic structures and bonding property of pristine and P-doped $BiVO_4$, we calculated and analyzed their PDOS. It can be seen from Figure 3.3(a) that pristine $BiVO_4$ exhibits semiconducting character with the calculated band gap of 2.17 eV, which is slightly smaller than the experimental value (2.4 eV) (Kudo *et al.*, 1999; Tokunaga *et al.*, 2001) due to the well-known underestimation of band gap in DFT (Stampfl and Van de Walle, 1999). The VB primarily comprises O 2*p* states with a small contribution from Bi 6*s* states at the VBM. The CB mainly consists of V 3*d* states with some hybridization of O 2*p* states. The distorted VO_4 tetrahedra induces crystal field splitting of d_{z^2}, $d_{x^2-y^2}$, and other *e* states, as discussed in previous computational works (Kweon *et al.*, 2015). It can be seen from Figure 3.3(b) that P doping does not significantly affect the electronic structure of the material as their calculated electronic structures exhibit similar band gap and DOS features. The increased DOS due to the doping at the top of the valence band (–0.7 eV) is insignificant (0.1%). This is expected because P substitution at the V site is considered a homovalent doping where there is no extra charge generated upon doping. Our finding is somewhat different with the previous studies that the band gap is enlarged upon P doping (Jo *et al.*, 2012; Regmi *et al.*, 2019). Such disagreement may stem from the low doping concentration (2.8%) in our model study.
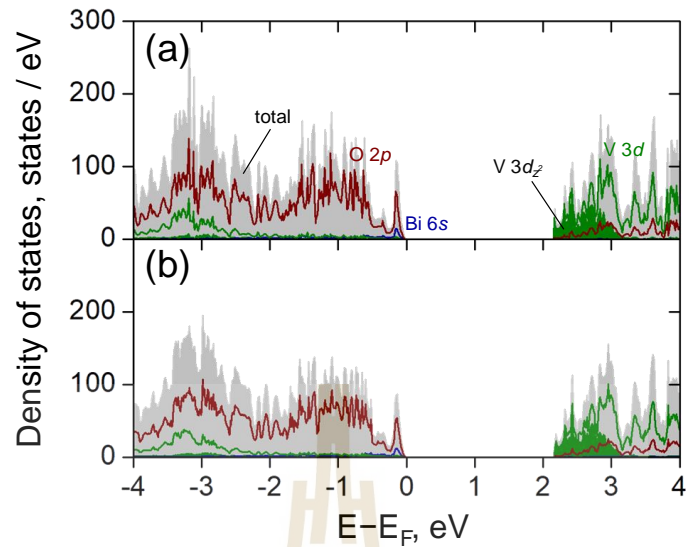
Figure 3.3 PDOS of (a) pristine and (b) P-doped BiVO₄, where royal blue, olive, and wine lines illustrate states contributed by Bi 6*s*, V 3*d*, and O 2*p* states, respectively, total DOS and V d_{z^2} states are shaded in gray and olive, respectively.

The change of charge distribution occurred due to the introduction of P impurities was examined by carrying out the Bader charge analysis. As summarized in Table 3.2, the amount of charge transfer from P atom to neighboring O atoms is larger than that from V atom to O atoms in pristine BiVO₄. In case of pristine system, V atom has 2.843 electrons and the four O atoms in VO₄ have 7.047, 7.048, 7.050, and 7.053 electrons. In case of P-doped system, P atom has 1.378 electrons and the charge of each O atom in PO₄ is very similar, where one O atom has 7.435 electrons and the others have the same number of electrons (7.433). Our calculated values are quantitatively different from those reported in the other DFT studies (Jo *et al.*, 2012; Regmi *et al.*, 2019) that the charge of O atoms in PO₄ fluctuate between 7.406 and 7.453 electrons (Jo *et al.*, 2012) where more charge is accumulated in one pair than that in the other pair of O atoms in PO₄ (Regmi *et al.*, 2019).

Table 3.2 Charge transfer, C_T (e) in pristine and P-doped $BiVO_4$.

C_T	Pristine $BiVO_4$	P-doped $BiVO_4$
V(P)	2.843	1.378
O1	7.047	7.435
O2	7.048	7.433
O3	7.050	7.433
O4	7.053	7.433

Next, we examined the behavior of polaron formation in the pristine and doped systems. We added an extra electron in the supercell where charge neutrality of the system is ensured by a compensating homogeneous background charge. Small perturbation to the V–O bonds of a VO_4 unit was made to break the lattice symmetry and allow for electron localization at the V center. The calculated PDOS shows that the added electron in the pristine and doped system occupies the low-lying energy state of V d_{z^2} and form a deep localized state at 1.03 eV below the conduction band, Figure 3.4. Upon the electron localization, the V center is reduced from V^{5+} to V^{4+} which in turn induces elongation of V–O bonds of the reduced VO_4 unit by 8 pm leading to a formation of a small polaron. It can be seen that the formation of a small polaron in both pristine and doped systems occurs in the same way as evidenced by their electronic trapped states and local distortions.
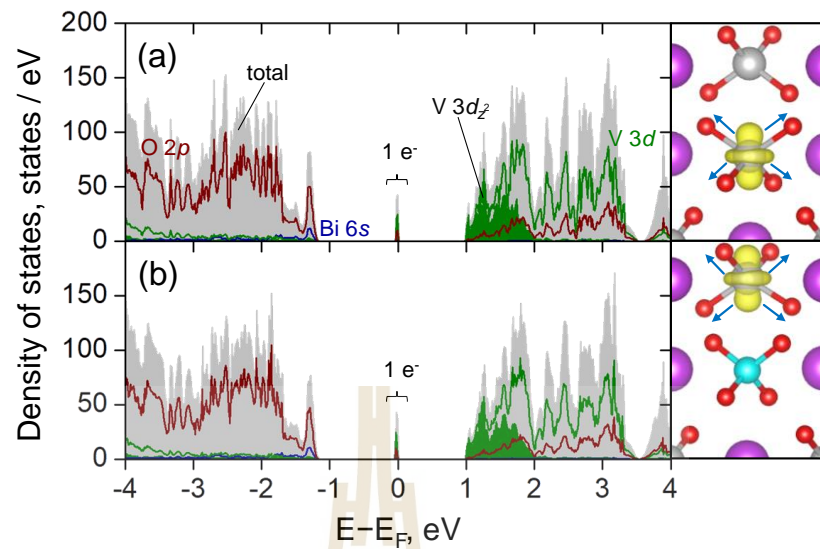
Figure 3.4 PDOS of electron-doped (a) $BiVO_4$ and (b) P-doped $BiVO_4$, where royal blue, olive, and wine lines illustrate states contributed by Bi $6s$, V $3d$, and O $2p$ states, respectively, total DOS and V $3d_{z^2}$ states are shaded in gray and olive, respectively. Spin density of the polaronic state (with an isosurface value of 0.02 e $Å^{-3}$) of pristine and P-doped systems are shown in upper and lower right panel, respectively. Purple, gray, red, and blue balls represent Bi, V, O, and P atoms, respectively, and the blue arrows indicate elongation of the V^{4+}–O bonds. Some Bi atoms and some of the VO_4 tetrahedra are omitted for clarity.

3.3   References

Jo, W. J., Jang, J.-W., Kong, K.-j., Kang, H. J., Kim, J. Y., Jun, H., Parmar, K. P. S. and Lee, J. S. (2012). Phosphate Doping into Monoclinic BiVO$_4$ for Enhanced Photoelectrochemical Water Oxidation Activity. **Angew Chem. Int. Ed.** 51: 3147.

Kudo, A., Omori, K. and Kato, H. (1999). A Novel Aqueous Process for Preparation of Crystal Form-Controlled and Highly Crystalline BiVO$_4$ Powder from Layered Vanadates at Room Temperature and Its Photocatalytic and Photophysical Properties. **J. Am. Chem. Soc.** 121: 11459.

Kweon, K. E., Hwang, G. S., Kim, J., Kim, S. and Kim, S. (2015). Electron Small Polarons and Their Transport in Bismuth Vanadate: a First Principles Study. **Phys. Chem. Chem. Phys.** 17: 256.

Payne, D. J., Robinson, M. D. M., Egdell, R. G., Walsh, A., McNulty, J., Smith, K. E. and Piper, L. F. J. (2011). The Nature of Electron Lone Pairs in BiVO$_4$. **Appl. Phys. Lett.** 98: 212110.

Regmi, C., Kshetri, Y. K., Dhakal, D., Sohng, J. K., Rosei, F. and Lee, S. W. (2019). Insight into Phosphate Doped BiVO$_4$ Heterostructure for Multifunctional Photocatalytic Performances: A Combined Experimental and DFT Study. **Appl. Surf. Sci.** 466: 787.

Sleight, A. W., Chen, H. y., Ferretti, A. and Cox, D. E. (1979). Crystal Growth and Structure of BiVO$_4$. **Mater. Res. Bull.** 14: 1571.

Stampfl, C. and Van de Walle, C. G. (1999). Density-Functional Calculations for III-V Nitrides using the Local-Density Approximation and the Generalized Gradient Approximation. **Phys. Rev. B.** 59: 5521.

Tokunaga, S., Kato, H. and Kudo, A. (2001). Selective Preparation of Monoclinic and Tetragonal BiVO$_4$ with Scheelite Structure and Their Photocatalytic Properties. **Chem. Mater.** 13: 4624.
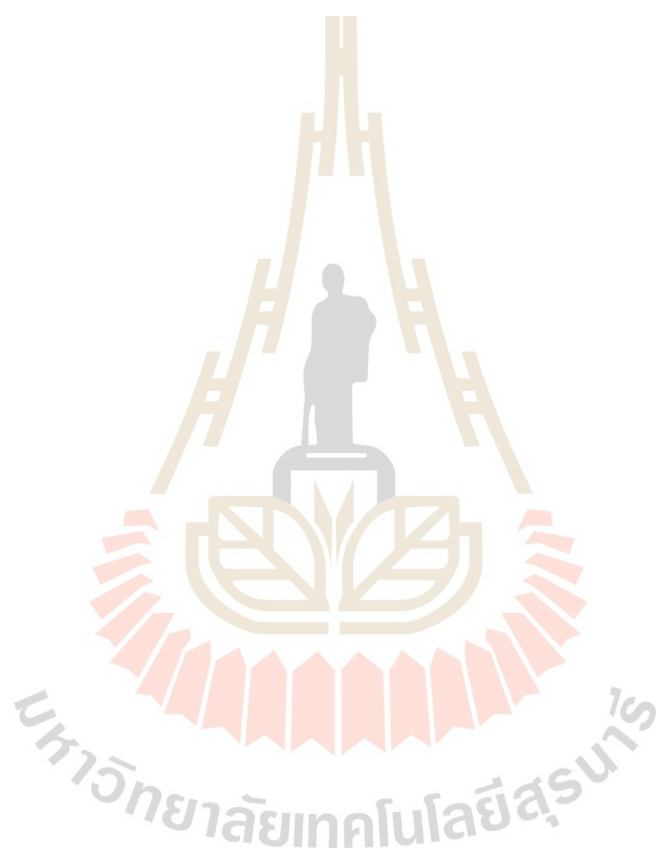
CHAPTER IV

FORMATION OF OXYGEN VACANCY AND

ITS STABILITY

Among various point defects, oxygen vacancies (V_O) are known as potential n-type dopants to improve charge carrier concentrations in various TMOs including BiVO$_4$ (Cooper *et al.*, 2016; Kim *et al.*, 2015; Seo *et al.*, 2018; Ullah *et al.*, 2018; Xia *et al.*, 2018; Yin *et al.*, 2011). Creation of an V_O gives rise to two electron carriers which have been regarded as an origin of the intrinsic n-type conductivity. The concentration of V_O in the lattice plays an important role in determining electrical conductivity of the materials. Therefore, the formation and relative stability of V_O in the pristine and doped systems were investigated to understand the effect of P doping on the improved current density of the photoanode.

4.1　Formation of oxygen vacancy

We removed an O atom in a selected VO$_4$ unit and PO$_4$ unit to generate an V_O in the pristine and P-doped BiVO$_4$ supercell, respectively. Various charge states of the V_O systems were considered including the doubly positive V_O (V_0^{2+}), the ionized V_O with a single polaron (V_0^{2+}-η^-), and that with two polarons (V_0^{2+}-$2\eta^-$). These charged systems can be obtained by manually adjusting the number of electrons in the supercell where a compensating homogeneous background charge was imposed to ensure charge neutrality of the systems. Their ionic coordinates were relaxed to yield

the V_O structures corresponding with the assigned charge state. In what follows, we explained how to obtain the V_O structures with various charge states where the changes in atomistic and electronic structures are schematically illustrated in Figure 4.1. Calculated bond lengths of key polyhedra are summarized in Table 4.1 and Table 4.2.
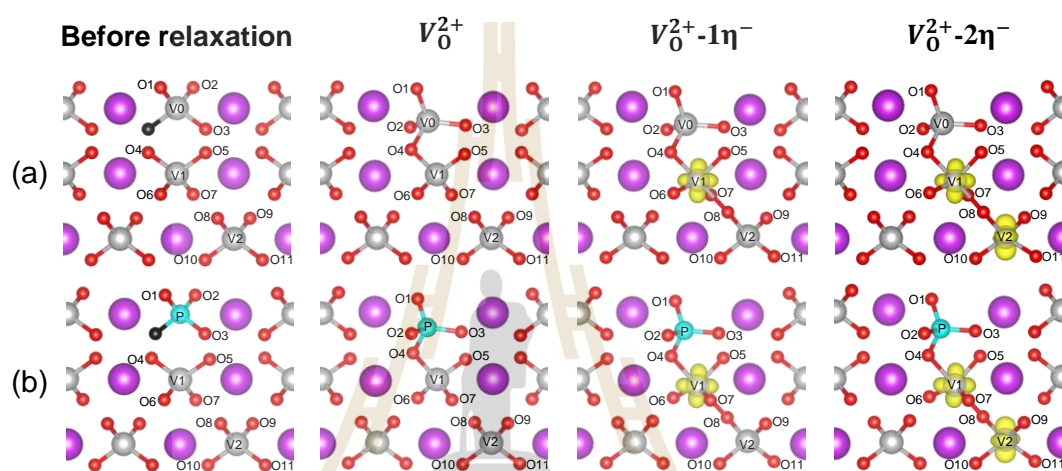
Figure 4.1 Geometry of V_O structure of (a) pristine and (b) P-doped $BiVO_4$ with various charge states including the doubly positive V_O (V_O^{2+}), the ionized V_O with a single polaron (V_O^{2+}-$1\eta^-$), and that with two polarons (V_O^{2+}-$2\eta^-$). The yellow isosurface with the value of 0.02 e $Å^{-3}$ indicates the spin density of the polaronic state. Purple, gray, red, and blue balls represent Bi, V, O, P atoms, respectively. Black balls represent the removed O atoms. Some Bi atoms and some of the VO_4 tetrahedra are omitted for clarity.

Table 4.1 Calculated bond distances (Å) and the variation of bond distances (numbers in parentheses) of pristine system. Their geometrical structures are shown in Figure 4.1(a).

Bond distances	Before relaxation	V_O^{2+}	$V_O^{2+}\text{-}1\eta^-$	$V_O^{2+}\text{-}2\eta^-$
V0–O1	1.752	1.710 (–0.042)	1.724 (+0.014)	1.723 (–0.001)
V0–O2	1.754	1.706 (–0.048)	1.727 (+0.021)	1.734 (+0.007)
V0–O3	1.749	1.718 (–0.031)	1.737 (+0.019)	1.736 (–0.001)
V0–O4	2.985	1.836 (–1.149)	1.781 (–0.055)	1.776 (–0.005)
V1–O4	1.750	1.853 (+0.103)	2.018 (+0.165)	2.051 (+0.033)
V1–O5	1.750	1.711 (–0.039)	1.837 (+0.126)	1.838 (+0.001)
V1–O6	1.752	1.720 (–0.032)	1.798 (+0.078)	1.802 (+0.004)
V1–O7	1.752	1.727 (–0.025)	1.784 (+0.057)	1.788 (+0.004)
V1–O8	3.015	2.874 (–0.141)	2.196 (–0.678)	2.129 (–0.067)
V2–O8	1.752	1.749 (–0.003)	1.798 (+0.049)	1.875 (+0.077)
V2–O9	1.752	1.759 (+0.007)	1.749 (–0.010)	1.839 (+0.090)
V2–O10	1.750	1.754 (+0.004)	1.747 (–0.007)	1.816 (+0.069)
V2–O11	1.750	1.745 (–0.005)	1.720 (–0.025)	1.810 (+0.090)

Table 4.2 Calculated bond distances (Å) and the variation of bond distances (numbers in parentheses) of P-doped system. Their geometrical structures are shown in Figure 4.1(b).

Bond distances	Before relaxation	V_O^{2+}	V_O^{2+}-$1\eta^-$	V_O^{2+}-$2\eta^-$
P–O1	1.564	1.536 (–0.028)	1.545 (+0.009)	1.546 (+0.001)
P–O2	1.569	1.530 (–0.039)	1.544 (+0.014)	1.546 (+0.002)
P–O3	1.569	1.535 (–0.034)	1.547 (+0.012)	1.547 (0.000)
P–O4	3.081	1.646 (–1.435)	1.605 (–0.041)	1.602 (–0.003)
V1–O4	1.751	1.878 (+0.127)	2.041 (+0.163)	2.058 (+0.017)
V1–O5	1.752	1.711 (–0.041)	1.837 (+0.126)	1.837 (0.000)
V1–O6	1.752	1.713 (–0.039)	1.808 (+0.095)	1.808 (0.000)
V1–O7	1.748	1.723 (–0.025)	1.783 (+0.060)	1.790 (+0.007)
V1–O8	2.986	2.855 (–0.131)	2.183 (–0.672)	2.133 (–0.050)
V2–O8	1.747	1.748 (+0.001)	1.796 (+0.048)	1.861 (+0.065)
V2–O9	1.751	1.756 (+0.005)	1.745 (–0.011)	1.823 (+0.078)
V2–O10	1.756	1.759 (+0.003)	1.753 (–0.006)	1.834 (+0.081)
V2–O11	1.749	1.745 (–0.004)	1.721 (–0.024)	1.823 (+0.102)

First, we optimized the doubly positive charge state (V_O^{2+}) systems. The V_O^{2+} state can be obtained by removing two electrons from the systems containing one V_O. For the pristine structure, the relaxed coordinates reveal that the VO_3 unit (denoted as V0) moves towards a neighboring VO_4 unit (denoted as V1) and share one O atom with it, as depicted in Figure 4.1(a). The newly formed V0–O bond is considerably longer than those of the equilibrium V–O bonds in the pristine structure (1.84 Å *vs* 1.75 Å), as summarized in Table 4.1. The structural reorganization in turn increases the bond distance between V1 and the shared O atom by 10 pm whereas the other three V1–O bonds are shortened by 2 to 4 pm, as presented in Table 4.1. Next, we put one electron back into the optimized V_O^{2+} system to generate the V_O^{2+}-η^- system. Due to the elongation of V1–O bond upon the removal of the O atom, the added electron prefers to localize at the V1 center and forms a small polaron as indicated by the isosurface plot of its spin density, Figure 4.1(a). Local structure distortion occurs upon the polaron formation. The $V1O_4$ unit relaxes closer to the nearby VO_4 unit (denoted as V2) and share one O atom to form the $V1O_5$ distorted trigonal bipyramid with a rather long apical V1–O bond of 220 pm, as detailed in Table 4.1. Finally, the second electron was added to the V_O^{2+}-η^- system to neutralize the V_O^{2+} charge and yield the V_O^{2+}-$2\eta^-$ system. As expected, the added electron localizes and forms a polaron at the V2 center leading to elongations of $V2O_4$ bonds in the range of 7 to 9 pm.

Likewise, the P-doped system exhibits similar behavior of polaron formation. Two electron polarons were generated upon the removal of an O atom at the PO_4 unit. These polarons localize at the two nearest V centers (V1, V2) and create local structure distortions at the polaronic sites, Figure 4.1(b) and Table 4.2. Nevertheless, a

distinct different from the pristine system is noted that the PO_4 bonds are significantly shorter than those of the VO_4 bonds. As a result, once the V_O was introduced at the PO_4 unit, the undercoordinated PO_3 unit relaxes closer to the V1 center to form the P–O bond with the shared O atom. The relaxed structure leads to a longer V1–O bond which offers a preferred site for a polaron formation resulting in a relatively low polaron formation energy compared to that of the pristine system (60 meV more stable). The effect of P impurity toward the stability of polaron is exclusive at the nearest neighbor V1 center. The second polaron formation at the V2 center is not affected where their relative formation energies are very similar (energy difference is less than 1 meV).

To ensure that the obtained polaron configurations are most stable, we calculated relative energies of several polaron configurations where the two polarons are localized at different V centers throughout the lattice, as depicted in Figure 4.2. For both pristine and doped systems, the most stable configurations are indeed the ones we initially obtained where the two polarons are located at the V1 and V2 centers, configuration C1. The other configurations where one or both polarons are not at the V1 and V2 sites are less stable, Figure 4.3. One example of the unstable configurations is when two electrons localize at the same V1 center, C2, they exhibit higher energies by 111 and 136 meV for the pristine and P-doped systems, respectively (Figure 4.3). It is not surprising that the least stable configurations for both systems have two polarons far away from the V_O site, configuration C3. Nevertheless, in the case that one polaron is at the V1 center and the other polaron is not in the vicinity of the defect site, C4, the polaronic stabilities are comparable to that of the most stable configuration. The calculated results indicate that an V_O

generates two electron polarons at the two nearest V centers where one polaron is tightly bound to the defect site at the V1 center where the other polaron is relatively mobile.
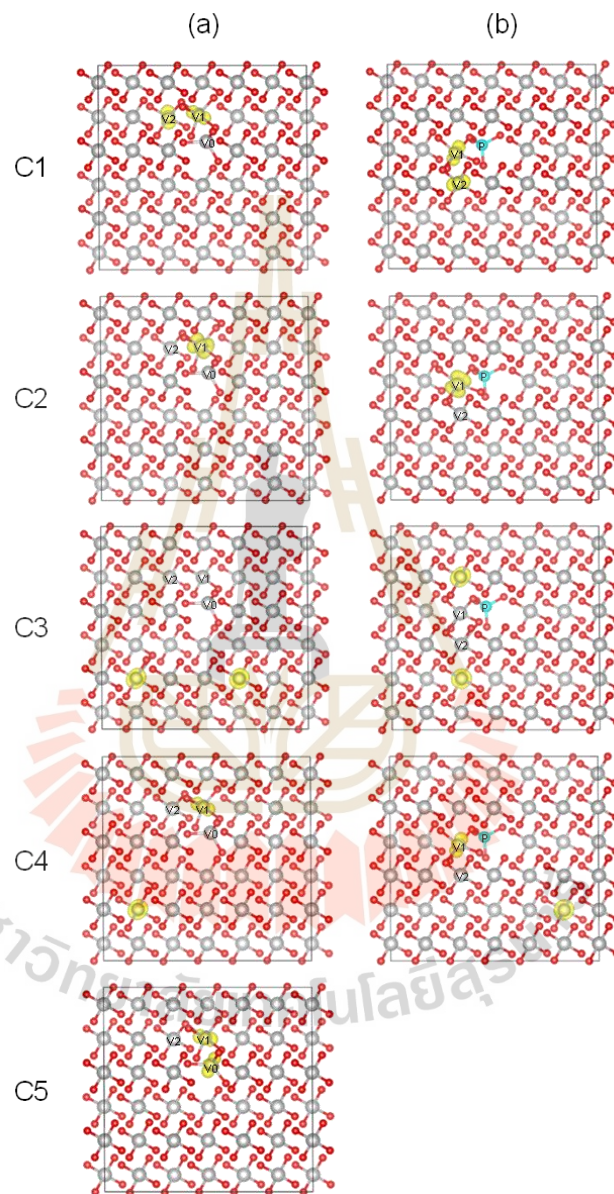
Figure 4.2 Several configurations of small polaron localization in the V_O structure of (a) pristine and (b) P-doped BiVO$_4$. Yellow isosurface with the value of 0.02 e Å^{-3} indicates the spin density of the polaronic state. Gray, red, and blue balls represent V, O, and P atoms, respectively. Bi atoms are omitted for clarity.
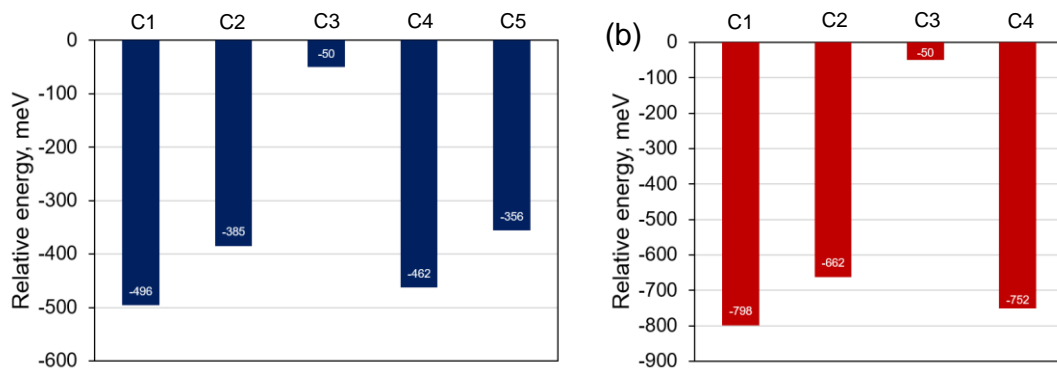
Figure 4.3 Corresponding relative energies of several configurations of small polaron localization for (a) pristine and (b) P-doped systems.

4.2 Stability of oxygen vacancy

We determined relative stabilities of V_O in the pristine and P-doped systems to better understand the role of P doping on the improved photocatalytic activity. To obtain a complete situation of all V_O charge states and their corresponding ionization energies, we calculated and analyzed the defect formation energies as a function of Fermi energy. This method has been widely used to describe the stabilities of various defects in several semiconducting materials including BiVO$_4$ (Seo *et al.*, 2018; Wang *et al.*, 2013; Yin *et al.*, 2011). In addition, stability of P impurity and its V_O complex were calculated to explain the origin of the improved reducibility and charge carrier concentrations. The defect formation energies, E^f for any point defect, X^q in charge state, q were calculated using the following expression (Freysoldt *et al.*, 2014; Zhang and Northrup, 1991)

$$E^f(X^q) = E_{\text{tot}}(X^q) - E_{\text{tot}}(\text{bulk}) - \sum_i \Delta n_i \mu_i + q(E_{\text{VBM}} + E_{\text{F}}) + E_{\text{corr}}^q, \quad (4.1)$$

where $E_{\text{tot}}(X^q)$ is the total energy of the defective supercell containing point defect, X^q in charge state, q and $E_{\text{tot}}(\text{bulk})$ is the total energy of the pristine supercell. For each elemental specie, i^{th}, μ_i and Δn_i represent the chemical potential and the number

of added (or removed) atoms in the defective supercell of the element. The chemical potential of each species was calculated by taking into account the thermodynamics of growth conditions. In addition, the chemical potential of electron or Fermi energy, E_F is considered, where its value is referenced at energy of VBM, E_{VBM}. Defect formation energies are plotted as a function of Fermi level from zero to the band gap energy, E_g. The last term E_{corr}^q is responsible for correction of an artifact contributed by interactions between charged defect and its periodic images. In this thesis, we use image-charge correction method proposed by Freysoldt, Neugebauer, and Van de Walle as implemented in sxdefectalign code (Freysoldt *et al.*, 2009, 2011; Kumagai and Oba, 2014).

In general, chemical potentials depend upon the experimental growth conditions (Freysoldt *et al.*, 2014). The changes in chemical potential related to growth condition would generate different defect formations or materials. However, the variable range of chemical potential is limited by thermodynamics. For instance, the chemical potential of Bi, V, and O are linked by the formation energy of primary phase BiVO$_4$

$$\Delta\mu_{Bi} + \Delta\mu_V + 4\Delta\mu_O = \Delta H^f(\text{BiVO}_4), \tag{4.2}$$

while the elementary chemical potentials are referenced by their standard phases by the following equations

$$\Delta\mu_O = \mu_O - \frac{1}{2}E_{tot}(O_2),$$

$$\Delta\mu_{Bi} = \mu_{Bi} - E_{tot}(Bi_{metal}), \text{ and}$$

$$\Delta\mu_V = \mu_V - E_{tot}(V_{metal}). \tag{4.3}$$

In addition, they must be satisfied the set of constraints for preventing the formations of other secondary Bi-V-O phases including *(i)* elements, e.g. Bi-metal, V-metal, and O_2-gas *(ii)* other competing metal oxides, e.g. bismuth oxides and vanadium oxides

   (i) For elements: $\mu_{Bi} \leq 0$, $\mu_V \leq 0$, and $\mu_O \leq 0$

   (ii) For competing phases: $m\mu_V + n\mu_O \leq \Delta H^f(V_mO_n)$ and $m\mu_{Bi} + n\mu_O \leq \Delta H^f(Bi_mO_n)$.

For P impurities, the chemical potential $\Delta\mu_P = \mu_P - E_{tot}(P)$ can be defined as the minimum number between $\frac{1}{2}(\Delta H^f(P_2O_5) - 5\Delta\mu_O)$ and $\Delta H^f(VPO_5) - \Delta\mu_V - 4\Delta\mu_O$ to represent the P-rich limit.

   Figure 4.4 (green region) illustrates the satisfied chemical potential domain in 2D when $\Delta\mu_{Bi}$ and $\Delta\mu_V$ are projected onto x and y axes respectively, whereas $\Delta\mu_O$ is associated with others by Equation (4.3). As a result, the equilibrium phase boundaries are O_2, Bi, V_2O_5, VO_2, and Bi_2O_3. The points at boundaries A and B represent two extreme conditions, i.e. A (O-poor/V-rich) and B (O-rich/V-poor). The chemical potentials $\Delta\mu_{Bi}$, $\Delta\mu_V$, $\Delta\mu_O$, and $\Delta\mu_P$ at condition A (condition B) are 0.00, –0.33, –2.23, and –2.82 eV (–3.09, –6.17, 0.00 and –6.91 eV), respectively. This potential domain qualitatively agrees well with previous calculations (Wang *et al.*, 2013; Yin *et al.*, 2011) which the quantitative differences comes from Hubbard parameter U for V 3*d*. In this thesis, we mainly focused on condition A which is associated with oxygen vacancy due to the O deficiency, namely, n-type doping (Lamers *et al.*, 2018).
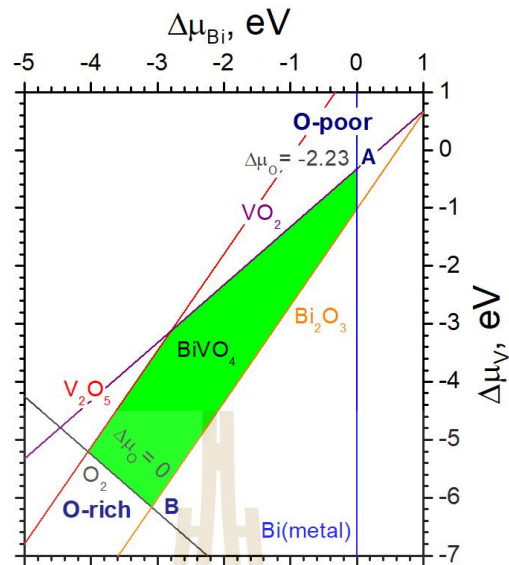
Figure 4.4 Projection of the chemical potential domain ($\Delta\mu_{Bi}$, $\Delta\mu_V$, and $\Delta\mu_O$) that satisfy the thermodynamic formation of BiVO$_4$ (green region) and constraints of secondary phases.

As shown in Figure 4.5, the calculated formation energies of various defects were plotted as a function of Fermi energy from the VBM to the CBM. The calculated band gap of 2.17 eV is shown in the black dotted line whereas the experimental band gap is 2.4 eV (Kudo *et al.*, 1999; Tokunaga *et al.*, 2001). The slope of each line indicates the charge of the defect. It can be seen that an injected electron polaron is stable with a charge state of –1 at 0.19 eV below the CBM (purple dashed line). Such calculated value is rather different with the result obtained by PBE+U (0.38 eV) in the previous computational work where they used the tetragonal BiVO$_4$ to be the model study (Seo *et al.*, 2018).
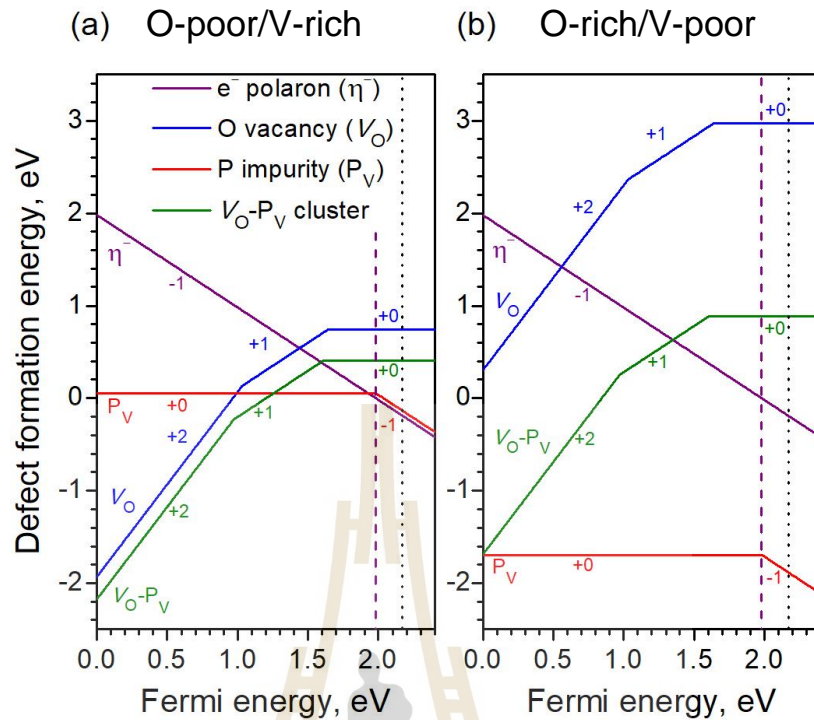
Figure 4.5 Defect formation energy of various defects in $BiVO_4$ as a function of Fermi energy for a) O-poor/V-rich and b) O-rich/V-poor conditions. The formation energies of isolated electron polaron (η^-), oxygen vacancy (V_O), phosphorus substitution for vanadium (P_V) and defect complex of V_O and phosphorus impurity (V_O-P_V) are represented by purple, blue, red, and green lines, respectively. The purple dashed line and black dotted line indicate the polaron level of 1.98 eV and the CBM level of 2.17 eV, respectively.

Stabilities of an V_O in the pristine and doped systems are of central interest. As previously discussed, the native V_O is in a doubly positive charged state where two electron polarons are formed at the two nearby V centers to neutralize the positive charges such that, $V_O^{2+} + \eta^- \rightleftharpoons [V_O^{2+}\text{-}\eta^-]$ and $[V_O^{2+}\text{-}\eta^-] + \eta^- \rightleftharpoons [V_O^{2+}\text{-}2\eta^-]$. Computations reveal that an V_O is stable in three possible charged states of +2, +1, and 0 within the band gap. The charge transition levels (CTLs) from +2 to +1 (+2/+1)

and +1 to 0 (+1/0) are determined at 1.14 and 0.53 eV below the CBM, respectively. The calculated results are consistent with the previously reported value for (+1/0) at 0.59 eV below the CBM (Seo *et al.*, 2018). Such a deep CTL of (+1/0) indicates that the energy needed to ionize the trapped electrons to the conduction band to generate free electrons is quite large (0.53 eV) with respect to thermal energy at room temperature (0.026 eV). As a result, the electrons are likely to be trapped at the local distortion as small polarons which is consistent with that observed in an experimental work (Cooper *et al.*, 2016). It has been reported that at finite temperature the electronic conductivity in oxygen deficient $BiVO_4$ is contributed by polaron migration rather than that the band conduction (Kumagai and Oba, 2014; Seo *et al.*, 2018).

The energy difference between the calculated CTLs of the V_O with respect to that of the isolated polaron can be used to determine the binding energies of each polaron to the defect site. The binding energy, E_b, is the energy different between formation energy of a complex defect and the sum of formation energies of isolated defects. For example, the binding energy of a complex defect containing X and Y can be calculated by

$$E_b = E^f(X) + E^f(Y) - E^f([X\text{-}Y]). \tag{4.4}$$

The calculated binding energies of the first and second polarons are 0.34 and 0.95 eV, respectively. Their positive values indicate that these polarons are likely to be in proximity with the V_O site. Nevertheless, it is possible that one bound polaron can be thermally activated to migrate to other V centers since its binding energy is relatively low (0.34 eV). On the other hand, the large binding energy of 0.95 eV forbids the second polaron to hop away from the defect site. These results agrees with those

obtained from the total energy calculations that the polaron at the V1 center strongly binds to the V_O site.

P impurities can be introduced into the crystal in three possible defect forms including interstitial phosphorus (P_i), phosphorus substitution for oxygen (P_O), and phosphorus substitution for vanadium (P_V). X-ray diffraction patterns reveal that the foreign P atoms substitute at V lattice sites and form a solid solution (Liu *et al.*, 2014). To confirm, their formation energies were calculated as shown in Figure 4.6.
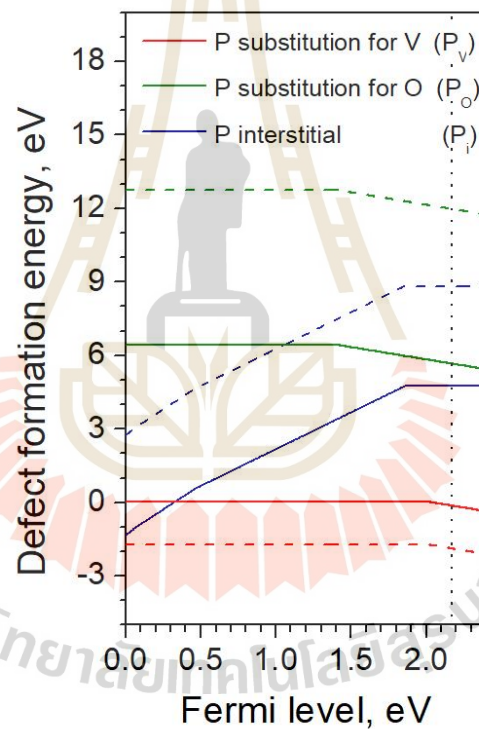
Figure 4.6 Defect formation energy of P impurity point defects in $BiVO_4$ as a function of fermi energy in condition A (O-poor/V-rich) (solid line) and condition B (O-rich/V-poor) (dotted line). The formation energies of phosphorus substitution for vanadium (P_V), phosphorus substitution for oxygen (P_O) and interstitial phosphorus (P_i) are represented by red, green, and blue lines, respectively.

It can be seen from Figure 4.6 that under condition B, defect formation energy of P_V is lowest in entire range of Fermi energy in the band gap. Similarly, defect formation energy of P_V is lowest in a wide range of the band gap under condition A. Even if P_i is more stable when Fermi energy close to VBM, it is not likely to be formed due to the lack of the negatively charged compensators. Thus, P_V is the most stable impurity defect for both O-poor and O-rich conditions because P and V have the same valency where their sizes are also similar ($r_P = 1.00$ Å, $r_V = 1.35$ Å). The P_V point defect is determined as an isovalent doping where there is no charge carrier generated in the system and its charged state is 0 as shown in Figure 4.5.

To study the interaction between an electron polaron and the P_V defect, we induced a polaron formation at the V center adjacent to the PO_4 unit resulting in a defect complex of $[P_V^0\text{-}\eta^-]$ with charge -1 as described by $P_V^0 + \eta^- \rightleftharpoons [P_V^0\text{-}\eta^-]$. The defect complex exhibits the CTL of $(0/-1)$ at 0.19 eV below the CBM which is equivalent to that of the isolated polaron. The calculated polaron binding energy of P_V is only 5 meV suggesting that a polaron tends not to be bound to the P dopant. The calculated results are consistent with the transport behavior that P doping does not affect the polaron hopping barriers where the calculated barriers in both pristine and P-doped systems are very similar (0.30 eV).

Next, we explored the effect of P doping on the stability of V_O. Computations show that P_V acts as an V_O trap where the calculated binding energy of defect complex $[V_O^{2+}\text{-}P_V^0]$ is 0.29 eV. It is suggested that V_O^{2+} prefers to be in the vicinity of the P impurity in the lattice. The $[V_O^{2+}\text{-}P_V^0]$ complex can be neutralized by the presence of two trapped polarons at the two nearest V centers to yield charged state of $+1$ and 0 as $[V_O^{2+}\text{-}P_V^0] + \eta^- \rightleftharpoons [V_O^{2+}\text{-}P_V^0\text{-}\eta^-]$ and $[V_O^{2+}\text{-}P_V^0\text{-}\eta^-] + \eta^- \rightleftharpoons [V_O^{2+}\text{-}P_V^0\text{-}2\eta^-]$. As shown in

Figure 4.5, the formation energy of this defect complex exhibits CTLs of (+2/+1) and (+1/+0) at 1.20 and 0.57 eV below the CBM, respectively, indicating deep donor states upon the V_O formation. The calculated polaron binding energies of 0.38 and 1.01 eV for the two polarons are quite similar to the case of isolated V_O which reflects that the defect complex could trap one polaron whereas the other polaron is relatively mobile.

Although isolated V_O and PO_4-V_O cluster exhibit similar behavior of polaron formation, the defect formation energy of the cluster is 0.3 eV lower for the charged states of +1 and 0 in the O-poor condition. Especially, in the O-rich environment, the stabilities of V_O are dramatically improved (2.1 eV) in the presence of P doping atom. The calculated results imply that P doping can stabilize V_O structures by forming a defect complex leading to higher concentrations of V_O. We can roughly estimate the relative concentration of V_O, $N(T)$ between the pristine and doped systems using the following expression

$$N(T) = N_0 \exp\left(\frac{-E^f}{k_B T}\right), \tag{4.5}$$

where N_0 is total number of possible defect sites per unit volume in the crystal, k_B is the Boltzmann's constant, and E^f is the defect formation energy. At the doping concentration of 1% and room temperature, the estimated concentration of V_O of the doped system is approximately five orders of magnitude greater than that of the pristine system. The calculated results are in agreement with that observed in the XPS measurement that the concentration of V_O is improved upon P doping (Xia *et al.*, 2018). Hence, P doping improves reducibility which increases number of charge carriers in the $BiVO_4$ photoanode.

4.3 References

Cooper, J. K., Scott, S. B., Ling, Y., Yang, J., Hao, S., Li, Y., Toma, F. M., Stutzmann, M., Lakshmi, K. V. and Sharp, I. D. (2016). Role of Hydrogen in Defining the n-Type Character of $BiVO_4$ Photoanodes. **Chem. Mater.** 28: 5761.

Freysoldt, C., Grabowski, B., Hickel, T., Neugebauer, J., Kresse, G., Janotti, A. and Van de Walle, C. G. (2014). First-principles Calculations for Point Defects in Solids. **Rev. Mod. Phys.** 86: 253.

Freysoldt, C., Neugebauer, J. and Van de Walle, C. G. (2009). Fully Ab Initio Finite-Size Corrections for Charged-Defect Supercell Calculations. **Phys. Rev. Lett.** 102: 016402.

Freysoldt, C., Neugebauer, J. and Van de Walle, C. G. (2011). Electrostatic Interactions between Charged Defects in Supercells. **Phys. Status Solidi B.** 248: 1067.

Kim, T. W., Ping, Y., Galli, G. A. and Choi, K.-S. (2015). Simultaneous Enhancements in Poton Absorption and Charge Transport of Bismuth Vanadate Photoanodes for Solar Water Splitting. **Nat. Comm.** 6: 8769.

Kudo, A., Omori, K. and Kato, H. (1999). A Novel Aqueous Process for Preparation of Crystal Form-Controlled and Highly Crystalline $BiVO_4$ Powder from Layered Vanadates at Room Temperature and Its Photocatalytic and Photophysical Properties. **J. Am. Chem. Soc.** 121: 11459.

Kumagai, Y. and Oba, F. (2014). Electrostatics-Based Finite-Size Corrections for First-Principles Point Defect Calculations. **Phys. Rev. B.** 89: 195205.

Lamers, M., Fiechter, S., Friedrich, D., Abdi, F. F. and van de Krol, R. (2018). Formation and Suppression of Defects during Heat Treatment of BiVO$_4$ Photoanodes for Solar Water Splitting. **J. Mater. Chem. A.** 6: 18694.

Liu, G., Liu, S., Lu, Q., Sun, H. and Xiu, Z. (2014). Synthesis and Characterization of BiVO$_4$−PO$_4$ Nanofibers by Electrospinning Process with Enhanced Photocatalytic Activity under Visible Light. **RSC Adv.** 4: 33695.

Seo, H., Ping, Y. and Galli, G. (2018). Role of Point Defects in Enhancing the Conductivity of BiVO$_4$. **Chem. Mater.** 30: 7793.

Tokunaga, S., Kato, H. and Kudo, A. (2001). Selective Preparation of Monoclinic and Tetragonal BiVO$_4$ with Scheelite Structure and Their Photocatalytic Properties. **Chem. Mater.** 13: 4624.

Ullah, H., Tahir, A. A. and Mallick, T. K. (2018). Structural and Electronic Properties of Oxygen Defective and Se-Doped p-Type BiVO$_4$ (001) Thin Film for the Applications of Photocatalysis. **Appl. Catal. B.** 224: 895.

Wang, G., Ling, Y., Lu, X., Qian, F., Tong, Y., Zhang, J. Z., Lordi, V., Rocha Leao, C. and Li, Y. (2013). Computational and Photoelectrochemical Study of Hydrogenated Bismuth Vanadate. **J. Phys. Chem. C.** 117: 10957.

Xia, T., Chen, M., Xiao, L., Fan, W., Mao, B., Xu, D., Guan, P., Zhu, J. and Shi, W. (2018). Dip-Coating Synthesis of P-doped BiVO$_4$ Photoanodes with Enhanced Photoelectrochemical Performance. **J. Taiwan Inst. Chem. E.**

Yin, W.-J., Wei, S.-H., Al-Jassim, M. M., Turner, J. and Yan, Y. (2011). Doping Properties of Monoclinic BiVO$_4$ Studied by First-Principles Density-Functional Theory. **Phys. Rev. B.** 83: 155102.

Zhang, S. B. and Northrup, J. E. (1991). Chemical Potential Dependence of Defect Formation Energies in GaAs: Application to Ga Self-Diffusion. **Phys. Rev. Lett.** 67: 2339.
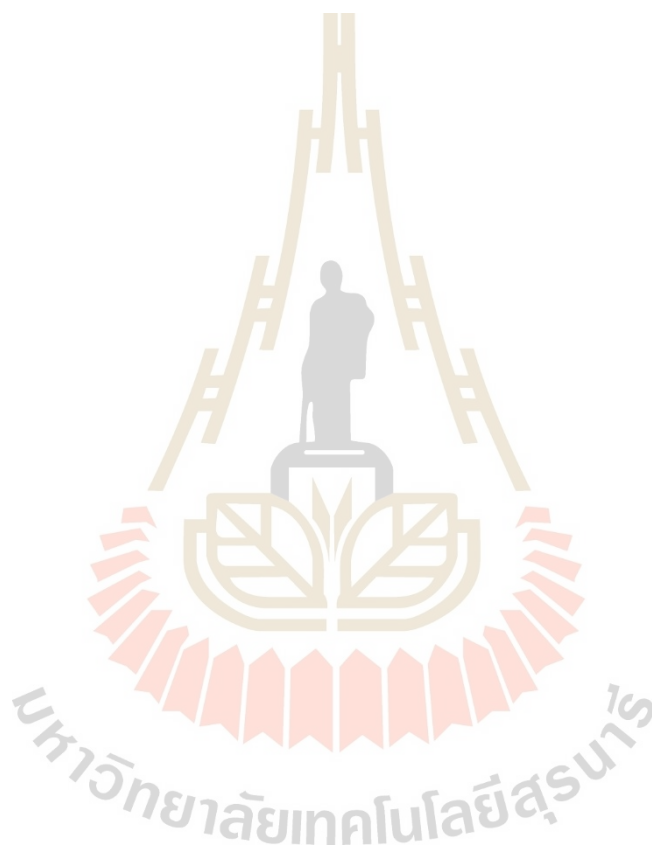
CHAPTER V

BEHAVIOR OF CHARGE TRANSPORT

As discussed in the previous chapter, the role of P doping toward the improved photocatalytic activities could be described by its potential to stabilize oxygen vacancy (V_O) which in turn increases number of charge carriers in the materials. The character of the generated electron polarons is of particular interest. It is known that a polaron can undergo thermally activated hopping from one polaronic site to the nearby site throughout the lattice. In this chapter, we first presented the electronic transport in the polaron hopping model and then we investigated the behavior of polaron transport and their mobilities by computing their migration barriers for pristine and P-doped systems with and without V_O.

5.1   Polaron hopping model

A schematic illustration of the electronic structure of the states involved in a basic polaron transfer process is shown in Figure 5.1. There are three relevant states in this process. The initial state is shown with the equilibrium configuration q_A where the extra electron polaron is localized on one V site, while the final state is shown with the equilibrium configuration q_B where the electron polaron has moved to an adjacent V site. In our case, the initial and final states are V^{4+}-V^{5+} and V^{5+}-V^{4+}, respectively. The transition state (TS) between these two states is shown as q_C. The

significant aspect in this process (see Figure 5.1) is the lattice deformation along the polaron hopping path, involving the change of bond lengths. A larger shading area is assigned to the V atom holding the extra electron and longer bonds are shown between the V atom and the O atoms bound to it. A linearized mathematical model of this polaronic distortion are used as a definition of the polaron transfer coordinate (N Aaron Deskins and Dupuis, 2007).
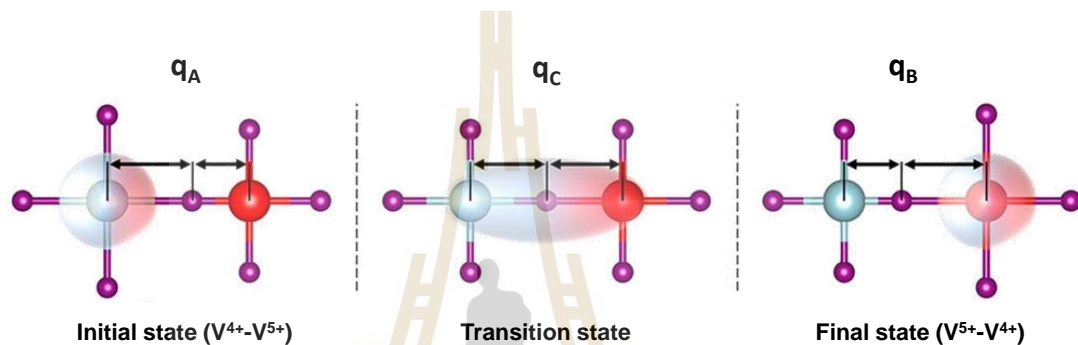
Figure 5.1 Schematic diagram of electron polaron transfer. Larger and smaller atoms represent V and O atoms, respectively. In the initial state with configuration q_A, the electron is localized on the left V atom, while in the final state with configuration q_B, the electron is localized on the right V atom. At the transition state with configuration q_C, (thermal transfer regime), the electron is shared between the two V atoms (Natanzon *et al.*, 2020).

The polaron transfer process can be described by the Marcus-Emin-Holstein-Austin-Mott theories. Within these theories, there are three important parameters including the reorganization energy λ, the diabatic activation energy ΔG^*, and the electronic coupling element V_{AB}. These parameters and the general features of the theories are demonstrated in Figure 5.2. The λ corresponds to the energy of the final state Ψ_B at the geometric configuration q_A. The V_{AB} is given as twice the energy difference between the two adiabatic states.
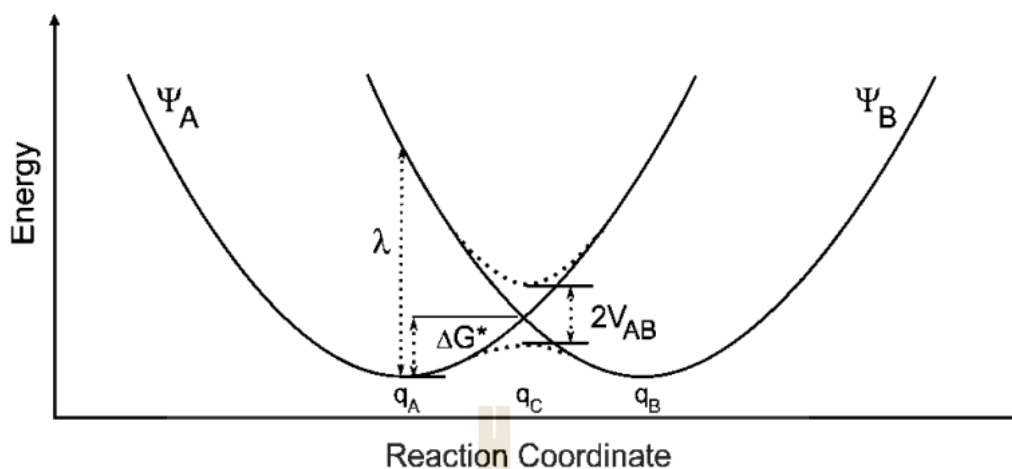
Figure 5.2 General features of Marcus-Emin-Holstein-Austin-Mott theories for symmetric polaron transfer. The potential-energy surfaces of the initial state Ψ_A and final state Ψ_B are shown with equilibrium structures q_A and q_B. The transition state between the two states is shown as q_C. λ, V_{AB}, ΔG^*, and dashed lines represent the reorganization energy, the electronic coupling element, the diabatic activation energy, and the adiabatic energy, respectively (N Aaron Deskins and Dupuis, 2007).

As illustrated in Figure 5.2, if an initial state has enough energy to overcome an activation barrier, electron will be transferred to an adjacent site, leading to the final state. The activation barrier depends strongly on the interaction between the initial and final states, which is quantified by V_{AB}. In case of the significant interaction between the initial and final states at q_C or small V_{AB}, the polaron transfer is a nonadiabatic or diabatic process where the main hopping mechanism occurs via quantum tunneling. On the other hand, if there is strong coupling or large V_{AB}, the polaron transfer is the adiabatic case where the main transfer mechanism occurs via thermal hopping (N Aaron Deskins and Dupuis, 2007).

In this thesis, we employed the CI-NEB method to achieve the polaron migration barriers. Their calculated barriers are considered adiabatic because this method implies the validity of Born-Oppenheimer approximation. To determine the adiabaticity of a polaron transfer, we must know the adiabatic activation energy barrier and the electronic coupling V_{AB}. As descried by previous computational work (Adelstein *et al.*, 2014), we can estimate V_{AB} using the Mulliken-Hush formalism within Marcus theory (Reimers and Hush, 1991). The parameter V_{AB} is related to ΔE_{12} as the following equation

$$V_{AB} = \frac{1}{2}\Delta E_{12}, \tag{5.1}$$

where ΔE_{12} is the energy difference between the adiabatic bonding and antibonding electronic states at the TS. Here, we can estimate the value of ΔE_{12} from the DOS of the TS, through the positions of the two gap states within the band gap which are below (bonding state) and above (antibonding state) the Fermi energy. These two states should be linear combinations of the initial and final polaron states.

In the adiabatic case, the reorganization energy, λ can be defined from the activation energy, E_a and the electronic coupling parameter, V_{AB} as (N. Aaron Deskins and Dupuis, 2009)

$$E_a(\text{adiabatic}) = \frac{\lambda}{4} - V_{AB}. \tag{5.2}$$

In addition, the diffusion coefficients and hopping mobility in pristine and doped systems were calculated using the kMC simulations. The carrier mobility can be expressed by the Einstein-Smoluchowski equation (Wu and Ping, 2018)

$$\mu_{ij}^{ES} = \frac{D_{ij}q}{k_B T}, \tag{5.3}$$

where D_{ij} is the diffusion coefficient tensor and q is the carrier charge. The diffusion coefficient, D can be expressed by (Wu and Ping, 2018)

$$D = \lim_{t \to \infty} \frac{\langle L(t)^2 \rangle}{2Nt}, \tag{5.4}$$

where N is the dimensionality of the kMC process, $\langle L(t)^2 \rangle$ is the mean squared displacement (MSD) ant t is the time. The MSD is determined from the hopping rate and the distance between two nearest neighbor lattice sites throughout the lattice included in the simulation. Then we can obtain hopping mobility through Equation 5.3. Here, we used the kMC algorithm reported by Wu and Ping (Wu and Ping, 2018) to estimate the polaron mobilities (see in in APPENDIX A).

From the Landau-Zener theory, the electron polaron transfer rate, k_{ET} can be defined as (Wu and Ping, 2018)

$$k_{ET} = \kappa_{el} \nu_{eff} \Gamma \exp(-E_a/k_B T), \tag{5.5}$$

where κ_{el}, ν_{eff}, and Γ represent the thermally averaged electronic transmission coefficient, effective frequency along the reaction coordinate of electron transfer, and nuclear tunneling factor (in this thesis we assumed $\Gamma = 1$ as it is only important for low temperature or light elements) (Wu and Ping, 2018), respectively.

The electronic transmission coefficient, κ_{el} can be calculated as (Wu and Ping, 2018)

$$\kappa_{el} = 2P_{LZ}/(1 + P_{LZ}), \tag{5.6}$$

where $P_{LZ} = 1 - \exp(-2\pi\gamma)$, P_{LZ} is the Landau-Zener transition probability and γ is the adiabaticity parameter which can be determined as $2\pi\gamma = \frac{\pi^{3/2}|V_{AB}|^2}{h\nu_{eff}\sqrt{\lambda k_B T}}$.

The effective frequency, ν_{eff} can be calculated from partition function as (Wu and Ping, 2018)

$$\nu_{\text{eff}} = \frac{k_{\text{B}}T}{h}\frac{Z_{\text{TS}}}{Z_{\text{GS}}} = \frac{k_{\text{B}}T}{h}\frac{\prod_i^{3N-6}\left[2\sinh\left(\frac{h\nu_i^{\text{GS}}}{2k_{\text{B}}T}\right)\right]}{\prod_i^{3N-7}\left[2\sinh\left(\frac{h\nu_i^{\text{TS}}}{2k_{\text{B}}T}\right)\right]}, \tag{5.7}$$

where Z_{TS} and Z_{GS} are the partition functions for the transition state and the ground state, respectively and ν_i represent vibrational eigenmodes of the corresponding geometry.

5.2 Polaron transport in the absence of oxygen vacancy

We explored behavior of polaron hopping to study the effect of P doping on the polaron mobility where various possible migration paths were considered as shown in Figure 5.3. We carried out CI-NEB calculations to determine the minimum energy path and the corresponding barrier. As presented in Table 5.1, P impurity has negligible effects on the polaron mobilities as the calculated hopping barriers along various paths in both systems are invariant in the range of 300 meV.
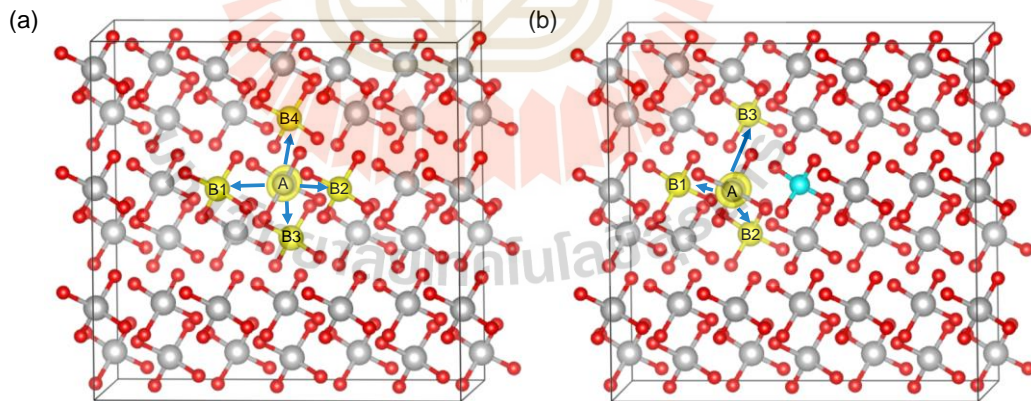
Figure 5.3 Polaron migration paths in the electron-doped (a) BiVO$_4$ and (b) P-doped BiVO$_4$. Yellow isosurface with the value of 0.02 e Å^{-3} indicates the spin density of the polaronic state at A site. The polaron hops from A site to nearest neighbor sites which are B1, B2, B3, and B4, as represented by yellow atoms. Gray, red, and blue balls represent V, O, and P atoms, respectively. Bi atoms are omitted for clarity.

Table 5.1 Calculated polaron migration barriers, E_a (meV) in the electron-doped BiVO$_4$ and P-doped BiVO$_4$. The corresponding migration paths are shown in Figure 5.3.

Pristine system		P-doped system	
Migration path	E_a	Migration path	E_a
A → B1	303	A → B1	308
A → B2	303	A → B2	315
A → B3	310	A → B3	317
A → B4	312		

In addition, the adiabaticity of a polaron transfer in pristine and P-doped BiVO$_4$ were determined where the parameters for the charge transfer rate were caculated. We first estimated V_{AB} from the calculate DOS of the TS configurations corresponding to the polaron hopping in pristine and P-doped BiVO$_4$, as shown in Figure 5.4.
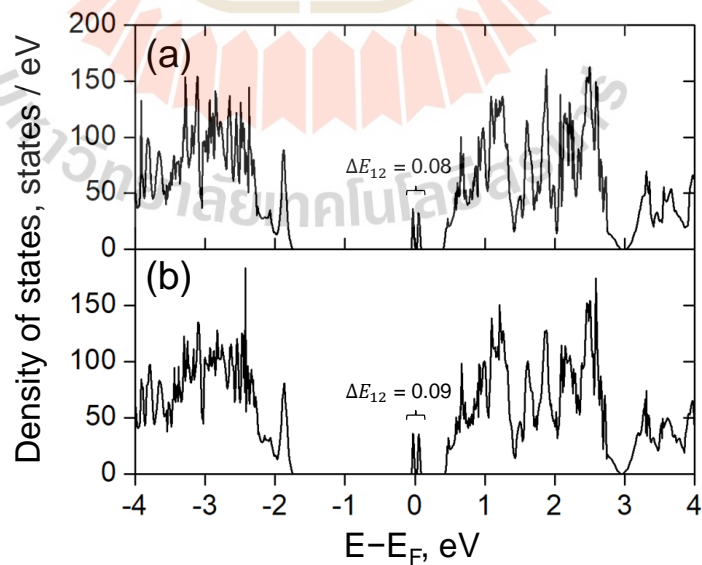
Figure 5.4 DOS of the TS configurations corresponding to the polaron hopping in (a) pristine and (b) P-doped BiVO$_4$.

From Figure 5.4, there are the two sharp peaks within the band gap which are interpreted as the bonding and antibonding states. The estimated values of V_{AB} (obtained by Equation 5.1) are significant which are 0.040 and 0.045 eV for pristine and P-doped systems, respectively. Therefore, the polaron hopping processes in both pristine and P-doped systems are adiabatic. Moreover, we obtained other parameters from Equation 5.2 and 5.5-5.7. All parameters for the charge transfer rate are listed in Table 5.2.

Table 5.2 Calculated parameters for the charge transfer rate at 300 K of the nearest neighbor hopping in pristine and P-doped $BiVO_4$ (compared with the values of pristine system obtained by the constrained DFT (CDFT) method from the previous work): hopping activation energy E_a, electronic coupling parameter V_{AB}, reorganization energy λ, effective frequency ν_{eff}, Landau-Zener transition probability P_{LZ}, electronic transmission coefficient κ_{el}.

Parameter	Pristine (this study)	P-doped $BiVO_4$ (this study)	Pristine (previous study) (Wu and Ping, 2018)
E_a (eV)	0.30	0.30	0.25
V_{AB} (meV)	40	45	91
λ (meV)	136	138	120
$h\nu_{eff}$ (meV)	184	202	276
P_{LZ}	0.23	0.26	0.60
κ_{el}	0.37	0.41	0.75

From Table 5.2, our calculated κ_{el} of 0.37 is smaller than the previously reported value using constrained DFT (CDFT) method (0.75) for the pristine system. Such mismatch may stem from the uncertainty in estimating the coupling constant,

V_{AB} (40 meV) and reorganization energy, λ (136 meV) where the ground-state theory (DFT) is used to identify the unoccupied state as discussed by Adelstein *et al* (Adelstein *et al.*, 2014). Using a more robust CDFT method yields V_{AB} of 91 meV and λ of 120 meV (Wu and Ping, 2018). Nevertheless, our calculated κ_{el} of 0.41 for the doped system is comparable to that of the pristine lattice (0.37), suggesting similar adiabaticity of polaron hopping. Overall, our computations suggest that P substitution hardly affects the behavior of polaron migration in $BiVO_4$.

5.3   Polaron transport in the presence of oxygen vacancy

For both pristine and doped systems, the formation of an V_O generates two polarons at V1 and V2 centers as denoted in Figure 4.1 and described in Chapter IV. These polarons induce a broken-symmetry lattice distortion resulting in nonequivalent polaron hopping paths. To systematically determine the behavior of polaron migration, we therefore examined various possible paths of one polaron hopping away from the V_O site while the other polaron is always trapped at the defect site.

Here, we calculated the migration barriers between nearest neighbor (NN) sites starting from the hopping of V2 to the first nearest neighbor (1NN). As illustrated in Figure 5.5(a), the migration scenario for both pristine and P-doped systems includes a consecutive hopping of V2 $\rightarrow$ 1NNs, 1NNs $\rightarrow$ 2NNs, 2NNs $\rightarrow$ 3NNs, and 3NNs $\rightarrow$ 4NNs, where the other polaron is located at V1 through the whole process. Potential energy profiles of all considered migration paths are depicted in Figure 5.5(b) and 5.5(c) for pristine and P-doped systems, respectively, where the band represents the variation of polaronic energies and barriers. The relative energies are referenced with the system containing one polaron farthest from the defect center.

For the pristine $BiVO_4$ system, as the polaron begin to move from V2 to the first nearest neighbors, V2 $\rightarrow$ 1NNs, it has to overcome a barrier in the range between 378 and 562 meV with an endothermic reaction energy from 111 to 178 meV. Such hopping path with the highest barrier of 562 meV stems from the strong interaction between the V_O formation and polaron resulting in the distorted TS structure with high TS energy. The bond distances and bond angles of VO_4 tetrahedra of its TS structure are asymmetric (V–O bond distances fluctuate between 174 and 181 pm, O–V–O bond angles vary between 103° and 113°) as depicted in Figure 5.6(a). Note that the TS structure of the perfect crystal exhibits a lower energy (300 meV) where both two V centers consist two sets of V–O bond distances (178 and 179 pm) and O–V–O bond angles (105° and 106°), Figure 5.6(b). The subsequent step, 1NNs $\rightarrow$ 2NNs, are nearly isothermal where the calculated barriers are in the range between 273 and 482 meV. This step still involves the polaron movement with a high barrier (482 meV) due to the interaction between the polaron and defect. Its TS structure is strongly distorted with the inequivalent V–O bond distances and O–V–O bond angles, which lead to relatively high TS energy, Figure 5.6(c). Nevertheless, in this step, some hopping paths exhibit relatively low barriers as they are accompanied by symmetrical TS structures. The two subsequent steps, 2NNs $\rightarrow$ 3NNs $\rightarrow$ 4NNs, are considered as isothermal changes. Their hopping barriers (284-342 meV) are comparable to that of the bulk migration where the polaron-defect interaction are vanished which hardly affects the hopping barriers. As a result, it is expected that the migration behavior in the V_O system resembles that of the perfect crystal from this step onward.
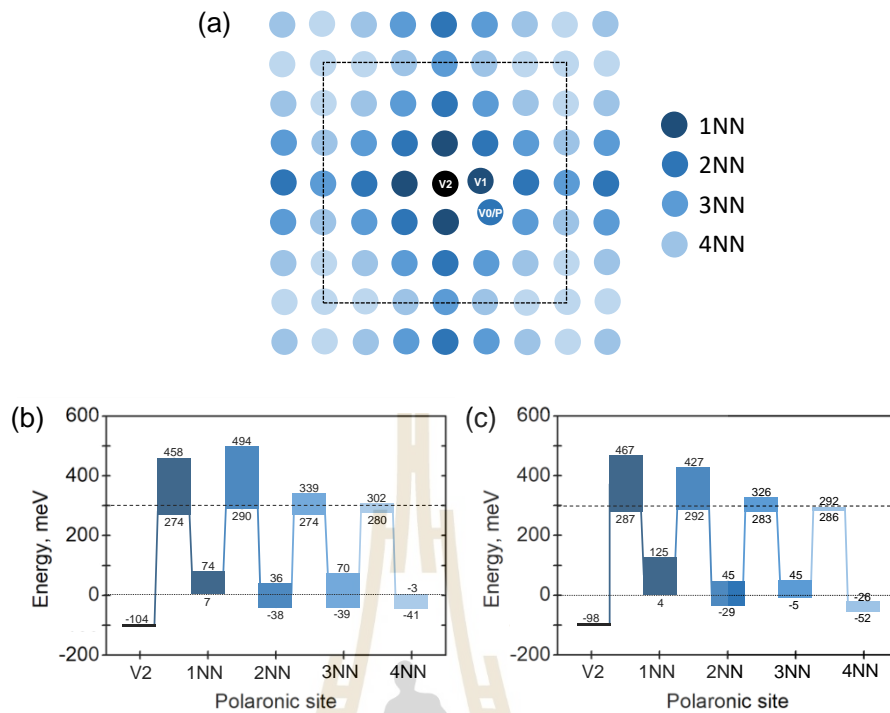
Figure 5.5 (a) Schematic illustrations of polaron migration paths in supercell (applying periodic boundary condition) of the V_O structure system, starting from the hopping of V2 to the first (1NN), second (2NN), third (3NN), and fourth (4NN) nearest neighbors, consecutively. Note that V_O generates two polarons at V1 and V2 centers, V0 and P are the O-deficient site for pristine and P-doped systems, respectively. The order of NN is referenced with V2. The distances between NN pairs are in the range of 4 Å. (b) and (c) Potential energy profiles of all considered polaron migration paths in the V_O structure of pristine and P-doped BiVO4, respectively. The relative energies are referenced with the energy of system containing one polaron farthest from the defect center for each system in the presence of V_O (which is set to be zero, dotted line). The dashed line represents the polaron hopping barrier (300 meV) in the pristine BiVO4.
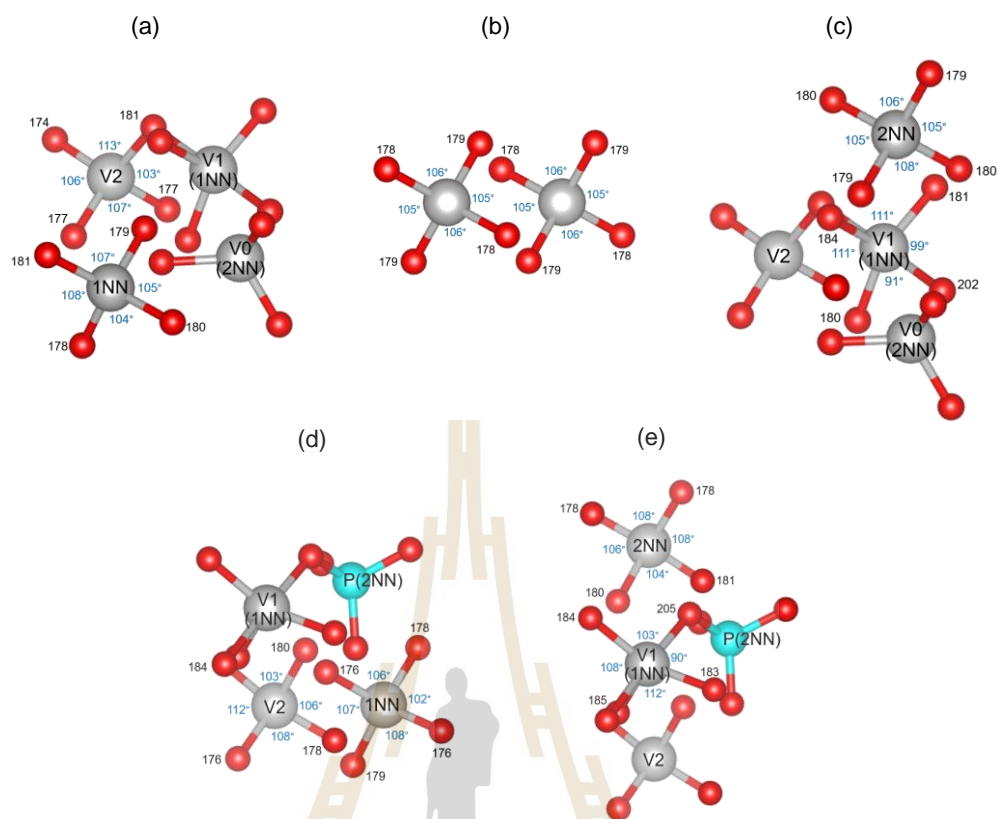
Figure 5.6 TS structures for polaron migrations between nearest neighbors (NNs), (a) V2 → 1NN path in the V_O structure of $BiVO_4$, (b) perfect crystal of $BiVO_4$, (c) 1NN → 2NN path in the V_O structure of $BiVO_4$ and (d),(e) V2 → 1NN path and 1NN → 2NN path in the V_O structure of P-doped $BiVO_4$, respectively. Gray, red, and blue balls represent V, O, and P atoms, respectively. The labelled numbers indicate the calculated bond distances (pm) and bond angles.

We now turn to describe the polaron transport in the P-doped $BiVO_4$ system with an V_O at the PO_4 unit. Similar to the movements in the pristine system, the hopping barriers of the first two steps are significantly higher than the subsequent steps. The highest barrier of 565 meV belongs to the first step which is very similar to that of the pristine system (562 meV). All these high barriers of the first two steps originate from the distorted TS structures, Figure 5.6(d) and 5.6(e), resulting in high

TS energies. The high-barrier characteristic is absence when the polaron hops further away from 2NNs onward. Their reaction energies and barriers are very similar to the migration in perfect crystal. From the potential energy profiles of various hopping paths in both systems, the behavior of polaron transport in the reduced $BiVO_4$ and P-doped $BiVO_4$ are not significantly different. The deviation of hopping barriers is quite large when polaron moves in close proximity to the defect site then the barriers become converged to the value of pristine bulk in the next steps. The strong polaron-defect interaction largely affects the polaron transport within 2NN region, where the polaron must overcome the large barrier. When the polaron moves further away from the 2NN sites, the hopping barrier becomes the same value as that of perfect crystal.

In order to accurately take into account the anisotropic polaron hopping, it is required that hopping rates of all possible pathways in the vicinity of the defect site are statistically sampled within the kMC simulations. The electron transfer rates were computed according to Landau-Zener theory as discussed in the previous section. All parameters used for computing the charge transfer rate are summarized in Table 5.2. Note that we used the pre-exponential values including effective frequency ($h\nu_{eff} = 276$ meV) and electronic transmission coefficient ($\kappa_{el} = 0.75$) as reported by Wu and Ping (Wu and Ping, 2018) since they were computed within a more robust description of the CDFT method. Upon formation of an V_O, dramatic local distortions are expected to create strong anisotropic mobility; therefore, hopping barriers of all possible pathways in the vicinity of the defect site (up to 4NNs) were used as inputs for the kMC simulations. The migration barriers included in the kMC simulations are listed in Table 5.3 and 5.4 for the pristine and doped systems, respectively. As the polaron moves farther away, its barrier resembles that of the bulk migration where the

hopping barrier of perfect crystal (0.3 eV) was used as inputs. On the contrary, the anisotropicity is much less prominent in the absence of V_O; hence, only the barriers of the nearest neighbor hopping were included in the simulations as summarized in Table 5.1. With these numerical inputs, the simulations reveal that the carrier mobilities of pristine and doped systems are quite similar in the presence and absence of V_O, Table 5.5. Our estimated mobility of the pristine system (5.05×10^{-6} cm^2 V^{-1} s^{-1}) is significantly lower than the previously calculated value (1.38×10^{-4} cm^2 V^{-1} s^{-1}) (Wu and Ping, 2018) because our input barriers are slightly higher (0.30 eV vs 0.25 eV (Wu and Ping, 2018)). Nevertheless, our calculated barriers of 0.30 eV as inputs for kMC simulations of polaron mobility are in reasonable agreement with the experimental determined value (0.29 eV) in W-doped BiVO$_4$ (Rettie et $al.$, 2013) and the computed value (0.35 eV) obtained by the hybrid functional in the electron-doped BiVO$_4$ (Kweon et $al.$, 2015). The charge transfer kinetics become sluggish in the presence of an V_O where the estimated mobilities are one magnitude lower than those systems without V_O defect, Table 5.5. Our finding is reasonably consistent with the previous works that the formation of V_O slows down the charge carrier transport in BiVO$_4$ (Cooper et $al.$, 2016; Qiu et $al.$, 2019) and other TMOs such as TiO$_4$ (Pham and Wang, 2015) and α-Fe$_2$O$_3$ (Smart and Ping, 2017). The obtained polaron mobilities at different temperatures can be used to further calculate the apparent activation energy of polaron hopping as

$$\mu(T) = A\exp(-E_{app}/k_B T). \tag{5.8}$$

Table 5.3 Calculated barriers, E_a (meV) of polaron migrations in all considered pathways of $BiVO_4$ in the presence of an V_O. The corresponding migration paths are shown in Figure 5.7.

Path (A ↔ B)	E_a	
	(A → B)	(B → A)
V2 ↔ 1NNs		
V2 ↔ V1	408	297
V2 ↔ V3	562	384
V2 ↔ V4	378	228
V2 ↔ V5	532	419
1NNs ↔ 2NNs		
V1 ↔ V6	482	479
V1 ↔ V7	283	293
V3 ↔ V0	309	346
V3 ↔ V8	420	532
V3 ↔ V9	275	329
V4 ↔ V10	273	328
V5 ↔ V6	298	297
2NNs ↔ 3NNs		
V0 ↔ V16	303	330
V0 ↔ V17	303	327
V6 ↔ V13	316	280
V6 ↔ V14	286	307
V7 ↔ V14	307	315
V7 ↔ V15	284	319
V7 ↔ V16	323	312
V8 ↔ V18	342	234
V10 ↔ V15	284	313
3NNs ↔ 4NNs		
V17 ↔ V23	290	343

Table 5.4 Calculated barriers, E_a (meV) of polaron migrations in all considered pathways of P-doped $BiVO_4$ in the presence of an V_O. The corresponding migration paths are shown in Figure 5.7.

| Path (A ↔ B)	E_a	
	(A → B)	(B → A)
V2 ↔ 1NNs		
V2 ↔ V1	498	362
V2 ↔ V3	565	342
V2 ↔ V4	385	227
V2 ↔ V5	481	380
1NNs ↔ 2NNs		
V1 ↔ V6	285	297
V1 ↔ V7	389	422
V3 ↔ V8	226	380
V3 ↔ V9	258	339
V4 ↔ V10	277	335
V5 ↔ V6	302	279
V5 ↔ V11	288	314
V5 ↔ V12	292	287
2NNs ↔ 3NNs		
V6 ↔ V13	299	281
V6 ↔ V14	285	311
V7 ↔ V14	304	309
V7 ↔ V15	302	313
V7 ↔ V16	319	309
V8 ↔ V17	312	247
V10 ↔ V15	303	310
3NNs ↔ 4NNs		
V16 ↔ V26	318	275
V16 ↔ V27	276	345
V17 ↔ V23	250	312
V17 ↔ V27	231	320
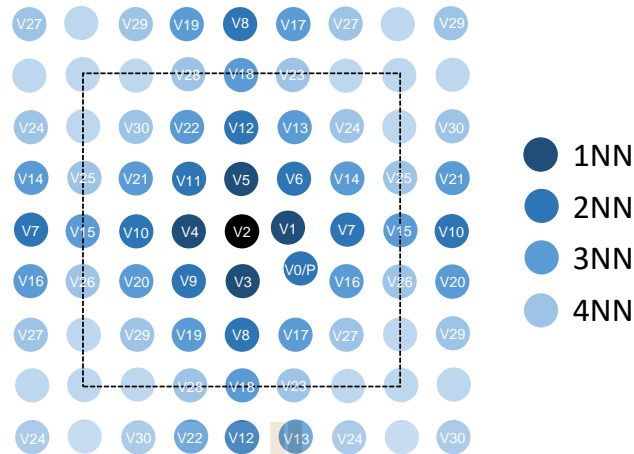
Figure 5.7 Schematic illustrations of polaron migration paths in supercell (applying periodic boundary condition) of the V_O structure system. Note that at first V_O generates two polarons at V1 and V2 centers, V0 and P are the O-deficient site for pristine and P-doped systems, respectively. The first (1NN), second (2NN), third (3NN), and fourth (4NN) nearest neighbor are referenced with V2. The distances between NN pairs are in the range of 4 Å.

Table 5.5 Electron polaron drift mobility (μ) and apparent activation energy (E_{app}) of pristine, P-doped BiVO$_4$ and the V_O structure of BiVO$_4$ and P-doped BiVO$_4$ at room temperature (300 K).

System	μ (10^{-6} cm^2 V^{-1} s^{-1})	E_{app} (meV)
Pristine	5.05	303
P-doped BiVO$_4$	4.06	308
BiVO$_4$ with V_O	1.66	391
P-doped BiVO$_4$ with V_O	0.92	407

The calculated apparent activation energies of all systems at room temperature are summarized in Table 5.5. As expected, the apparent activation energies are inversely proportional to the carrier mobilities where the higher-mobility systems exhibit lower apparent activation energy.

Moreover, polaron mobility can be estimated from the dielectric constants of the system. In particular, the hopping barrier can be estimated as

$$E_a = \frac{e^2}{4\varepsilon_p}\left(\frac{1}{r_p} - \frac{1}{R}\right), \tag{5.9}$$

where $\frac{1}{\varepsilon_p} = \frac{1}{\varepsilon_\infty} - \frac{1}{\varepsilon_0}$, ε_∞ and ε_0 are the high frequency and static dielectric constant respectively; r_p is the small polaron radius which can be defined as $r_p = \frac{1}{2}(\frac{\pi}{6})^{1/3}\bar{a}$, where $\bar{a}^{-3}$ is the number of centers per unit volume; R is the distance between polaron hopping centers (Kim *et al.*, 2015). In the absence of V_O, the calculated ε_p for pristine (9.28) and P-doped systems (8.93) are quite similar which lead to a negligible difference of E_a of only 3.9% upon doping. Similar trend is observed for the systems containing an V_O where the pristine and doped systems exhibit comparable calculated ε_p (7.59 *vs* 7.49) resulting in 1.3% difference of E_a. The relatively slow kinetics is predicted in the presence of V_O where the E_a is increased by 22.3% and 19.3% for pristine and P-doped systems, respectively. The carrier mobility obtained from the kMC simulations and estimation of barriers from dielectric constants ensure that P doping do not play a role on the hopping conduction itself as the polaron mobilities are hardly changed upon doping in the presence and absence of V_O. Its crucial role lies in the stabilization of V_O structure which could increase the number of charge carriers in the materials. Although it is expected that V_O impedes the polaron conduction, the

increased carrier concentration arising from V_O formation and light absorption could yield an improved electronic conductivity of the system.

5.4   Reference

Adelstein, N., Neaton, J. B., Asta, M. and De Jonghe, L. C. (2014). Density Functional Theory Based Calculation of Small-Polaron Mobility in Hematite. **Phys. Rev. B.** 89: 245115.

Cooper, J. K., Scott, S. B., Ling, Y., Yang, J., Hao, S., Li, Y., Toma, F. M., Stutzmann, M., Lakshmi, K. V. and Sharp, I. D. (2016). Role of Hydrogen in Defining the n-Type Character of $BiVO_4$ Photoanodes. **Chem. Mater.** 28: 5761.

Deskins, N. A. and Dupuis, M. (2007). Electron transport via polaron hopping in bulk TiO_2: A density functional theory characterization. **Phys. Rev. B.** 75: 195212.

Deskins, N. A. and Dupuis, M. (2009). Intrinsic Hole Migration Rates in TiO_2 from Density Functional Theory. **J. Phys. Chem. C.** 113: 346.

Kim, T. W., Ping, Y., Galli, G. A. and Choi, K.-S. (2015). Simultaneous Enhancements in Photon Absorption and Charge Transport of Bismuth Vanadate Photoanodes for Solar Water Splitting. **Nat. Commun.** 6: 8769.

Kweon, K. E., Hwang, G. S., Kim, J., Kim, S. and Kim, S. (2015). Electron Small Polarons and Their Transport in Bismuth Vanadate: a First Principles Study. **Phys. Chem. Chem. Phys.** 17: 256.

Natanzon, Y., Azulay, A. and Amouyal, Y. (2020). Evaluation of Polaron Transport in Solids from First-principles. **Isr. J. Chem.**

Pham, H. H. and Wang, L.-W. (2015). Oxygen Vacancy and Hole Conduction in Amorphous TiO_2. **Phys. Chem. Chem. Phys.** 17: 541.

Qiu, W., Xiao, S., Ke, J., Wang, Z., Tang, S., Zhang, K., Qian, W., Huang, Y., Huang, D. and Tong, Y. (2019). Freeing the Polarons to Facilitate Charge Transport in $BiVO_4$ from Oxygen Vacancies with an Oxidative 2D Precursor. **Angew. Chem.** 131: 19263.

Reimers, J. R. and Hush, N. S. (1991). Electronic Properties of Transition-Metal Complexes Determined from Electroabsorption (Stark) Spectroscopy. 2. Mononuclear Complexes of Ruthenium(II). **J. Phys. Chem.** 95: 9773.

Rettie, A. J. E., Lee, H. C., Marshall, L. G., Lin, J.-F., Capan, C., Lindemuth, J., McCloy, J. S., Zhou, J., Bard, A. J. and Mullins, C. B. (2013). Combined Charge Carrier Transport and Photoelectrochemical Characterization of $BiVO_4$ Single Crystals: Intrinsic Behavior of a Complex Metal Oxide. **J. Am. Chem. Soc.** 135: 11389.

Smart, T. J. and Ping, Y. (2017). Effect of Defects on the Small Polaron Formation and Transport Properties of Hematite from First-Principles Calculations. **J. Phys.: Condens. Matter.** 29: 394006.

Wu, F. and Ping, Y. (2018). Combining Landau–Zener Theory and Kinetic Monte Carlo Sampling for Small Polaron Mobility of Doped $BiVO_4$ from First-Principles. **J. Mater. Chem. A.** 6: 20025.

CHAPTER VI

CONCLUSIONS

In this thesis, the role of the P substitution in enhancing the electronic conductivity of $BiVO_4$-based photoanodes for photoelectrochemical water splitting was investigated. We utilized the computational tools based on the DFT+U method to explore the effect of P doping on (i) the change of the geometrical and electronic structures (ii) the interplay between formation of oxygen vacancies and charge transport properties of $BiVO_4$.

The impact of P doping toward the geometrical structure of $BiVO_4$ was investigated by replacing a V atom with a P atom in the $BiVO_4$ supercell. The substitution of P creates a local structure reorganization at the PO_4 unit where the average P–O bond distance is about 11% shorter than that of the VO_4 unit, leading to the elongation of Bi−O bonds of the nearest BiO_8 units (4% longer than that in pure system). To obtain insight into the electronic structures of pristine and P-doped $BiVO_4$, we calculated and analyzed their PDOS, charge transfer, and polaron formation. Computations reveal that the introduction of P impurities does not significantly affect the electronic structure feature the host system.

Next, the formation and relative stability of oxygen vacancy (V_O) in the pristine and doped systems were investigated to understand the effect of P doping on the improved charge carrier of the $BiVO_4$ photoanode. The computed defect formation energies reveal that P doping improves the reducibility of the material by lowering the

energies of V_O formation. Upon the formation of an V_O, two electron polarons are generated and localized at the two nearby V centers. We examined the behavior of the generated polarons and found that one polaron is trapped at the defect site, while the other polaron is relatively mobile.

Finally, the behavior of polaron transport and their mobilities in pristine and P-doped systems in the presence and absence of oxygen vacancies were explored by computing their migration barriers. The kMC simulations reveal that the polaron mobility and apparent activation energy of the pristine and doped systems are quite similar. Thus, P doping does not play a role on the hopping conduction itself.

From our obtained results, we can conclude that the P substitution plays an important role in the stabilization of V_O structure which could increase the number of charge carriers in the materials. Although V_O inhibits the polaron conduction, the increased carrier concentration arising from V_O formation and light absorption could yield the improved electronic conductivity of the system. The conclusion obtained here based on the macroscopic investigation explains the experimentally observed higher concentration of oxygen vacancies and improved photocatalytic efficiency of the P-doped samples. Our work sheds light on the fundamental understanding of the mechanisms responsible for high-performance P-doped $BiVO_4$ photoanodes.
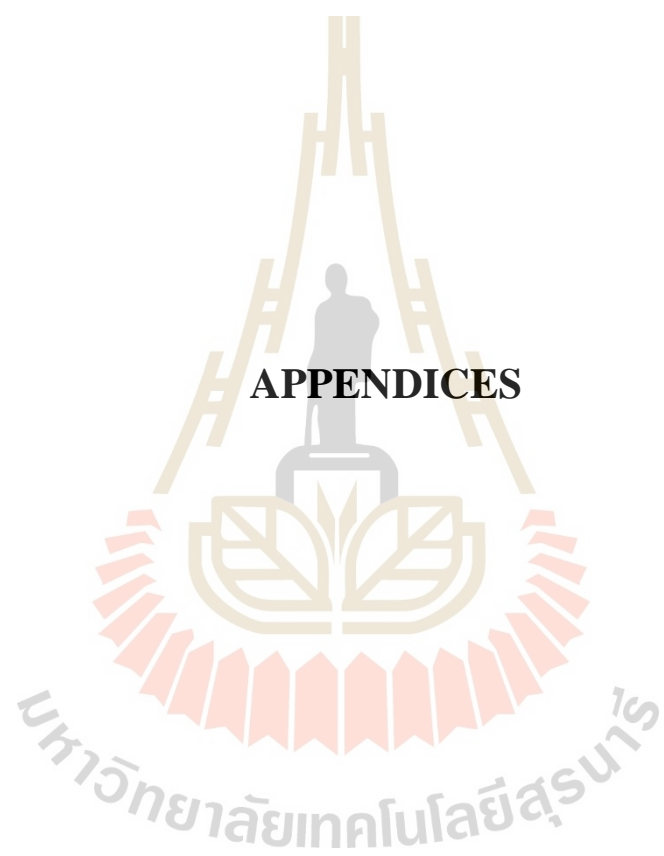
APPENDICES

APPENDIX A

KINETIC MONTE CARLO SIMULATION FOR

POLARON MOBILITY

We used kinetic Monte Carlo (kMC) simulation to predict the mobility with polaron hopping transfer rates between sites in BiVO$_4$. The kMC is a statistical method of a random process on average by means of multiple simulations. The process can be described as below [reproduced from Ref. (Wu and Ping, 2018)].

1. Set up a lattice model with multiple sites represent different V atoms. A selected group of hopping between sites are considered in the simulation, that is the first nearest neighbor (1NN) hopping.

2. Calculate all non-equivalent hopping rates (between 1NN) k_{ab} from the method as described in Chapter V with the Landau-Zener theory at a specific temperature T, where a, b are sites.

3. Choose an arbitrary site as the starting point, marked as a.

4. Randomly choose the next site b to hop to: the probability to hop to the neighbor b_i is $p_i = k_{ab_i}/\sum_j k_{ab_i}$. A random number r uniformed distributed on [0,1) is generated. The site b_i is chosen if $\sum_{j=1}^{i} p_j \leq r < \sum_{j=1}^{i+1} p_j$.

5. A random number r' uniformed distributed on [0,1) is generated, and the time cost $\Delta t = -\ln(r')/\sum_i k_{ab_i}$.

6.   Repeat the above two steps, and record the squared displacement L^2 and time per S streps until sampled M times, where S and M should be sufficiently large. The total simulation time is given by $MS\langle\Delta t\rangle$.

7. Repeat step 3 to 6 for N times, and take the average of these $L^2 - t$ curve (each consists of M points). This would give an approximately linear curve from which we can fit the diffusion coefficient D.

8. Repeat the above steps for K times and get a set of diffusion coefficient D_i ($i = 1, 2, ..., K$) and following mobility μ_i ($i = 1, 2, ..., K$). We can estimate the error of the mobility from this dataset as $\max(\mu_i) - \min(\mu_i)$.

In this thesis, the code used for kMC simulation to calculate the polaron mobility and the apparent activation energy is written in Python. The program reads the excel input file, containing energy barrier of polaron hopping, lattice vectors of BiVO$_4$, and position of 36 V sites in direct coordinate. The example of excel file is presented in Table A.1-A.3. The code is shown in Table A.4.

Table A.1 Example of excel file of the energy barrier (in meV) of polaron hopping.

	A	B	C	D	E	F	G	H	I	J	K	L	M	N
1	q	V1	V2	V3	V4	V5	V6	V7	V8	V9	V10	V11	V12	V13
2	V1	-	-	-	-	-	-	-	-	-	307	-	307	-
3	V2	-	-	-	-	-	-	-	-	-	307	307	-	-
4	V3	-	-	-	-	-	-	-	-	-	-	307	307	-
5	V4	-	-	-	-	-	-	-	-	-	-	-	-	307
6	V5	-	-	-	-	-	-	-	-	-	-	-	-	307
7	V6	-	-	-	-	-	-	-	-	-	-	-	-	-
8	V7	-	-	-	-	-	-	-	-	-	-	-	-	-
9	V8	-	-	-	-	-	-	-	-	-	-	-	-	-
10	V9	-	-	-	-	-	-	-	-	-	-	-	-	-
11	V10	307	307	-	-	-	-	-	-	-	-	-	-	-
12	V11	-	307	307	-	-	-	-	-	-	-	-	-	-
13	V12	307	-	307	-	-	-	-	-	-	-	-	-	-
14	V13	-	-	-	307	307	-	-	-	-	-	-	-	-
15	V14	-	-	-	-	420	384	-	-	-	-	-	-	-
16	V15	-	-	-	307	-	419	-	-	-	-	-	-	-
17	V16	-	-	-	-	-	-	307	307	-	-	-	-	-
18	V17	-	-	-	-	-	-	-	307	312	-	-	-	-
19	V18	-	-	-	-	-	-	307	-	315	-	-	-	-
20	V19	-	-	-	-	-	-	-	-	-	307	-	-	307
21	V20	-	-	-	-	-	-	-	-	-	-	307	-	-
22	V21	-	-	-	-	-	-	-	-	-	-	-	307	-
23	V22	-	-	-	-	-	-	-	-	-	-	-	-	307
24	V23	-	-	-	-	-	-	-	-	-	-	-	-	-

Table A.2 Example of excel file of the lattice vectors of BiVO4.

	A	B	C	D	E	F	G	H	I	J	K	L	M	N
1	latx	laty	latz											
2	15.580	0.000	0.000											
3	-0.103	15.269	0.000											
4	0.000	0.000	11.697											
5														
6														
7														
8														
9														
10														
11														
12														
13														
14														
15														
16														
17														
18														
19														
20														
21														
22														
23														
24														

Table A.3 Example of excel file of the position of V sites in direct coordinate.

	A	B	C	D	E	F	G	H	I	J	K	L	M	N
1	site	posa	posb	posc										
2	V1	0.000406	0.083001	0.124895										
3	V2	0.999595	0.415766	0.122239										
4	V3	0.000015	0.748785	0.126083										
5	V4	0.333110	0.081480	0.123463										
6	V5	0.333308	0.414196	0.122337										
7	V6	0.335368	0.746392	0.127600										
8	V7	0.668139	0.083714	0.125389										
9	V8	0.665802	0.415546	0.126324										
10	V9	0.667003	0.750983	0.126237										
11	V10	0.001133	0.251538	0.876061										
12	V11	0.999001	0.583193	0.873901										
13	V12	0.000926	0.917384	0.877667										
14	V13	0.332959	0.249869	0.876631										
15	V14	0.335228	0.584309	0.878774										
16	V15	0.333252	0.916175	0.879788										
17	V16	0.666521	0.249649	0.875569										
18	V17	0.664296	0.583645	0.872065										
19	V18	0.668328	0.918518	0.878944										
20	V19	0.166335	0.251131	0.624694										
21	V20	0.163827	0.583663	0.626613										
22	V21	0.165816	0.917319	0.625985										
23	V22	0.497572	0.251219	0.623420										
24	V23	0.518094	0.627353	0.566583										

Table A.4 Python code used for calculating the polaron mobility and the apparent activation energy.

```
Program: kinetic Monte Carlo Simulation
Author:  Lappawat Ngamwongwan; Computational Catalysis (COMSCAT) Group
Insitute: Suranaree University of Technology
System:  BiVO4 3x3x1
```

Table A.4 (Continued).

```
######################## Library import ###############################
import numpy as np
import pandas as pd
import matplotlib.pyplot as plt
plt.rcParams.update({'font.size': 14})

##################### input parameters ###############################
input_file = 'pure.xlsx'
H_ab       = 91/1000  # electronic coupling in eV
lamda      = 1.20     # reorganization energy in eV
hv_eff300  = 276/1000 # effective frequency at 300 K in eV
Gamma      = 1        # nuclear tunneling factor
T          = 300      # temperature in K

############################# Controls ###############################
S   = 10               # numbers of step per record
M   = 100              # numbers of record per sampling
N   = 100              # numbers of sampling
K   = 16               # numbers of calculation

############################ Constants ###############################
h  = 4.1356675E-15   # Planck's constant in eV s
kb = 8.617333262E-5  # Boltzmann' constant in eV/K
pi = 3.14159         # Pi constant
ND = 3               # dimensionality (3D)
q  = 1.0             # elementary charge in eV/V

######################################################################
### Begin: load data fron excel file #################################
def readInput(file):
    ### nsites   : the number of considering sites
    ### barriers : the array of energy barrier of polaron hopping
    ### pos      : the position of ith site in direct coordinate
    ### nn       : the nearest neighbor sites for each site
    ### lat      : lattice constant [a, b, c]
    df1 = pd.read_excel(file, sheet_name='barriers')
    df2 = pd.read_excel(file, sheet_name='position')
    df3 = pd.read_excel(file, sheet_name='lattice')
    nsites = (len(df1.columns)-1)
    print('The number of V-sites: %2d\n' %nsites)
    barriers = df1[df1.columns[1:]].to_numpy(copy=True)
    print('The matrix of energy barrier in meV:\n', barriers)
    pos = df2[df2.columns[1:]].to_numpy(copy=True)
    print('\nThe position of each site in direct coordinate:\n', pos)
    lat = df3[df3.columns[:]].to_numpy(copy=True)
    print('\nlattice parameters:\n', lat)
    return nsites, barriers, pos, lat
def findNN():
    nn = []
    print('\nnearest neighbor:')
    for i in range(nsites):
```

Table A.4 (Continued).

```
        tmp_i = []
        for j in range(nsites):
            if barriers[i, j] > 0 :
                tmp_i.append(j+1)
        nn.append(tmp_i)
        print('atom %2d: '%(i+1), tmp_i)
    return nn

def calculateDisp(nsites, barriers):
    disp = np.zeros((nsites,nsites))
    for i in range(nsites):
        for j in range(nsites):
            if True:
                dr = [0.0,0.0,0.0]
                for k in range(3):
                    tmp = abs(pos[i][k]-pos[j][k])
                    if (abs(tmp)>0.5):
                        tmp = 1-abs(tmp)
                    dr[0] = dr[0] + (tmp*lat[0][k])
                    dr[1] = dr[1] + (tmp*lat[1][k])
                    dr[2] = dr[2] + (tmp*lat[2][k])
                dd = np.sqrt(dr[0]**2+dr[1]**2+dr[2]**2)
                disp[i][j] = dd
    print('displacement matrix (d):\n')
    print(disp)
    print('\n')
    return disp

def calculateRate(nsites, barriers, TT, verbose=False):
    ##### calculate parameters
    ### twopigamma : adiabaticity parameter
    ### P_LZ       : Landau-Zener transition probabiliy
    ### kappa      : electronic transition coefficient
    ### k_rate     : electron transfer rate
    ### Z_ratio    : partition function ratio
    Z_ratio   = hv_eff300/kb/300*h
    hv_eff    = Z_ratio*kb*TT/h
    twopigamma = (pi**(1.5))*((H_ab)**2)/hv_eff/np.sqrt(lamda*kb*TT)
    P_LZ  = 1-np.exp(-twopigamma)
    kappa = 2*P_LZ/(1+P_LZ)
    if verbose==False:
        print('2\u03C0\u03B3  : %6.3f' %twopigamma)
        print('P_LZ : %6.3f' %P_LZ)
        print('\u03BA    : %6.3f\n' %kappa)
    k_rate = np.zeros((nsites,nsites))
    for i in range(nsites):
        for j in range(nsites):
    if barriers[i][j] != 0:
```

Table A.4 (Continued).

```
                v_eff_per_s = hv_eff/h
                k_rate[i][j] = kappa * v_eff_per_s * Gamma * np.exp(-
(barriers[i][j])/1000/kb/TT)
    if verbose == False:
        print('electron transfer rate (k)')
        print(k_rate)
        print('\n')
    return k_rate

def getRate(i_site,f_site):
    return k_rate[i_site-1,f_site-1]
def getDisp(i_site,f_site):
    return disp[i_site-1,f_site-1]
def getNN(i_site):
    return nn[i_site-1]
def model(S,M,N,TT):
    Mu = []
    for n in range(N):
        # random initial site
        site = np.random.randint(1,nsites+1)
        L2_sample = [0.0]
        t_sample = [0.0]
        for m in range(M):
            dT  = 0.0
            init_site = site
            cnt[site-1] = cnt[site-1]+1
            for s in range(S):
                #print('\nstep: %02d' %s)
                #print(site)       # current site
                ### step1-checking-configuration
                nn1 = getNN(site)
                #print(nn1)        # the first nearest neighbor
                ### step2-updating-configuration
                k_bar = [0.0]      # collective rate
                for i in nn1:
                    if i > 0:
                        #print(site,i)
                        k_bar.append(k_bar[-1]+getRate(site,i))
                Q = k_bar[-1]
                k_bar = k_bar/Q
                #print(k_bar)
                r1 = np.random.random()
                #print(r1)
                for i in range(len(k_bar)):
                    if r1 < k_bar[i]:
                        #print(i,nn1[i-1])
                        #print(k_bar[i-1],k_bar[i])
                        site = nn1[i-1]
```

Table A.4 (Continued).

```
                       break
                ### step3-updating-time
                r2 = np.random.random()
                dt = -np.log(r2)/Q
                #print(dt)
                dT = dT + dt
            final_site = site
            dL2 = getDisp(init_site,final_site)**2
            L2_sample.append(L2_sample[-1]+dL2)
            t_sample.append(t_sample[-1]+dT)
        L2_sample = np.array(L2_sample)
        t_sample  = np.array(t_sample)
        t_sample  = t_sample[:,np.newaxis]
        slope, _, _, _ = np.linalg.lstsq(t_sample,
L2_sample,rcond=None)
        D = slope/ND/2          # in A2/s
        mu = D*q/kb/TT          # in A2/V/s
        mu = mu/10**16          # in cm2/V/s
        Mu.append(mu)
        #print('N=%d mu=%10.3E' %(n,mu))
    Mu = np.array(Mu)
    return L2_sample, t_sample, Mu.min(), Mu.max(), Mu.mean(),
Mu.std()


### initial setting ##########################################
nsites, barriers, pos, lat = readInput(input_file)
nn     = findNN()
disp   = calculateDisp(nsites, barriers)
cnt = np.zeros(nsites)

## mode 1: basic calculation at 300K
################################################################
print('mode 1: basic calculation of electron mobility at 300K')
k_rate = calculateRate(nsites, barriers,T)
print('electron drift mobilities [cm^2/s]')
print(' N     mean        SD         min         max')
for k in range(K):
    L2_sample, t_sample, minn, maxx, mean, std = model(S,M,N,T)
    plt.plot(t_sample*10**9,L2_sample*10**(-3))
    print('%2d %10.3e %10.3e %10.3e %10.3e'
%(k+1,mean,std,minn,maxx))
plt.title('square displacement vs time')
plt.xlabel('time (ns)')
plt.xlim(left=0)
plt.ylim(bottom=0)
plt.ylabel(r'displacement square (10$^3$ cm$^2s^{-1}$)')
plt.show()
```

Table A.4 (Continued).

```
print('polaron site counting')
plt.bar(range(1,nsites+1,1),cnt)
plt.xlim((0,nsites+1))
plt.xticks(range(1,nsites+1))
plt.xlabel('polaron site')
plt.ylabel('time counting')
plt.show()
######################################################################

# mode 2: varying temperature from 100 to 1000 K
######################################################################
print('mode 2: varying temperature')
Tmin = 50
Tmax = 500
Tstep = 50
print('electron drift mobilities [cm^2/s]')
print('  T      mobility(mu)      ln(mu)      1/T')
oneot = []
lnmu  = []
for TT in np.arange(Tmin,Tmax+Tstep/2,Tstep):
    k_rate = calculateRate(nsites, barriers, TT, True)
    _,_,_, _, mean, _ = model(S,M,N,TT)
    tmp_lnmu = np.log(mean)
    tmp_oneot = 1/TT
    print('%4d    %10.3e %10.3f %10.5f'
%(TT,mean,tmp_lnmu,tmp_oneot))
    lnmu.append(tmp_lnmu)
    oneot.append(tmp_oneot)
plt.plot(oneot,lnmu,'b.')
plt.title(r'electron mobility ($\mu$) vs temperature')
plt.xlabel(r'1/T (K$^{-1}$)')
plt.ylabel(r'ln($\mu$)')
oneot = np.array(oneot)
slope, bb = np.polyfit(oneot, lnmu, 1)
plt.plot(oneot,(slope*oneot+bb),'r-')
plt.show()
E_eff = slope*(-1)*kb      # Effective barrier in eV
E_eff = E_eff*1000         # Effective barrier in meV
print('effective barrier: %6.1f meV' %E_eff)
```

Reference

Wu, F. and Ping, Y. (2018). Combining Landau–Zener Theory and Kinetic Monte Carlo Sampling for Small Polaron Mobility of Doped BiVO$_4$ from First-Principles. **J. Mater. Chem. A.** 6: 2002.

APPENDIX B

PUBLICATION AND PRESENTATIONS

B.1 List of publication

Ngoipala, A., Ngamwongwan, L., Fongkaew, I., Jungthawan, S., Hirunsit, P., Limpijumnong, S., and Suthirakun, S. (2020). On the Enhanced Reducibility and Charge Transport Properties of Phosphorus-Doped $BiVO_4$ as Photocatalysts: A Computational Study. **J. Phys. Chem. C** 124: 4352.

B.2 List of presentations (poster)

Ngoipala, A., Jungthawan, S., and Suthirakun, S. (January 2019). Role of P-doping on the Enhanced Photoelectrochemical Performance of $BiVO_4$-based Photoanodes: A First-principles Study. **The 2nd Taiwan-Thailand-Vietnam Workshop on Theoretical and Computational Chemistry (TTV2)**. Sirindhorn Science Home, Thailand Science Park, Pathum Thani, Thailand.

Ngoipala, A., Jungthawan, S., and Suthirakun, S. (November 2019). Role of P-doping on the Enhanced Photoelectrochemical Performance of $BiVO_4$-based Photoanodes: A First-principles Study. **The International Centre for Theoretical Physics (ICTP) Asian Network School and Workshop on Complex Condensed Matter Systems 2019**. National Institute of Physics, University of Philippines Diliman, Quezon city, Philippines.

Manuscript published in The Journal of Physical Chemistry C

(journal impact factor = 4.270)

Article

On the Enhanced Reducibility and Charge Transport Properties of Phosphorus-Doped BiVO₄ as Photocatalysts: A Computational Study

Apinya Ngoipala, Lappawat Ngamwongwan, Ittipon Fongkaew, Sirichok Jungthawan, Pussana Hirunsit, Sukit Limpijumnong, and Suwit Suthirakun*

ACCESS | 📊 Metrics & More | 📄 Article Recommendations | 🆘 Supporting Information

ABSTRACT: Phosphorus (P)-doped BiVO₄ has been proposed as a promising photoanode for water splitting as it exhibits significant improvement of photocurrent density and photocatalytic O₂ evolution rate. Previous findings suggest that substitution of V with P induces lattice polarization, which facilitates electron−hole separation. However, little attention has been paid to the mechanism underlying the observed changes in electronic conductivity due to oxygen vacancies. In this work, we carry out first-principles calculations to study the effect of P doping on the stability of oxygen vacancies and charge transport properties of BiVO₄ photocatalysts. Our computations reveal improved reducibility of P-doped BiVO₄ as reflected in the lower energies of oxygen vacancy formation. The generated oxygen vacancy yields two electron polarons localized at the two nearest V centers, where one polaron is always trapped at the defect site. The calculated polaron hopping barriers and their mobilities obtained from kinetic Monte Carlo simulations indicate that the P impurity by itself does not significantly alter the behavior of polaron transport. Hence, P doping improves reducibility of the material, which, in turn, increases the number of charge carriers and improves the electronic conductivity, which could lead to superior photocatalytic activity. These results can explain the experimentally observed higher concentration of oxygen vacancies and the enhancement of photocurrent density of P-doped BiVO₄. This study provides valuable insights for designing doping strategies to improve the photocurrent density of photocatalysts.
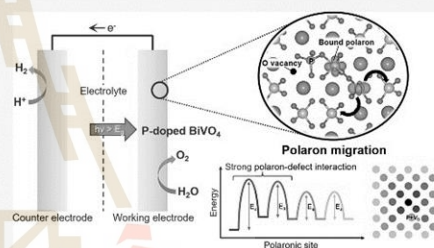
1. INTRODUCTION

Photoelectrochemical (PEC) water splitting has received extensive attention as an approach for clean hydrogen production.[1,2] Numerous efforts have been made to design and develop efficient transition-metal oxide (TMO) semiconductors as photocatalysts in PEC cells.[3,4] Recently, bismuth vanadate (BiVO₄) has been identified as one of the most promising photoanode materials for solar water oxidation to O₂ because it possesses unique physical and electrochemical properties, including the ability to effectively harvest sunlight in the visible spectral region and high stability under electrochemical conditions.[5−9] In particular, among various crystalline phases of BiVO₄, monoclinic scheelite (ms-) BiVO₄ exhibits the highest photocatalytic activity as the distortion of VO₄ tetrahedra creates local polarization, which could facilitate the separation of photogenerated electron−hole pairs.[8,9]

Despite the mentioned advantages, BiVO₄ still suffers from major limitations such as extreme recombination of photogenerated electron−hole pairs,[10,11] low electrical conductivity,[12,13] and poor water oxidation kinetics,[14] resulting in a main bottleneck for practical PEC performance. Such low intrinsic conductivity and mobility is typically encountered in various

TMOs due to the slow thermally activated hopping conduction instead of fast band conduction in group A semiconductors.[15,16] In TMOs such as BiVO₄, an extra electron prefers to localize at one transition-metal (TM) center due to strong electron−electron repulsion in contracted d orbitals and thereby reduces TM^{n+} to $TM^{(n-1)+}$. The trapped electrons are accompanied by local distortion of the surrounding lattice, leading to the formation of small polarons. The small polarons can undergo thermally activated hopping from one TM site to the nearby site, which is much slower than the band conduction (on the order of 0.1 cm² V⁻¹ s⁻¹ electron mobility for BiVO₄ compared to 1450 cm² V⁻¹ s⁻¹ for Si).[17]

To improve the charge transport kinetics of BiVO₄, research has been focused on developing strategies to overcome these drawbacks, including morphology control,[18−20] composite structure (heterojunction formation),[21−24] oxygen evolution

Manuscript published in The Journal of Physical Chemistry C

(journal impact factor = 4.270)

catalyst loading,[10,14,25] defect formation (oxygen vacancy creation),[26-30] and doping.[26-38] Both experimental and theoretical studies have reported that substitutional doping at the V site (W,[26,31,32] Mo,[26,31-33] P[27,34-36]), Bi site (Sm,[37] Yb,[37] Ce[38]), or O site (Se,[28] N[29,30]) could enhance electron–hole separation, carrier mobilities, and conductivities of the BiVO$_4$ photoanode. In particular, it has been shown by several studies that addition of a small amount of phosphorus impurities significantly improves the photocurrent density, photocatalytic O$_2$ evolution rate, carrier concentrations, and mobility.[27,34-36] Computations based on density functional theory (DFT) reveal that substitution of P at the V site increases the electron density at the surrounding O atoms, leading to polarization of P–O bonds, which could facilitate charge separation and improve photocatalytic activity.[36] Furthermore, the electron density at the top of the valence band could increase carrier concentration in the material.[34,36] Nevertheless, one experimental study based on X-ray photoelectron spectroscopy (XPS) suggests that P-doped samples contain a noticeable amount of oxygen vacancies, which could enhance charge transport properties.[27]

Such ambiguous explanations on the origin of superior electrochemical performance of P-doped BiVO$_4$ have motivated us to further explore the fundamental role of P doping in the formation of oxygen vacancies and corresponding charge transport properties. Therefore, it is the objective of this work to utilize computational tools based on the DFT + U method to study the effect of P substitution on the interplay between the formation of oxygen vacancies and charge transport properties. We first examined the geometrical and electronic structures of the doped system and compared with those of pristine BiVO$_4$. The behavior of polaron formation and migration in both systems was also explored. Then, we computed the defect formation energies of oxygen vacancy structures at various charged states to better understand the role of P doping in reducibility. Finally, we calculated the migration barriers of electrons originated from the formation of oxygen vacancy and their mobilities to determine the interaction between polarons and the defect site. The obtained fundamental understanding could be used to rationally design doping strategies to obtain high-performance photocatalysts.

2. COMPUTATIONAL DETAILS

We carried out first-principles calculations using the spin-polarized DFT + U approach with a periodic supercell model as implemented in the Vienna Ab initio Simulation Package (VASP 5.3).[39-41] The projector-augmented wave method[42,43] was used to describe electron–ion interactions, where Bi $5d^{10}6s^26p^3$, V $3p^63d^34s^2$, O $2s^22p^4$, and P $3s^23p^3$ were treated as valence electrons. Their wave functions were expanded in the plane-wave basis with a cutoff energy of 450 eV. The exchange–correlation functional was approximated using the generalized gradient approximation in the Perdew, Burke, and Ernzerhof form.[44] We employed the Dudarev approach[45] for DFT + U calculations with $U_{3d}(V) = 2.7$ eV[31] to correct for the self-interaction error inherent in the current exchange–correlation functional when applied to transition metals with tightly bound d electrons, such as V in BiVO$_4$ systems. This U value has been used to properly describe the behavior of polaron formation in Mo/W-doped BiVO$_4$.[31] The calculated hopping barrier of 0.3 eV is consistent with the experimentally determined value (0.29 eV) in W-doped BiVO$_4$[46] and the hybrid functional calculated value (0.35 eV) in electron-doped

BiVO$_4$.[47] A Gaussian smearing technique (σ = 0.05 eV) was used during structural relaxations, where the calculated energies were extrapolated to zero smearing width.

To study the role of P doping in the reducibility and transport properties of charge carriers in the BiVO$_4$ lattice, we constructed a 3 × 3 × 1 supercell of Bi$_{36}$V$_{36}$O$_{144}$ using the experimental lattice parameters of the ms-BiVO$_4$ unit cell.[48] The supercell model contains 216 atoms, which corresponds to 36 BiVO$_4$ formula units. The P-doped BiVO$_4$ system was created by replacing a V atom with a P atom to yield a 2.8% doping concentration, which is in the range of experimental values.[27,34,35] The most stable oxygen vacancy structures for the pristine and doped systems were achieved by removing an O atom at various possible positions, where the lowest energy structures were identified. For structural optimization, we sampled the Brillouin zone with a single k-point at the Γ-position. Internal coordinates were relaxed until the forces were smaller than 0.02 eV Å^{-1}. We used the tetrahedron smearing method with Bloch corrections with a denser k-point grid of 2 × 2 × 2 Γ-centers to accurately calculate the projected density of states (PDOS).

In this work, polaron migration was described by the transfer of electrons accompanied by a lattice distortion along a one-dimensional trajectory on the Born–Oppenheimer surface.[50] We adopted the climbing image nudged elastic band (CI-NEB) method[51] to determine the minimum energy path of polaron transfer. The CI-NEB approach allows for ionic relaxation of each configuration along the migration path. The transition state (TS) is located at the saddle point of the reaction coordinate, where the energy difference between TS and the initial state yields the migration barrier. The calculated barriers are considered adiabatic because this method implies the validity of the Born–Oppenheimer approximation. Various possible migration paths were examined to understand the behavior of electron polarons in the pristine and doped systems, in the presence and absence of an oxygen vacancy. The kinetic Monte Carlo (kMC) simulations were carried out to take into account the anisotropic hopping in the pristine and doped systems. We used the kMC algorithm reported by Wu and Ping[52] to estimate the polaron mobilities. The hopping rate and the distance between two nearest-neighbor lattice sites throughout the lattice were included in the simulation. In addition, the hopping barriers were estimated by computing the high-frequency and static dielectric constants using the 2 × 2 × 1 supercell with density functional perturbation theory.[49]

3. RESULTS AND DISCUSSION

3.1. Geometrical and Electronic Structures. ms-BiVO$_4$ belongs to the space group $I2/b$ with lattice parameters a = 5.1935 Å, b = 5.0898 Å, c = 11.6972 Å, and γ = 90.387°.[48] As illustrated in Figure S1a, its unit cell contains 4 Bi atoms, 4 V atoms, and 16 O atoms. Each V atom is coordinated by four O atoms forming a distorted VO$_4$ tetrahedron, each Bi atom is coordinated by eight O atoms forming a distorted BiO$_8$ dodecahedron, and each O atom connects to one V atom and two Bi atoms. The significant distortion in ms-BiVO$_4$ is caused by Bi 6s lone-pair electrons.[53] The optimized pristine structure exhibits two sets of the average V–O bond distances (1.750 and 1.753 Å) and four sets of the average Bi–O bond distances (2.419, 2.431, 2.462, and 2.503 Å). These values are consistent with the experimental results (V–O bond distances are 1.69 and 1.77 Å and Bi–O bond distances are 2.354, 2.372,

Manuscript published in The Journal of Physical Chemistry C

(journal impact factor = 4.270)

Article

2.516, and 2.628 Å),[48] which validates the methodology used in this study.

To explore the impact of P doping on the local structure of $BiVO_4$, we replaced a V atom with a P atom in the $3 \times 3 \times 1$ $BiVO_4$ supercell, as shown in Figure S1b. The substitution of P creates a local structural reorganization at the PO_4 unit. As depicted in Figure 1 and summarized in Table 1, the average
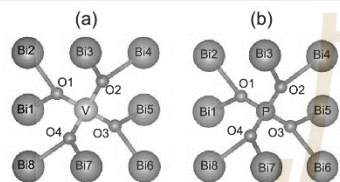

Figure 1. Local structures of (a) pristine and (b) P-doped $BiVO_4$.

Table 1. Calculated Bond Distances (Å) of Pristine and P-Doped $BiVO_4$[1]

bond distance	pristine $BiVO_4$	P-doped $BiVO_4$	variation (%)
V(P)−O1	1.749	1.564	−10.58
V(P)−O2	1.752	1.569	−10.45
V(P)−O3	1.750	1.564	−10.63
V(P)−O4	1.754	1.569	−10.55
			−10.55 ave.
Bi1−O1	2.503	2.655	+6.07
Bi2−O1	2.429	2.489	+2.47
Bi3−O2	2.469	2.592	+4.98
Bi4−O2	2.420	2.480	+2.48
Bi5−O3	2.502	2.655	+6.12
Bi6−O3	2.428	2.494	+2.72
Bi7−O4	2.461	2.589	+5.20
Bi8−O4	2.417	2.483	+2.73
			+4.10 ave.

[1]Their structures are shown in Figure 1.

P−O bond distance is about 11% shorter than that of VO_4, suggesting a relatively strong interaction between P and the surrounding O atoms in the lattice. There are two sets of P−O bond distances in the PO_4 tetrahedron, which are 1.564 and 1.569 Å. These results are consistent with those of the previous studies.[34,36] The relaxation of the PO_4 tetrahedron in turn leads to the elongation of Bi−O bonds of the nearest BiO_8 units. The average distance of these Bi−O bonds in the P-doped system is slightly longer than that of the pristine system by about 4%.

To obtain insight into the electronic structures and bonding properties of pristine and P-doped $BiVO_4$, we calculated and analyzed their PDOS. It can be seen from Figure S2a that pristine $BiVO_4$ exhibits semiconducting character with a calculated band gap of 2.17 eV, which is slightly smaller than the experimental value $(2.4 \text{ eV})^{[8,9]}$ due to the well-known underestimation of band gaps in DFT.[54] The valence band primarily comprises O 2p states with a small contribution from Bi 6s states at the valence band maximum (VBM). The conduction band mainly consists of V 3d states with some hybridization of O 2p states. The distorted VO_4 tetrahedron induces crystal field splitting of d_{z^2}, $d_{x^2-y^2}$, and other e states, as discussed in previous computational works.[47] It can be seen

from Figure S2b that P doping does not significantly affect the electronic structure of the material as their calculated electronic structures exhibit similar band gaps and DOS features. The increased DOS due to doping at the top of the valence band (−0.7 eV) is insignificant (0.1%). This is expected because P substitution at the V site is considered a homovalent doping where there is no extra charge generated upon doping. Our finding is somewhat different from the previous results that the band gap is enlarged upon P doping.[34,36] Such a disagreement may stem from the low doping concentration (2.8%) in our model study.

The change in charge distribution occurred due to the introduction of P impurities was examined by carrying out the Bader charge analysis. As summarized in Table S1, the amount of charge transfer from a P atom to neighboring O atoms is larger than that from a V atom to O atoms in pristine $BiVO_4$. In the case of the pristine system, the V atom has 2.843 electrons and the four O atoms in VO_4 have 7.047, 7.048, 7.050, and 7.053 electrons. In the case of the P-doped system, the P atom has 1.378 electrons and the charge of each O atom in PO_4 is very similar, where one O atom has 7.435 electrons and the others have the same number of electrons (7.433). Our calculated values are quantitatively different from those reported in other DFT studies[34,36] that the charge of O atoms in PO_4 fluctuates between 7.406 and 7.453 electrons,[32] where more charge is accumulated in one pair than that in the other pair of O atoms in PO_4.[34]

Next, we examined the behavior of polaron formation and migration in the pristine and doped systems. We added an extra electron in the supercell, where charge neutrality of the system is ensured by a compensating homogeneous background charge. A small perturbation to the V−O bonds of a VO_4 unit was made to break the lattice symmetry and allow for electron localization at the V center. The calculated PDOS shows that the added electron in the pristine and doped systems occupies the low-lying energy state of V d_{z^2} and form a deep localized state at 1.03 eV below the conduction band, Figure 2. Upon electron localization, the V center is reduced from V^{5+} to V^{4+}, which, in turn, induces an elongation of V−O bonds of the reduced VO_4 unit by 8 pm, leading to the formation of a small polaron. It can be seen that the formation of a small polaron in both pristine and doped systems occurs in
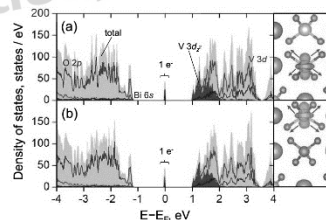
Figure 2. PDOS of electron-doped (a) $BiVO_4$ and (b) P-doped $BiVO_4$. Spin density of the polaronic state (with an isosurface value of 0.02 e Å^{-3}) of the pristine and P-doped systems are shown in the upper and lower right panels, respectively. Purple, gray, red, and blue balls represent Bi, V, O, and P atoms, respectively. The blue arrows indicate elongation of the V^{4+}−O bonds. Some Bi atoms and some of the VO_4 tetrahedra are omitted for clarity.

Manuscript published in The Journal of Physical Chemistry C

(journal impact factor = 4.270)
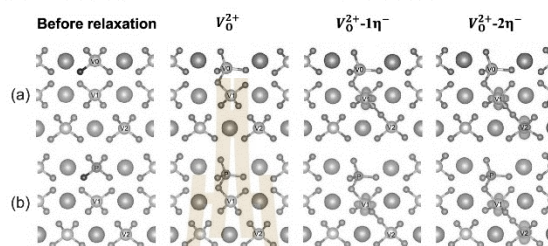
Figure 3. Geometry of the V_O structure of (a) pristine and (b) P-doped BiVO$_4$ with various charge states including the doubly positive V_O (V_O^{2+}), the ionized V_O with a single polaron (V_O^{2+}-$1\eta^-$), and that with two polarons (V_O^{2+}-$2\eta^-$). The yellow isosurface with a value of 0.02 e Å^{-3} indicates the spin density of the polaronic state. Purple, gray, red, and blue balls represent Bi, V, O, and P atoms, respectively. Black balls represent the removed O atoms. Some Bi atoms and some of the VO$_4$ tetrahedra are omitted for clarity.

the same way, as evidenced by their electronic trapped states and local distortions.

We further explored the behavior of polaron hopping to study the effect of P doping on the polaron mobility, where various possible migration paths were considered, as shown in Figure S3. We carried out CI-NEB calculations to determine the minimum energy path and the corresponding barrier. As presented in Table S2, the P impurity has negligible effects on the polaron mobilities as the calculated hopping barriers along various paths in both systems are invariant in the range of 0.3 eV. In addition, the adiabaticity of a polaron transfer in pristine and P-doped BiVO$_4$ was determined by computing the averaged electronic transmission coefficient, κ_{el}, within the description of Landau–Zener theory, as detailed in the Supporting Information, Section S5. The deviation of κ_{el} from unity is typically regarded as a nonadiabatic behavior. Our calculated κ_{el} of 0.37 is smaller than the previously reported value using the constrained DFT (CDFT) method (0.75) for the pristine system. Such a mismatch may stem from the uncertainty in estimating the coupling constant, V_{AB} (40 meV), and reorganization energy, λ (136 meV), where the ground-state theory (DFT) is used to identify the unoccupied state, as discussed by Adelstein et al.[55] Using a more robust CDFT method yields V_{AB} of 91 and 110 meV and λ of 120 meV.[30,52] Nevertheless, our calculated κ_{el} of 0.41 for the doped system is comparable to that of the pristine lattice, suggesting similar adiabaticity of polaron hopping. Overall, our computations suggest that P doping by itself hardly affects the behavior of polaron formation and migration in BiVO$_4$, despite the structural distortion and charge polarization occurring upon doping.

3.2. Formation of an Oxygen Vacancy. Among various point defects, oxygen vacancies (V_O) are known as potential n-type dopants to improve charge carrier concentrations in various TMOs including BiVO$_4$.[26–30,56] Creation of a V_O gives rise to two electron carriers, which have been regarded as the origin of the intrinsic n-type conductivity. The concentration of V_O in the lattice plays an important role in determining the electrical conductivity of materials. Therefore, relative stabilities of V_O in the pristine and doped systems were investigated to understand the effect of P doping on the improved current density of the photoanode.

We removed an O atom in a VO$_4$ unit and a PO$_4$ unit to generate a V_O in the pristine and P-doped BiVO$_4$ supercells, respectively. Various charge states of the V_O systems were

considered, including the doubly positive V_O (V_O^{2+}), the ionized V_O with a single polaron (V_O^{2+}-η^-), and that with two polarons (V_O^{2+}-$2\eta^-$). These charged systems can be obtained by manually adjusting the number of electrons in the supercell, where a compensating homogeneous background charge was imposed to ensure charge neutrality of the systems. Their ionic coordinates were relaxed to yield the V_O structures corresponding to the assigned charge state. In what follows, we explain how to obtain the V_O structures with various charge states, where the changes in atomistic and electronic structures are schematically illustrated in Figure 3 and detailed in the Supporting Information, Section S6. Calculated bond lengths of key polyhedra are summarized in Tables S4 and S5.

First, we optimized the doubly positive charge state (V_O^{2+}) systems. The V_O^{2+} state can be obtained by removing two electrons from the systems containing one V_O. For the pristine structure, the relaxed coordinates reveal that the VO$_3$ unit (denoted as V0) moves toward a neighboring VO$_4$ unit (denoted as V1) and shares one O atom with it, as depicted in Figure 3a. The newly formed V0–O bond is considerably longer than the equilibrium V–O bonds in the pristine structure (1.84 vs 1.75 Å), as summarized in Table S4. The structural reorganization, in turn, increases the bond distance between V1 and the shared O atom by 10 pm, whereas the other three V1–O bonds are shortened by 2–4 pm, as presented in Table S4. Next, we put one electron back into the optimized V_O^{2+} system to generate the V_O^{2+}-η^- system. Due to the elongation of the V1–O bond upon the removal of the O atom, the added electron prefers to localize at the V1 center and forms a small polaron, as indicated by the isosurface plot of its spin density, Figure 3a. A local structural distortion occurs upon polaron formation. The V1O$_4$ unit relaxes closer to the nearby VO$_4$ unit (denoted as V2) and shares one O atom to form a V1O$_5$ distorted trigonal bipyramid with a rather long apical V1–O bond of 220 pm, as detailed in Table S4. Finally, the second electron is added to the V_O^{2+}-η^- system to neutralize the V_O^{2+} charge and yield the V_O^{2+}-$2\eta^-$ system. As expected, the added electron localizes and forms a polaron at the V2 center, leading to elongations of V2O$_4$ bonds in the range of 7–9 pm.

Likewise, the P-doped system exhibits a similar behavior of polaron formation. Two electron polarons are generated upon the removal of an O atom at the PO$_4$ unit. These polarons localize at the two nearest V centers (V1 and V2) and create local structure distortions at the polaronic sites, Figure 3b and

Manuscript published in The Journal of Physical Chemistry C

(journal impact factor = 4.270)

Table S5. Nevertheless, a distinct difference from the pristine system is noted that the PO_4 bonds are significantly shorter than the VO_4 bonds. As a result, once the V_O is introduced at the PO_4 unit, the undercoordinated PO_3 unit relaxes closer to the V1 center to form the P−O bond with the shared O atom. The relaxed structure leads to a longer V1−O bond, which offers a preferred site for polaron formation, resulting in a relatively low polaron formation energy compared to that of the pristine system (60 meV more stable). The effect of P impurity toward the stability of polaron is exclusive at the nearest-neighbor V1 center. The second polaron formation at the V2 center is not affected, where their relative formation energies are very similar (energy difference is less than 1 meV).

To ensure that the obtained polaron configurations are the most stable, we calculated relative energies of several polaron configurations, where the two polarons are localized at different V centers throughout the lattice, as depicted in Figure S6. For both pristine and doped systems, the most stable configurations are indeed the ones we initially obtained, where the two polarons are located at the V1 and V2 centers, configuration C1. The other configurations where one or both polarons are not at the V1 and V2 sites are less stable, Figure S7. One example of the unstable configurations is that in which two electrons localize at the same V1 center, C2, and they exhibit higher energies by 111 and 136 meV for the pristine and P-doped systems, respectively (Figure S7). It is not surprising that the least stable configurations for both systems have two polarons far away from the V_O site, configuration C3. Nevertheless, in the case where one polaron is at the V1 center and the other polaron is not in the vicinity of the defect site, C4, the polaronic stability is comparable to that of the most stable configuration. The calculated results indicate that a V_O generates two electron polarons at the two nearest V centers, where one polaron is tightly bound to the defect site at the V1 center and the other polaron is relatively mobile.

3.3. Stability of Oxygen Vacancies. Next, we determined the relative stability of V_O in the pristine and P-doped systems to better understand the role of P doping in the improved photocatalytic activity. To obtain a complete picture of all V_O charge states and their corresponding ionization energies, we calculated and analyzed the defect formation energies as a function of Fermi energy. This method has been widely used to describe the stabilities of various defects in several semiconducting materials, including $BiVO_4$.[26,30,57] In addition, the stability of the P impurity and its V_O complex was calculated to explain the origin of the improved reducibility and charge carrier concentrations. The defect formation energies, E^f, for any point defect X^q in charge state q were calculated using the following expression[58,59]

$$E^f(X^q) = E_{tot}(X^q) - E_{tot}(bulk) - \sum_i \Delta n_i \mu_i$$
$$+ q(E_{VBM} + E_F) + E_{corr}^q$$

where $E_{tot}(X^q)$ is the total energy of the defective supercell containing point defect X^q in charge state q, and $E_{tot}(bulk)$ is the total energy of the pristine supercell. For each elemental species i, μ_i and Δn_i represent the chemical potential and the number of added (or removed) atoms in the defective supercell of the element. The chemical potential of each species was calculated by taking into account the thermodynamics of growth conditions, as discussed in the Supporting Information, Section S8. In addition, the chemical potential of

electron or Fermi energy, E_F, is considered, where its value is referenced to the energy of VBM, E_{VBM}. Defect formation energies are plotted as a function of Fermi level from zero to the band gap energy, E_g. The last term E_{corr}^q is responsible for correction of an artifact contributed by interactions between the charged defect and its periodic images. In this work, we use the image charge correction method proposed by Freysoldt, Neugebauer, and Van de Walle as implemented in the sxdefectalign code.[60−62]

As shown in Figure 4, the calculated formation energies of various defects are plotted as a function of Fermi energy from
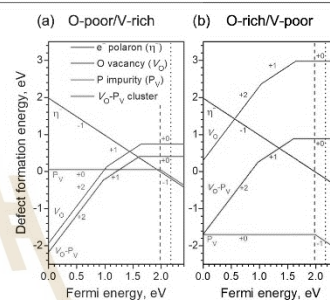

Figure 4. Defect formation energy of various defects in $BiVO_4$ as a function of Fermi energy for (a) O-poor/V-rich and (b) O-rich/V-poor conditions. The formation energies of the isolated electron polaron (η^-), oxygen vacancy (V_O), phosphorus substitution for vanadium (P_V), and defect complex of V_O and phosphorus impurity (V_O-P_V) are represented by purple, blue, red, and green lines, respectively. The purple dashed line and black dotted line indicate the polaron level of 1.98 eV and the conduction band minimum (CBM) level of 2.17 eV, respectively.

the valence band maximum (VBM) to the conduction band minimum (CBM). The calculated band gap of 2.17 eV is shown by the black dotted line, whereas the experimental band gap is 2.4 eV.[8,9] The slope of each line indicates the charge of the defect. It can be seen that an injected electron polaron is stable with a charge state of −1 at 0.19 eV below the CBM (purple dashed line). Such a calculated value is rather different from the result obtained by PBE + U (0.38 eV) in a previous computational work, where they used the tetragonal $BiVO_4$ to be the study model.[30]

Stabilities of V_O in the pristine and doped systems are of central interest. As previously discussed, the native V_O is in a doubly positive charged state where two electron polarons are formed at the two nearby V centers to neutralize the positive charges such that $V_O^{2+} + \eta^- \rightleftharpoons [V_O^{2+}\cdot\eta^-]$ and $[V_O^{2+}\cdot\eta^-] + \eta^- \rightleftharpoons [V_O^{2+}\cdot2\eta^-]$. Computations reveal that V_O is stable in three possible charged states of +2, + 1, and 0 within the band gap. The charge transition levels (CTLs) from +2 to +1 (+2/+1) and +1 to 0 (+1/0) are determined at 1.14 and 0.53 eV below the CBM, respectively. The calculated results are consistent with the previously reported value for (+1/0) at 0.59 eV below the CBM.[30] Such a deep CTL of (+1/0) indicates that the energy needed to ionize the trapped electrons to the conduction band to generate free electrons is quite large (0.53 eV) with respect to thermal energy at room temperature (0.026 eV). As a result, the electrons are likely to be trapped at

Manuscript published in The Journal of Physical Chemistry C

(journal impact factor = 4.270)
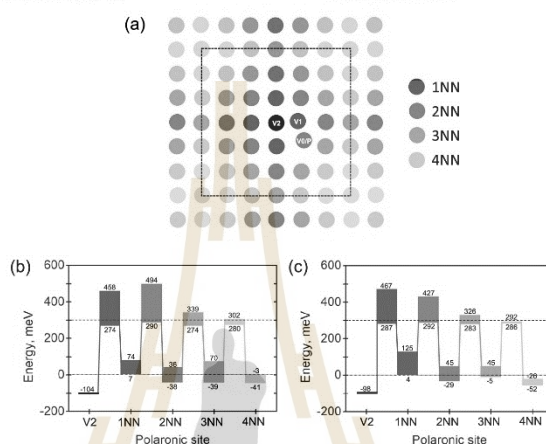
Figure 5. (a) Schematic illustrations of polaron migration paths in a supercell (applying periodic boundary conditions) of the V_O structure system, starting from the hopping of V2 to the first (1NN), second (2NN), third (3NN), and fourth (4NN) nearest neighbors, consecutively. Note that V_O generates two polarons at V1 and V2 centers, V0 and P are the O-deficient site for pristine and P-doped systems, respectively. The order of NN is referenced to V2. The distances between NN pairs are in the range of 4 Å. Potential energy profiles of all considered polaron migration paths in the V_O structure of (b) pristine and (c) P-doped BiVO$_4$. The relative energies are referenced to the energy of the system containing one polaron farthest from the defect center for each system in the presence of V_O (dotted line). The dashed line represents the polaron hopping barrier (0.3 eV) in pristine BiVO$_4$.

the local distortion as small polarons, which is consistent with that observed in an experimental work.[56] It has been reported that at a finite temperature the electronic conductivity in oxygen-deficient BiVO$_4$ is contributed by polaron migration rather than by band conduction.[30,62]

The energy difference between the calculated CTLs of the V_O with respect to that of the isolated polaron can be used to determine the binding energies of each polaron to the defect site. The binding energy, E_b, is the energy difference between the formation energy of a complex defect and the sum of formation energies of isolated defects. For example, the binding energy of a complex defect containing X and Y can be calculated by $E_b = E^f(X) + E^f(Y) - E^f([X-Y])$. The calculated binding energies of the first and second polarons are 0.34 and 0.95 eV, respectively. Their positive values indicate that these polarons are likely to be in proximity to the V_O site. Nevertheless, it is possible that one bound polaron can be thermally activated to migrate to other V centers since its binding energy is relatively low (0.34 eV). On the other hand, the large binding energy of 0.95 eV forbids the second polaron to hop away from the defect site. These results agree with those obtained from the total energy calculations that the polaron at the V1 center strongly binds to the V_O site.

P impurities can be introduced into the crystal in three possible defect forms, including interstitial phosphorus (P_i), phosphorus substitution for oxygen (P_O), and phosphorus substitution for vanadium (P_V). X-ray diffraction patterns reveal that the foreign P atoms substitute at V lattice sites and form a solid solution.[35] To confirm, their formation energies were calculated, as shown in Figure S9. It can be seen that P_V is the most stable for both O-poor and O-rich conditions because P and V have the same valency where their sizes are also similar ($r_P = 1.00$ Å, $r_V = 1.35$ Å). The P_V point defect is

determined as an isovalent doping where there is no charge carrier generated in the system, and its charged state is 0, as shown in Figure 4a.

To study the interaction between an electron polaron and the P_V defect, we induced the formation of a polaron at the V center adjacent to the PO$_4$ unit resulting in a defect complex of $[P_V^0 \cdot \eta^-]$ with charge −1, as described by $P_V^0 + \eta^- \rightleftharpoons [P_V^0 \cdot \eta^-]$. The defect complex exhibits the CTL of $(0/-1)$ at 0.19 eV below the CBM, which is equivalent to that of the isolated polaron. The calculated polaron binding energy of P_V is only 5 meV, suggesting that a polaron tends not to be bound to the P dopant. The calculated results are consistent with the transport behavior that P doping does not affect the polaron hopping barriers, where the calculated barriers in both pristine and P-doped systems are very similar (0.30 eV).

Next, we explored the effect of P doping on the stability of V_O. Computations show that P_V acts as a V_O trap, where the calculated binding energy of defect complex $[V_O^{2+}\text{-}P_V^0]$ is 0.29 eV. It is suggested that V_O^{2+} prefers to be in the vicinity of the P impurity in the lattice. The $[V_O^{2+}\text{-}P_V^0]$ complex can be neutralized by the presence of two trapped polarons at the two nearest V centers to yield charged states of +1 and 0 as $[V_O^{2+}\text{-}P_V^0] + \eta^- \rightleftharpoons [(V_O^{2+})\text{-}P_V^0\cdot\eta^-]$ and $[(V_O^{2+})\text{-}P_V^0\cdot\eta^-] + \eta^- \rightleftharpoons [V_O^{2+}\text{-}P_V^0\text{-}2\eta^-]$. As shown in Figure 4, the formation energy of this defect complex exhibits CTLs of $(+2/+1)$ and $(+1/+0)$ at 1.20 and 0.57 eV below the CBM, respectively, indicating deep donor states upon V_O formation. The calculated polaron binding energies of 0.38 and 1.01 eV for the two polarons are quite similar to the case of isolated V_O, which reflects that the defect complex could trap one polaron, whereas the other polaron is relatively mobile.

Although the isolated V_O and PO$_4$−V_O cluster exhibit similar behavior of polaron formation, the defect formation energy of

Manuscript published in The Journal of Physical Chemistry C

(journal impact factor = 4.270)

the cluster is 0.3 eV lower for charged states of +1 and 0 in the O-poor condition. Particularly, in the O-rich environment, the stability of V_O is dramatically improved (2.1 eV) in the presence of the P doping atom. The calculated results imply that P doping can stabilize V_O structures by forming a defect complex, leading to higher concentrations of V_O. We can roughly estimate the relative concentration of V_O, $N(T)$, between the pristine and doped systems using the expression, $N(T) = N_0 \exp(-E^f/k_B T)$, where N_0 is the total number of possible defect sites per unit volume in the crystal, k is the Boltzmann constant, and E^f is the defect formation energy. At a doping concentration of 1% and room temperature, the estimated concentration of V_O of the doped system is approximately 5 orders of magnitude greater than that of the pristine system. The calculated results are in agreement with that observed in the X-ray photoelectron spectroscopy (XPS) measurement that the concentration of V_O is improved upon P doping.[27] Hence, P doping improves reducibility, which increases the number of charge carriers in the $BiVO_4$ photoanode.

3.4. Behavior of Charge Transport. As discussed in the previous sections, the role of P doping in the improved photocatalytic activity could be described by its ability to stabilize V_O, which, in turn, increases the number of charge carriers in the materials. The character of the generated electron polarons is of particular interest. It is known that a polaron can undergo thermally activated hopping from one polaronic site to the nearby site throughout the lattice. In this section, we investigated the behavior of polaron transport and the mobility of polarons by computing their migration barriers. For both pristine and doped systems, the formation of a V_O generates two polarons at V1 and V2 centers, as denoted in Figure 3 and described in Section 3.2. These polarons induce a broken-symmetry lattice distortion resulting in nonequivalent polaron hopping paths. To systematically determine the behavior of polaron migration, we examined various possible paths of one polaron hopping away from the V_O site, while the other polaron is always trapped at the defect site.

Here, we calculated the migration barriers between nearest-neighbor (NN) sites starting from the hopping of V2 to the first nearest neighbor (1NN). As illustrated in Figure 5a, the migration scenario for both pristine and P-doped systems includes a consecutive hopping of V2 → 1NNs, 1NNs → 2NNs, 2NNs → 3NNs, and 3NNs → 4NNs, where the other polaron is located at V1 throughout the entire process. Potential energy profiles of all considered migration paths are depicted in Figure 5b,c for pristine and P-doped systems, respectively, where the band represents the variation of polaronic energies and barriers. The relative energies are referenced to the system containing one polaron farthest from the defect center.

For the pristine $BiVO_4$ system, as the polaron begins to move from V2 to the first nearest neighbors, V2 → 1NNs, it has to overcome a barrier in the range between 378 and 562 meV with an endothermic reaction energy from 111 to 178 meV. Such hopping paths with the highest barrier of 562 meV stem from the strong interaction between the V_O formation and polaron resulting in a distorted TS structure with a high TS energy. The bond distances and bond angles of VO_4 tetrahedra of the TS structure are asymmetric (V−O bond distances fluctuate between 174 and 181 pm, O−V−O bond angles vary between 103 and 113°), as depicted in Figure S10a. Note that the TS structure of the perfect crystal exhibits a

lower energy (0.3 eV), where both V centers consist of two sets of V−O bond distances (178 and 179 pm) and O−V−O bond angles (105 and 106°), Figure S10b. The subsequent step, 1NNs → 2NNs, is nearly isothermal, where the calculated barriers are in the range between 273 and 482 meV. This step still involves the polaron movement with a high barrier (482 meV) due to the interaction between the polaron and the defect. Its TS structure is strongly distorted with inequivalent V−O bond distances and O−V−O bond angles, which lead to a high TS energy, Figure S10c. Nevertheless, in this step, some hopping paths exhibit relatively low barriers as they are accompanied by symmetrical TS structures. The two subsequent steps, 2NNs → 3NNs → 4NNs, are considered as isothermal changes. Their hopping barriers (284−342 meV) are comparable to that of bulk migration, where the polaron−defect interaction vanishes, which hardly affects the hopping barriers. As a result, it is expected that the migration behavior in the V_O system resembles that of the perfect crystal from this step onward.

We now turn to describe the polaron transport in the P-doped $BiVO_4$ system with a V_O at the PO_4 unit. Similar to the movements in the pristine system, the hopping barriers of the first two steps are significantly higher than those of the subsequent steps. The highest barrier of 565 meV belongs to the first step, which is very similar to that of the pristine system (562 meV). All of these high barriers of the first two steps originate from the distorted TS structures (Figure S10d,e), resulting in high TS energies. The high-barrier characteristic is absent when the polaron hops further away from 2NNs onward. Their reaction energies and barriers are very similar to the migration in the perfect crystal. From the potential energy profiles of various hopping paths in both systems, the behavior of polaron transport in reduced $BiVO_4$ and P-doped $BiVO_4$ is not significantly different. The deviation of hopping barriers is quite large when polaron moves in close proximity to the defect site; then, the barriers become converged to the value of pristine bulk in the subsequent steps. The strong polaron−defect interaction largely affects the polaron transport within the 2NN region, where the polaron must overcome large barriers. When the polaron moves further away from the 2NN sites, the hopping barriers become the same as that of the perfect crystal.

To accurately take into account the anisotropic polaron hopping, it is required that hopping rates of all possible pathways in the vicinity of the defect site are statistically sampled within the kMC simulations. The electron transfer rates were computed according to Landau−Zener theory, as discussed in the Supporting Information, Section S5. All parameters used for computing the charge transfer rate are summarized in Table S3. Note that we used the pre-exponential values, including effective frequency ($h\nu_{eff}$ = 276 meV) and electronic transmission coefficient (κ_{el} = 0.75), as reported by Wu and Ping[52] since they were computed within a more robust description of the CDFT method. Upon formation of a V_O, dramatic local distortions are expected to create strong anisotropic mobility; therefore, hopping barriers of all possible pathways in the vicinity of the defect site (up to 4NNs) were used as inputs for the kMC simulations. The migration barriers included in the kMC simulations are listed in Tables S6 and S7 for the pristine and doped systems, respectively. As the polaron moves farther away, its barrier resembles that of bulk migration, where the hopping barrier of the perfect crystal (0.3 eV) is used as input. In contrast,

Manuscript published in The Journal of Physical Chemistry C

(journal impact factor = 4.270)

anisotropicity is much less prominent in the absence of V_O; hence, the barriers of bulk migrations in the pristine and doped systems were included in the simulations, as summarized in Table S2. With these numerical inputs, the simulations reveal that the carrier mobilities of the pristine and doped systems are quite similar in the presence and absence of V_O, Table 2. Our

Table 2. Electron Polaron Drift Mobility (μ) and Apparent Activation Energy (E_{app}) of Pristine, P-Doped BiVO$_4$, and the V_O Structure of BiVO$_4$ and P-Doped BiVO$_4$ at Room Temperature (300 K)

system	μ (10^{-6} cm^2 V^{-1} s^{-1})	E_{app} (meV)
pristine	5.05	303
P-doped BiVO$_4$	4.06	308
BiVO$_4$ with V_O	1.66	391
P-doped BiVO$_4$ with V_O	0.92	407

estimated mobility of the pristine system (5.05×10^{-6} cm^2 V^{-1} s^{-1}) is significantly lower than the previously calculated value (1.38×10^{-4} cm^2 V^{-1} s^{-1})[52] because our input barriers are slightly higher (0.30 vs 0.25 eV[52]). Nevertheless, our calculated barriers of 0.30 eV are in reasonable agreement with the experimentally determined value (0.29 eV) in W-doped BiVO$_4$[46] and the computed value (0.35 eV) obtained using the hybrid functional in electron-doped BiVO$_4$.[47] The charge transfer kinetics become sluggish in the presence of V_O, where the estimated mobilities are lower than those of systems without V_O defects, Table 2. Our finding is consistent with previous results, suggesting that the formation of V_O slows down the charge carrier transport in BiVO$_4$[56,63] and other TMOs, such as TiO$_4$[64] and α-Fe$_2$O$_3$.[65] The obtained polaron mobilities at different temperatures can be used to further calculate the apparent activation energy of polaron hopping as $\mu(T) = A \exp(-E_{app}/k_B T)$. The calculated E_{app} of all systems at room temperature are summarized in Table 2. As expected, the E_{app} are inversely proportional to the carrier mobilities, where the higher mobility systems exhibit lower apparent activation energy.

Moreover, polaron mobility can be estimated from the dielectric constants of the system. In particular, the hopping barrier can be estimated as $E_a = \frac{e^2}{4\varepsilon_p}\left(\frac{1}{r_p} - \frac{1}{R}\right)$, where $\frac{1}{r_p} = \frac{1}{\varepsilon_\infty} - \frac{1}{\varepsilon_0}$, ε_∞ and ε_0 are the high-frequency and static dielectric constants, respectively; r_p is the small polaron radius, which can be defined as $r_p = 1/2(\pi/6)^{1/3}\bar{a}$, where $\bar{a}^{-3}$ is the number of centers per unit volume; and R is the distance between hopping centers.[66] In the absence of V_O, the calculated ε_p for the pristine (9.28) and P-doped systems (8.93) are quite similar, which lead to a negligible difference of E_a of only 3.9% upon doping. A similar trend is observed for the V_O systems, where the pristine and doped systems exhibit comparable ε_p (7.59 vs 7.49), resulting in 1.3% difference of E_a. Relatively slow kinetics is predicted in the presence of V_O, where E_a is increased by 22.3 and 19.3% for the pristine and P-doped systems, respectively. The carrier mobility obtained from the kMC simulations and estimation of barriers from dielectric constants confirm that P doping does not play a role in hopping conduction itself as the polaron mobilities are hardly changed upon doping in the presence and absence of V_O. Its crucial role lies in the stabilization of the V_O structure, which increases the number of charge carriers in the materials.

Although it is expected that V_O impedes the polaron conduction, the increased carrier concentration arising from V_O formation and light absorption could yield an improved electronic conductivity for the system.

4. CONCLUSIONS

This work utilizes the DFT + U method to explore the effect of P doping on the improved photocatalytic activity of a BiVO$_4$ photoanode. It can be seen that introduction of P impurities does not significantly affect the electronic structure and electron mobilities of the host system. On the other hand, the computed defect formation energies reveal that P doping improves the reducibility of the material by lowering the energies of V_O formation. Upon the formation of an oxygen vacancy, two electron polarons are generated and localized at the two nearby V centers. We examine the behavior of the generated polarons and find that one polaron is trapped at the defect site, while the other polaron is relatively mobile. In the presence and absence of oxygen vacancies, kMC simulations reveal that the polaron mobility and apparent activation energy of the pristine and doped systems are quite similar. Therefore, P doping increases the number of charge carriers through the improved reducibility while maintaining the carrier mobility. The conclusion drawn here based on the microscopic investigation explains the macroscopically observed higher oxygen-vacancy concentration and improved photocatalytic efficiency of the P-doped samples. Our study sheds light on the fundamental understanding of the mechanisms responsible for high-performance P-doped BiVO$_4$ photoanodes.

■ ASSOCIATED CONTENT

ⓈI Supporting Information

The Supporting Information is available free of charge at https://pubs.acs.org/doi/10.1021/acs.jpcc.9b09909.

Detailed results of structures of the ms-BiVO$_4$ unit cell and $3 \times 3 \times 1$ P-doped BiVO$_4$ supercell (Section S1); density of states (DOS) of pristine and P-doped BiVO$_4$ (Section S2); the change of charge distribution upon P doping (Section S3); polaron migration in electron-doped BiVO$_4$ and P-doped BiVO$_4$ (Section S4); parameters for the polaron transfer rate (Section S5); geometry of the oxygen-vacancy (V_O) structure of pristine and P-doped BiVO$_4$ with various charge states (Section S6); Several configurations of small polaron localization in the V_O structure of pristine and P-doped BiVO$_4$ (Section S7); Chemical potential (Section S8); defect formation energy of P impurity point defects in BiVO$_4$ (Section S9) and polaron migration in the V_O structure of pristine and P-doped BiVO$_4$ (Section S10) (PDF)

■ AUTHOR INFORMATION

Corresponding Author

Suwit Suthirakun − Center of Excellence in Advanced Functional Materials and School of Chemistry, Institute of Science, Suranaree University of Technology, Nakhon Ratchasima 30000, Thailand; ● orcid.org/0000-0002-6590-6343; Phone: +66 44 224-886; Email: suthirak@sut.ac.th

Authors

Apinya Ngoipala − School of Physics, Institute of Science and Center of Excellence in Advanced Functional Materials,

Manuscript published in The Journal of Physical Chemistry C

(journal impact factor = 4.270)

Suranaree University of Technology, Nakhon Ratchasima 30000, Thailand; Thailand Center of Excellence in Physics, Ministry of Higher Education, Science, Research and Innovation, Bangkok 10400, Thailand

Lappawat Ngamwongwan − School of Physics, Institute of Science and Center of Excellence in Advanced Functional Materials, Suranaree University of Technology, Nakhon Ratchasima 30000, Thailand; Thailand Center of Excellence in Physics, Ministry of Higher Education, Science, Research and Innovation, Bangkok 10400, Thailand

Ittipon Fongkaew − School of Physics, Institute of Science and Center of Excellence in Advanced Functional Materials, Suranaree University of Technology, Nakhon Ratchasima 30000, Thailand; Thailand Center of Excellence in Physics, Ministry of Higher Education, Science, Research and Innovation, Bangkok 10400, Thailand

Sirichok Jungthawan − School of Physics, Institute of Science and Center of Excellence in Advanced Functional Materials, Suranaree University of Technology, Nakhon Ratchasima 30000, Thailand; Thailand Center of Excellence in Physics, Ministry of Higher Education, Science, Research and Innovation, Bangkok 10400, Thailand

Pussana Hirunsit − National Nanotechnology Center (NANOTEC), National Science and Technology Development Agency (NSTDA), Pathum Thani 12120, Thailand; ● orcid.org/0000-0003-1309-7553

Sukit Limpijumnong − School of Physics, Institute of Science, Suranaree University of Technology, Nakhon Ratchasima 30000, Thailand; The Institute for the Promotion of Teaching Science and Technology (IPST), Bangkok 10110, Thailand

Complete contact information is available at:
https://pubs.acs.org/10.1021/acs.jpcc.9b09909

Notes

The authors declare no competing financial interest.

■ **REFERENCES**

(1) Walter, M. G.; Warren, E. L.; McKone, J. R.; Boettcher, S. W.; Mi, Q.; Santori, E. A.; Lewis, N. S. Solar Water Splitting Cells. *Chem. Rev.* **2010**, *110*, 6446−6473.

(2) Tran, P. D.; Wong, L. H.; Barber, J.; Loo, J. S. C. Recent Advances in Hybrid Photocatalysts for Solar Fuel Production. *Energy Environ. Sci.* **2012**, *5*, 5902−5918.

(3) Maeda, K. Photocatalytic Water Splitting Using Semiconductor Particles: History and Recent Developments. *J. Photochem. Photobiol., C* **2011**, *12*, 237−268.

(4) Jafari, T.; Moharreri, E.; Amin, S. A.; Miao, R.; Song, W.; Suib, L. S. Photocatalytic Water Splitting-The Untamed Dream: A Review of Recent Advances. *Molecules* **2016**, *21*, No. E900.

(5) Park, Y.; McDonald, K. J.; Choi, K.-S. Progress in Bismuth Vanadate Photoanodes for Use in Solar Water Oxidation. *Chem. Soc. Rev.* **2013**, *42*, 2321−2337.

(6) Xi, G.; Ye, J. Synthesis of Bismuth Vanadate Nanoplates with Exposed (001) Facets and Enhanced Visible-Light Photocatalytic Properties. *Chem. Commun.* **2010**, *46*, 1893−1895.

(7) Zhao, Z.; Li, Z.; Zou, Z. Electronic Structure and Optical Properties of Monoclinic Clinobisvanite BiVO$_4$. *Phys. Chem. Chem. Phys.* **2011**, *13*, 4746−4753.

(8) Kudo, A.; Omori, K.; Kato, H. A Novel Aqueous Process for Preparation of Crystal Form-Controlled and Highly Crystalline BiVO$_4$ Powder from Layered Vanadates at Room Temperature and Its Photocatalytic and Photophysical Properties. *J. Am. Chem. Soc.* **1999**, *121*, 11459−11467.

(9) Tokunaga, S.; Kato, H.; Kudo, A. Selective Preparation of Monoclinic and Tetragonal BiVO$_4$ with Scheelite Structure and Their Photocatalytic Properties. *Chem. Mater.* **2001**, *13*, 4624−4628.

(10) Zhong, D. K.; Choi, S.; Gamelin, D. R. Near-Complete Suppression of Surface Recombination in Solar Photoelectrolysis by "Co-Pi" Catalyst-Modified W:BiVO$_4$. *J. Am. Chem. Soc.* **2011**, *133*, 18370−18377.

(11) Abdi, F. F.; van de Krol, R. Nature and Light Dependence of Bulk Recombination in Co-Pi-Catalyzed BiVO$_4$ Photoanodes. *J. Phys. Chem. C* **2012**, *116*, 9398−9404.

(12) Abdi, F. F.; Savenije, T. J.; May, M. M.; Dam, B.; van de Krol, R. The Origin of Slow Carrier Transport in BiVO$_4$ Thin Film Photoanodes: A Time-Resolved Microwave Conductivity Study. *J. Phys. Chem. Lett.* **2013**, *4*, 2752−2757.

(13) Ziwritsch, M.; Müller, S.; Hempel, H.; Unold, T.; Abdi, F. F.; van de Krol, R.; Friedrich, D.; Eichberger, R. Direct Time-Resolved Observation of Carrier Trapping and Polaron Conductivity in BiVO$_4$. *ACS Energy Lett.* **2016**, *1*, 888−894.

(14) Berglund, S. P.; Rettie, A. J. E.; Hoang, S.; Mullins, C. B. Incorporation of Mo and W into Nanostructured BiVO$_4$ Films for Efficient Photoelectrochemical Water Oxidation. *Phys. Chem. Chem. Phys.* **2012**, *14*, 7065−7075.

(15) Bosman, A. J.; van Daal, H. J. Small-Polaron versus Band Conduction in Some Transition-Metal Oxides. *Adv. Phys.* **1970**, *19*, 1−117.

(16) Lany, S. Semiconducting Transition Metal Oxides. *J. Phys.: Condens. Matter* **2015**, *27*, No. 283203.

(17) Canali, C.; Majni, G.; Minder, R.; Ottaviani, G. Electron and Hole Drift Velocity Measurements in Silicon and Their Empirical Relation to Electric Field and Temperature. *IEEE Trans. Electron Devices* **1975**, *22*, 1045−1047.

(18) Pilli, S. K.; Furtak, T. E.; Brown, L. D.; Deutsch, T. G.; Turner, J. A.; Herring, A. M. Cobalt-phosphate (Co-Pi) catalyst modified Mo-doped BiVO$_4$ photoelectrodes for solar water oxidation. *Energy Environ. Sci.* **2011**, *4*, 5028−5034.

(19) Luo, W.; Wang, Z.; Wan, L.; Li, Z.; Yu, T.; Zou, Z. Synthesis, Growth Mechanism and Photoelectrochemical Properties of BiVO$_4$ Microcrystal Electrodes. *J. Phys. D: Appl. Phys.* **2010**, *43*, No. 405402.

(20) Su, J.; Guo, L.; Yoriya, S.; Grimes, C. A. Aqueous Growth of Pyramidal-Shaped BiVO$_4$ Nanowire Arrays and Structural Characterization: Application to Photoelectrochemical Water Splitting. *Cryst. Growth Des.* **2010**, *10*, 856−861.

(21) Su, J.; Guo, L.; Bao, N.; Grimes, C. A. Nanostructured WO$_3$/BiVO$_4$ Heterojunction Films for Efficient Photoelectrochemical Water Splitting. *Nano Lett.* **2011**, *11*, 1928−1933.

(22) Pilli, S. K.; Deutsch, T. G.; Furtak, T. E.; Brown, L. D.; Turner, J. A.; Herring, A. M. BiVO$_4$/CuWO$_4$ Heterojunction Photoanodes for Efficient Solar Driven Water Oxidation. *Phys. Chem. Chem. Phys.* **2013**, *15*, 3273−3278.

(23) Selim, S.; Francàs, L.; García-Tecedor, M.; Corby, S.; Blackman, C.; Gimenez, S.; Durrant, J. R.; Kafizas, A. WO$_3$/BiVO$_4$: Impact of Charge Separation at the Timescale of Water Oxidation. *Chem. Sci.* **2019**, *10*, 2643−2652.

(24) Saito, R.; Miseki, Y.; Sayama, K. Highly Efficient Photoelectrochemical Water Splitting Using a Thin Film Photoanode of BiVO$_4$/SnO$_2$/WO$_3$ Multi-Composite in a Carbonate Electrolyte. *Chem. Commun.* **2012**, *48*, 3833−3835.

(25) Jeon, T. H.; Choi, W.; Park, H. Cobalt−Phosphate Complexes Catalyze the Photoelectrochemical Water Oxidation of BiVO$_4$ Electrodes. *Phys. Chem. Chem. Phys.* **2011**, *13*, 21392−21401.

Manuscript published in The Journal of Physical Chemistry C

(journal impact factor = 4.270)

(26) Yin, W.-J.; Wei, S.-H.; Al-Jassim, M. M.; Turner, J.; Yan, Y. Doping Properties of Monoclinic BiVO$_4$ Studied by First-Principles Density-Functional Theory. *Phys. Rev. B* **2011**, *83*, No. 155102.

(27) Xia, T.; Chen, M.; Xiao, L.; Fan, W.; Mao, B.; Xu, D.; Guan, P.; Zhu, J.; Shi, W. Dip-Coating Synthesis of P-doped BiVO$_4$ Photoanodes with Enhanced Photoelectrochemical Performance. *J. Taiwan Inst. Chem. Eng.* **2018**, *93*, 582−589.

(28) Ullah, H.; Tahir, A. A.; Mallick, T. K. Structural and Electronic Properties of Oxygen Defective and Se-Doped p-Type BiVO$_4$ (001) Thin Film for the Applications of Photocatalysis. *Appl. Catal., B* **2018**, *224*, 895−903.

(29) Kim, T. W.; Ping, Y.; Galli, G. A.; Choi, K.-S. Simultaneous Enhancements in Poton Absorption and Charge Transport of Bismuth Vanadate Photoanodes for Solar Water Splitting. *Nat. Commun.* **2015**, *6*, No. 8769.

(30) Seo, H.; Ping, Y.; Galli, G. Role of Point Defects in Enhancing the Conductivity of BiVO$_4$. *Chem. Mater.* **2018**, *30*, 7793−7802.

(31) Park, H. S.; Kweon, K. E.; Ye, H.; Paek, E.; Hwang, G. S.; Bard, A. J. Factors in the Metal Doping of BiVO$_4$ for Improved Photoelectrocatalytic Activity as Studied by Scanning Electrochemical Microscopy and First-Principles Density-Functional Calculation. *J. Phys. Chem. C* **2011**, *115*, 17870−17879.

(32) Zhang, J.; Deng, M.; Ren, F.; Wu, Y.; Wang, Y. Effects of Mo/W Codoping on the Visible-Light Photocatalytic Activity of Monoclinic BiVO$_4$ within the GGA + U Framework. *RSC Adv.* **2016**, *6*, 12290−12297.

(33) Liu, B.; Yan, X.; Yan, H.; Yao, Y.; Cai, Y.; Wei, J.; Chen, S.; Xu, X.; Li, L. Preparation and Characterization of Mo Doped in BiVO$_4$ with Enhanced Photocatalytic Properties. *Materials* **2017**, *10*, No. 976.

(34) Jo, W. J.; Jang, J.-W.; Kong, K.-j.; Kang, H. J.; Kim, J. Y.; Jun, H.; Parmar, K. P. S.; Lee, J. S. Phosphate Doping into Monoclinic BiVO$_4$ for Enhanced Photoelectrochemical Water Oxidation Activity. *Angew Chem., Int. Ed.* **2012**, *51*, 3147−3151.

(35) Liu, G.; Liu, S.; Lu, Q.; Sun, H.; Xiu, Z. Synthesis and Characterization of BiVO$_4$–PO$_4$ Nanofibers by Electrospinning Process with Enhanced Photocatalytic Activity under Visible Light. *RSC Adv.* **2014**, *4*, 33695−33701.

(36) Regmi, C.; Kshetri, Y. K.; Dhakal, D.; Sohng, J. K.; Rosei, F.; Lee, S. W. Insight into Phosphate Doped BiVO$_4$ Heterostructure for Multifunctional Photocatalytic Performances: A Combined Experimental and DFT Study. *Appl. Surf. Sci.* **2019**, *466*, 787−800.

(37) Govindaraju, G. V.; Morbec, J. M.; Galli, G. A.; Choi, K.-S. Experimental and Computational Investigation of Lanthanide Ion Doping on BiVO$_4$ Photoanodes for Solar Water Splitting. *J. Phys. Chem. C* **2018**, *122*, 19416−19424.

(38) Jiang, Z.; Liu, Y.; Jing, T.; Huang, B.; Zhang, X.; Qin, X.; Dai, Y.; Whangbo, M.-H. Enhancing the Photocatalytic Activity of BiVO$_4$ for Oxygen Evolution by Ce Doping: Ce^{3+} Ions as Hole Traps. *J. Phys. Chem. C* **2016**, *120*, 2058−2063.

(39) Kresse, G.; Furthmüller, J. Efficient Iterative Schemes for Ab Initio Total-Energy Calculations using a Plane-Wave Basis Set. *Phys. Rev. B* **1996**, *54*, 11169−11186.

(40) Kresse, G.; Furthmüller, J. Efficiency of Ab-Initio Total Energy Calculations for Metals and Semiconductors using a Plane-Wave Basis Set. *Comput. Mater. Sci.* **1996**, *6*, 15−50.

(41) Kresse, G.; Hafner, J. Ab Initio Molecular Dynamics for Liquid Metals. *Phys. Rev. B* **1993**, *47*, 558−561.

(42) Blöchl, P. E. Projector Augmented-Wave Method. *Phys. Rev. B* **1994**, *50*, 17953−17979.

(43) Kresse, G.; Joubert, D. From Ultrasoft Pseudopotentials to the Projector Augmented-Wave Method. *Phys. Rev. B* **1999**, *59*, 1758−1775.

(44) Perdew, J. P.; Burke, K.; Ernzerhof, M. Generalized Gradient Approximation Made Simple. *Phys. Rev. Lett.* **1996**, *77*, 3865−3868.

(45) Dudarev, S. L.; Botton, G. A.; Savrasov, S. Y.; Humphreys, C. J.; Sutton, A. P. Electron-Energy-Loss Spectra and the Structural Stability of Nickel Oxide: An LSDA+U Study. *Phys. Rev. B* **1998**, *57*, 1505−1509.

(46) Rettie, A. J. E.; Lee, H. C.; Marshall, L. G.; Lin, J.-F.; Capan, C.; Lindemuth, J.; McCloy, J. S.; Zhou, J.; Bard, A. J.; Mullins, C. B. Combined Charge Carrier Transport and Photoelectrochemical Characterization of BiVO$_4$ Single Crystals: Intrinsic Behavior of a Complex Metal Oxide. *J. Am. Chem. Soc.* **2013**, *135*, 11389−11396.

(47) Kweon, K. E.; Hwang, G. S.; Kim, J.; Kim, S.; Kim, S. Electron Small Polarons and Their Transport in Bismuth Vanadate: a First Principles Study. *Phys. Chem. Chem. Phys.* **2015**, *17*, 256−260.

(48) Sleight, A. W.; Chen, H.; Ferretti, A.; Cox, D. E. Crystal Growth and Structure of BiVO$_4$. *Mater. Res. Bull.* **1979**, *14*, 1571−1581.

(49) Baroni, S.; de Gironcoli, S.; Dal Corso, A.; Giannozzi, P. Phonons and Related Crystal Properties from Density-Functional Perturbation Theory. *Rev. Mod. Phys.* **2001**, *73*, 515−562.

(50) Maxisch, T.; Zhou, F.; Ceder, G. Ab Initio Study of the Migration of Small Polarons in Olivine Li$_x$FePO$_4$ and Their Association with Lithium Ions and Vacancies. *Phys. Rev. B* **2006**, *73*, No. 104301.

(51) Henkelman, G.; Uberuaga, B. P.; Jónsson, H. A Climbing Image Nudged Elastic Band Method for Finding Saddle Points and Minimum Energy Paths. *J. Chem. Phys.* **2000**, *113*, 9901−9904.

(52) Wu, F.; Ping, Y. Combining Landau−Zener Theory and Kinetic Monte Carlo Sampling for Small Polaron Mobility of Doped BiVO$_4$ from First-Principles. *J. Mater. Chem. A* **2018**, *6*, 20025−20036.

(53) Payne, D. J.; Robinson, M. D. M.; Egdell, R. G.; Walsh, A.; McNulty, J.; Smith, K. E.; Piper, L. F. J. The Nature of Electron Lone Pairs in BiVO$_4$. *Appl. Phys. Lett.* **2011**, *98*, 212110−2121103.

(54) Stampfl, C.; Van de Walle, C. G. Density-Functional Calculations for III-V Nitrides using the Local-Density Approximation and the Generalized Gradient Approximation. *Phys. Rev. B* **1999**, *59*, 5521−5535.

(55) Adelstein, N.; Neaton, J. B. Asta, M.; De Jonghe, L. C. Density Functional Theory Based Calculation of Small-Polaron Mobility in Hematite. *Phys. Rev. B* **2014**, *89*, No. 245115.

(56) Cooper, J. K.; Scott, S. B.; Ling, Y.; Yang, J.; Hao, S.; Li, Y.; Toma, F. M.; Stutzmann, M.; Lakshmi, K. V.; Sharp, I. D. Role of Hydrogen in Defining the n-Type Character of BiVO$_4$ Photoanodes. *Chem. Mater.* **2016**, *28*, 5761−5771.

(57) Wang, G.; Ling, Y.; Lu, X.; Qian, F.; Tong, Y.; Zhang, J. Z.; Lordi, V.; Rocha Leao, C.; Li, Y. Computational and Photoelectrochemical Study of Hydrogenated Bismuth Vanadate. *J. Phys. Chem. C* **2013**, *117*, 10957−10964.

(58) Zhang, S. B.; Northrup, J. E. Chemical Potential Dependence of Defect Formation Energies in GaAs: Application to Ga Self-Diffusion. *Phys. Rev. Lett.* **1991**, *67*, 2339−2342.

(59) Freysoldt, C.; Grabowski, B.; Hickel, T.; Neugebauer, J.; Kresse, G.; Janotti, A.; Van de Walle, C. G. First-principles Calculations for Point Defects in Solids. *Rev. Mod. Phys.* **2014**, *86*, 253−305.

(60) Freysoldt, C.; Neugebauer, J.; Van de Walle, C. G. Fully Ab Initio Finite-Size Corrections for Charged-Defect Supercell Calculations. *Phys. Rev. Lett.* **2009**, *102*, No. 016402.

(61) Freysoldt, C.; Neugebauer, J.; Van de Walle, C. G. Electrostatic Interactions between Charged Defects in Supercells. *Phys. Status Solidi B* **2011**, *248*, 1067−1076.

(62) Kumagai, Y.; Oba, F. Electrostatics-Based Finite-Size Corrections for First-Principles Point Defect Calculations. *Phys. Rev. B* **2014**, *89*, No. 195205.

(63) Qiu, W.; Xiao, S.; Ke, J.; Wang, Z.; Tang, S.; Zhang, K.; Qian, W.; Huang, Y.; Huang, D.; Tong, Y.; Yang, S. Freeing the Polarons to Facilitate Charge Transport in BiVO$_4$ from Oxygen Vacancies with an Oxidative 2D Precursor. *Angew. Chem.* **2019**, *131*, 19263−19271.

(64) Pham, H. H.; Wang, L.-W. Oxygen Vacancy and Hole Conduction in Amorphous TiO$_2$. *Phys. Chem. Chem. Phys.* **2015**, *17*, 541−550.

(65) Smart, T. J.; Ping, Y. Effect of Defects on the Small Polaron Formation and Transport Properties of Hematite from First-Principles Calculations. *J. Phys.: Condens. Matter* **2017**, *29*, No. 394006.

Manuscript published in The Journal of Physical Chemistry C

(journal impact factor = 4.270)

(66) Kim, T. W.; Ping, Y.; Galli, G. A.; Choi, K.-S. Simultaneous Enhancements in Photon Absorption and Charge Transport of Bismuth Vanadate Photoanodes for Solar Water Splitting. *Nat. Commun.* **2015**, *6*, No. 8769.
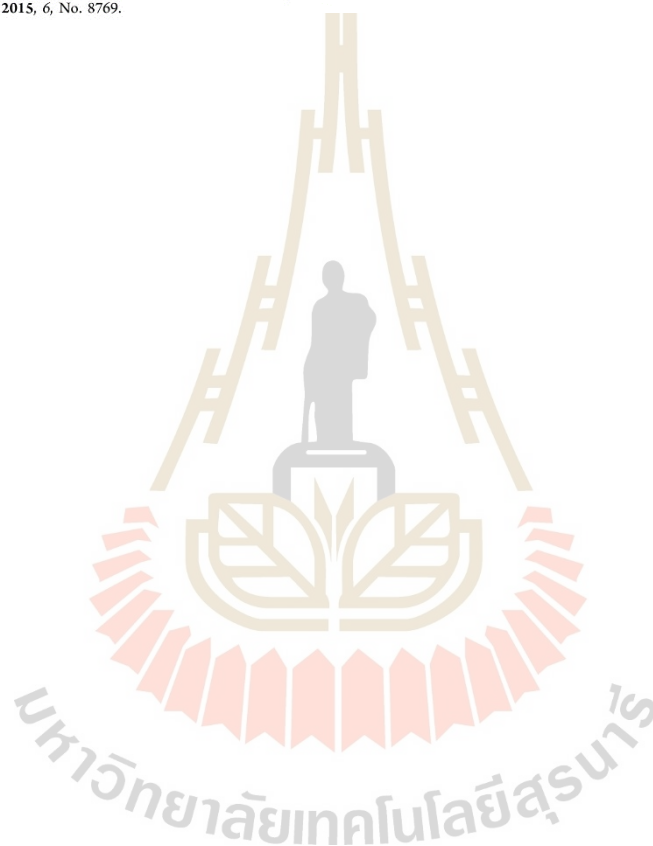
Abstract submitted in The 2nd Taiwan-Thailand-Vietnam Workshop on Theoretical

and Computational Chemistry (TTV2) (2019)

NANOTEC
a member of NSTDA   The 2nd Taiwan-Thailand-Vietnam Workshop on Theoretical and Computational Chemistry (TTV2)

Role of P-doping on the Enhanced Photoelectrochemical Performance of BiVO$_4$-based Photoanodes: A First Principles Study

Apinya Ngoipala[1,2], Sirichok Jungthawan[1,2], Suwit Suthirakun[2,3]*

1School of Physics, Institute of Science, Suranaree University of Technology,
Nakhon Ratchasima, 30000, Thailand
2Center of Excellence in Advanced Functional Materials, Suranaree University of Technology,
Nakhon Ratchasima, 30000, Thailand
3School of Chemistry, Institute of Science, Suranaree University of Technology,
Nakhon Ratchasima, 30000, Thailand
*E-mail: suthirak@sut.ac.th

Abstract:

Phosphate-doped BiVO$_4$ has been experimentally proposed as a promising photoanode for water splitting as it exhibits significant improvement of photocurrent density and photocatalytic O$_2$ revolution rate [1]. In this work, we utilized first-principles plane-wave calculations to better understand the effect of phosphate doping on the charge transport kinetics of the BiVO$_4$-based photocatalysts. In particular, density functional theory (DFT+U) calculations were carried out to explore geometrical and electronic structures of pristine and P-doped BiVO$_4$ systems. Computations reveal that substitution of V with phosphorous does not significantly alter the electronic structures of the materials as the band gap and features of frontier orbitals of the pristine and doped systems are very similar. Interestingly, P-doping improves reducibility of the materials as reflects through the lower energy of oxygen vacancy formation in the P-doped system. The generated oxygen vacancy yields two extra electrons localized at the two nearest V centers which in turn reduces V^{5+} to V^{4+}. The self-trapped electron induces local structure distortion around the reduced V center leading to a formation of a small polaron. The mobilities of the generated charge carriers were accessed using a method based on Marcus theory. This work provides key approaches for the design of non-metal doped BiVO$_4$ photoanode for solar-to-fuel conversion.

References:
[1] W. J. Jo, J.-W. Jang, H. J. Kang, J. Y. Kim, H. Jun, K. P. S. Parmar, J. S. Lee, **Angew. Chem. Int. Ed.**, *51*, 3147–3151 (2012).

Keywords: Phosphate-doped BiVO$_4$, photocatalysts, density functional theory

Abstract submitted in The International Centre for Theoretical Physics (ICTP) Asian

Network School and Workshop on Complex Condensed Matter Systems (2019)

Role of P-doping on the Enhanced Photoelectrochemical Performance of $BiVO_4$-based Photoanodes: A First Principles Study

Apinya Ngoipala[1,2], Sirichok Jungthawan[1,2], Suwit Suthirakun[2,3]
[1]School of Physics, Institute of Science, Suranaree University of Technology,
Nakhon Ratchasima, 30000, Thailand
[2]Center of Excellence in Advanced Functional Materials, Suranaree University
of Technology, Nakhon Ratchasima, 30000, Thailand
[3]School of Chemistry, Institute of Science, Suranaree University of Technology,
Nakhon Ratchasima, 30000, Thailand

Abstracts:

Phosphate-doped $BiVO_4$ has been experimentally proposed as a promising photoanode for water splitting as it exhibits significant improvement of photocurrent density and photocatalytic O_2 revolution rate. In this work, we utilized first-principles plane-wave calculations to better understand the effect of phosphate doping on the charge transport kinetics of the $BiVO_4$-based photocatalysts. In particular, density functional theory (DFT+U) calculations were carried out to explore geometrical and electronic structures of pristine and P-doped $BiVO_4$ systems. Computations reveal that substitution of V with phosphorous does not significantly alter the electronic structures of the materials as the band gap and features of frontier orbitals of the pristine and doped systems are very similar. Interestingly, P-doping improves reducibility of the materials as reflects through the lower energy of oxygen vacancy formation in the P-doped system. The generated oxygen vacancy yields two extra electrons localized at the two nearest V centers which in turn reduces V^{5+} to V^{4+}. The self-trapped electron induces local structure distortion around the reduced V center leading to a formation of a small polaron. The mobilities of the generated charge carriers were accessed using a method based on Marcus theory. This work provides key approaches for the design of non-metal doped $BiVO_4$ photoanode for solar-to-fuel conversion.

CURRICULUM VITAE

Apinya Ngoipala was born on April 20, 1996 in Sakon Nakhon, Thailand. She received her B.Sc. in Physics (first-class honors) in 2017 from the Department of Physics, Faculty of Science, Khon Kaen University. She has granted the scholarship from the Development and Promotion of Science and Technology Talents Project (DPST, THAILAND) since 2014. During her senior year in bachelor's degree, she has successfully completed an internship (3 months) at the Computational and Theoretical Chemistry Lab at the School of Molecular Sciences, The University of Western Australia under the supervision of Assoc. Prof. Dr. Amir Karton, Dr. Tanveer Hussain, and Asst. Prof. Dr. Thanayut Kaewmaraya. In 2018, she continued to pursue the Master's degree program in the School of Physics, Suranaree University of Technology with DPST scholarship under the supervision of Asst. Prof. Dr. Suwit Suthirakun and Assoc. Prof. Dr. Sirichok Jungthawan. She has published an article in an international journal [J. Phys. Chem. C, 124, 8, 4352, (2020)] and also participated in the international conferences (listed in APPENDIX B) during the course of her master program education.